University of Naples Federico II
Polytechnic and Basic Sciences School
Department of Chemical Sciences

Ph.D. in Chemical Sciences

# From Ring-Opening Catalytic Cycles to Material and Products: Development of an Integrated Experimental and Theoretical Approach

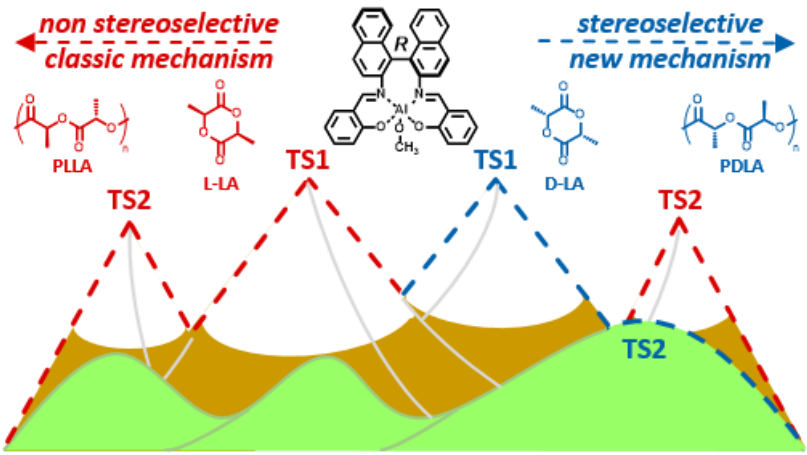


**Massimo Christian D'Alterio**

***Advisor:***
***Prof. Giovanni Talarico***

***Examiner:***
***Prof. Nadia Rega***

**XXXII Cycle** 2017 – 2020
**Coordinator:** Prof. Angela Lombardi

# Index

## Introduction



## Chapter 1. Modelling stereoselective lactide polymerization: the challenge of chiral catalyst recognition



## Chapter 2. Alternating copolymerization of $CO_2$ and cyclohexene oxide by new pyridylamidozinc(II) catalysts

## Chapter 3. Tailor-made block copolymers of L-, D-, *rac*-lactides and ε-caprolactone *via* one-pot sequential ring opening polymerization by pyridylamidozinc(II) catalysts

## Chapter 4. Base-controlled, product switch in the ruthenium-catalyzed protodecarbonylation of phthalimides: a mechanistic study



## Appendix

# Introduction

## I.1 Rational catalyst design: the philosophy of matching theory and experiment

Humans have been exploiting natural catalysts, the enzymes, for thousands of years ranging from food and beverages to pharmaceuticals.[1,2] In comparison, synthetic catalysts have appeared only recently although they have the potential to address and solve some of the greatest challenges of the 21st century, especially those related to the increasing demands of new environmentally benign materials,[3-5] low-cost and clean industrial processes[6] and last but not least sustainable energy.[7,8] Anyway, chemists do not have the same scale of time which has had the nature to develop highly efficient catalysts (namely, billions of years) since most of our environmental and energetic concerns needs to be solved as soon as possible.

Catalyst designers mainly adopt two different approaches to develop a new catalyst: one relies on the high-throughput screening of a large library of potential catalysts to explore as many candidates as possible,[9-11] and the other consists of developing a catalyst with predefined properties in an informed and rational way, possibly through a few iterations aimed at improving the catalyst's performance up to a satisfactory level.[12]

It should be noted here that the first approach received important hints from the extensive improvement of high-throughput facilities (both from experimental and theoretical point of view). Although, with the aim of saving materials and energy, the latter approach should be strongly encouraged.

In the rational design of catalysts, a valid ally of experiments is represented by computational modeling. Calculations based on Density Functional Theory (DFT)[13] is nowadays a well assessed method to model catalyzed chemical reactions.[14] The DFT modeling, giving an atomistic outlook on the reactivity, can return information not easily accessible by means of experiments. Therefore, the aim of calculations is

to explain, drive and sometimes even predict experiments. On the other hand, experiments are necessary to prove and give reliability to theoretical predictions and it is not uncommon that experiments inspire new calculations.

In this thesis we would like to demonstrate how powerful this kind of theoretical and experimental synergy can be by focusing on reactions aimed at the production of environmentally benign polymers and products of agrochemical and pharmaceutical interest. More specifically, we studied homogeneous ring-opening reactions catalyzed by earth-abundant metals (Al, Zn, Ru).

## I.2 Ring opening polymerization and copolymerization

In last decades Ring Opening Polymerization (ROP) has proved to be a useful synthetic route to technologically interesting polymers with very specific and controllable properties, for preparing synthetic variants to naturally occurring polymers or to optimize biodegradable polymers for agricultural, medicinal and pharmaceutical applications.[15-16]

It is useful to recall the IUPAC definition for the Ring-Opening Polymerization (ROP) that states "A polymerization in which a cyclic monomer yields a monomeric unit which is acyclic or contains fewer cycles than the monomer".[17] If more than one monomer is introduced in the chain we speak about Ring-Opening Copolymerization (ROCOP) whose IUPAC definition is "A Copolymerization which is a ring-opening polymerization with respect to at least one monomer".[17]

In **1** of Scheme I.1 we report a draft of the ROP process for a generic cyclic monomer M and in **2** and **3** the ROCOP processes, in particular in **2** the copolymerization involves a cyclic monomer C whilst in **3** the copolymerization involves an acyclic monomer A.

The great success of this kind of polymerization resides in the fact that several different monomers are prone to undergo the ROP and the ROCOP achieving a huge plethora of controlled microstructures.[3,14] Moreover, the favorable kinetics and

thermodynamics of this reaction enhanced by the release of the ring strain ensures mild reaction conditions.[18]

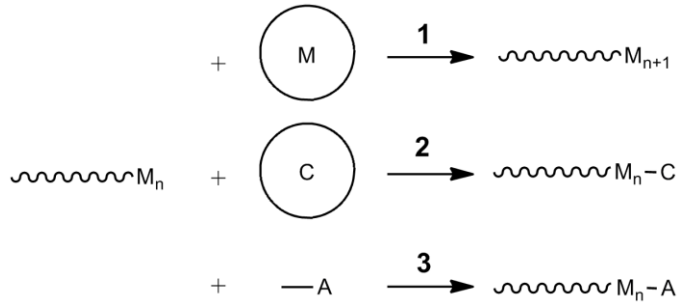


**Scheme I.1.** Ring Opening Polymerization of M (**1**), Ring Opening Copolymerization of M with a cyclic monomer C (**2**) or an acyclic monomer A (**3**).

The well-known problems related to plastic pollution are driving research in the ROP and the ROCOP toward the synthesis of biodegradable polymers with thermal and mechanical properties competitive with the non-biodegradable ones.

Polylactide (PLA) is among the polyesters produced via ROP more extensively studied for the interesting thermal and mechanical properties together with biodegradability; its industrial production is nowadays a reality[19] but the production and the properties of this polymer still needs improvement.

Pure PLA is a hard and brittle material and it is not adequate for high-temperature application ($T_g$ and $T_m$ are 60 °C and 170 °C respectively). Anyway, as the history of polypropylene (PP) teaches, huge improvement of the material can be obtained by carefully tuning the microstructure of the polymer.[20] This kind of process is closely related to the understanding of the catalytic mechanism and its possible modification.

One of the aims of this thesis is to add some pieces to the puzzle corresponding to the targeted material properties by a (suitable) tuning of the catalyst design.

In Chapter 1 we propose a model for stereoselective ROP of *rac*-LA promoted by chiral aluminum systems based on DFT calculations. The chiral catalyst recognition has been addressed as a promising route to the production of improved PLA

microstructures.[21-24] The mechanism of enantiomorphic site control dictated by the chiral catalyst shows unusual features, that add complexity and need to be taken into account when addressing the challenge of chiral catalyst recognition.

In Chapter 2 we focused on another appealing target for ROP catalysts that is the alternating copolymerization of $CO_2$ and cyclohexene oxide. Indeed, among all the global concerns, the increase in $CO_2$ concentration in the atmosphere is attracting a lot of attention and is boosting research efforts toward $CO_2$ utilization as an abundant and renewable carbon source for chemical production, although it is clear that even extensive incorporation of $CO_2$ feedstock from industrial chemical processes would have only a limited impact on the greenhouse effect problem.[29] The ring-opening copolymerization (ROCOP) of $CO_2$ with energy-rich substrates such as epoxides is a rare example of catalytic process with the potential to deliver large-scale quantities of products from carbon dioxide.[30] The copolymerization mechanism is analyzed in Chapter 2, where we report the results of a combined experimental and theoretical approach of a new family of Zn(II) complexes for the alternating copolymerization of carbon dioxide and cyclohexene oxide. The difference among the activities of the catalysts are justified by DFT calculations.

In Chapter 3 we report the experimental results of heteroleptic Zn(II) pyridylamido complexes functioning as very active catalysts for the ROP of L-, D- and *rac*-lactides and ε-caprolactone, hence developing "tailor-made" aliphatic polyesters block copolymers.[25,26] In particular, the production of stereo-diblock and stereo-multiblock PLA's has been extensively investigated together with the copolymers of LA and ε-caprolactone (CL) that appeared to be interesting materials because they combine the complementary features of the two homopolymers (the low PCL $T_g$ and the high modulus of PLA).[27.28]

## I.3 Ring opening of organic substrates

In the previous paragraph we discussed how homogeneous catalysis can play a pivotal role in the production of environmental benign and innovative materials. Here, we would like to recall that during the past decades the synthesis of many daily life chemicals (drugs, pesticides, OLED materials, commodities) has comprised at least one step involving transition metal catalysed transformation and many of these reactions nowadays are being conducted at the multiton scale (i.e. the rhodium-catalyzed hydroformylation of alkenes).[31-35] Consequently, the fundamental understanding of the metal reactivity and the discovery of new chemical reactions are still extremely appealing in view of generating sustainable and environmentally benign processes in academic and industrial laboratories. In the context of homogeneous catalysis, ruthenium is a promising alternative to precious metals[36-40] since it displays a large number of oxidation states (from +8 to -2) and coordination geometries comparable to most of the most expensive metals.[41-43] Anyway ruthenium is still far more expensive rather than the earth-abundant iron, which also shows encouraging catalytic performances.[44]

Moving in this context, it has been recently reported a general and high functional group tolerant protodecarbonylation of *N*-substituted phthalimides into amides using $[RuCl_2(p\text{-cymene})]_2$ as pre-catalyst in the presence of $K_2CO_3$ and water at high temperatures.[45]

In Chapter 4 we show detailed control experiments together with theoretical calculations at the DFT level to identify the mechanism operating in this ruthenium-catalyzed reaction, in particular, regarding the five-membered ring-opening step.

## References


1. Chemistry for Tomorrow's World (Royal Society of Chemistry, 2009).
2. Basic Research Needs for Catalysis Science (US Department of Energy, 2017).
3. Schneiderman, D. K.; Hillmyer, M. A. 50th Anniversary Perspective: There is a Great Future in Sustainable Polymers. *Macromolecules* **2017**, *50*, 3733-3749.
4. Zhang, X.; Fevre, M.; Jones, O. J.; Waymouth, R. M. Catalysis as an Enabling Science for Sustainable Polymers. *Chem. Rev*. **2018**, *118*, 839-885.
5. Zhu, Y.; Romain, C.; Williams, K. C. Sustainable Polymers from Renewable Resources. *Nature* **2016**, *540*, 354-362.
6. Dunn, P. J. The importance of Green Chemistry in Process Research and Development. *Chem. Soc. Rev.* **2012**, *41*, 1452-1461.
7. Cook, T.R.; Dogutan, D. K.; Reece, S. Y.; Surendranath Y.; Teets T. S.; Nocera, D. G. Solar Energy Supply and Storage for the Legacy and Nonlegacy Worlds. *Chem. Rev.* **2010**, *110*, 6474-6502.
8. Holladay, J.D.; Hu, J.; King, D.L.; Wang Y. An Overview of Hydrogen Production Technologies. *Catal. Today* **2009**, *139*, 244-260.
9. Holzwarth, A.; Schmidt, H.-W. & Maier, W. F. Detection of Catalytic Activity in Combinatorial Libraries of Heterogeneous Catalysts by IR Thermography. *Angew. Chem. Int. Ed.* **1998**, *37*, 2644–2647.
10. Boussie, T. R.; Diamond, G. M.; Goh C.; Hall, K. A.; LaPointe, A. M.; Leclerc, M.; Lund, C.; Murphy, V.; Shoemaker, J. A. W.; Tracht, U.; Turner, H.; Zhang, J.; Uno, T.; Rosen, R. K.; Stevens, J. C. A Fully Integrated High-Throughput Screening Methodology for the Discovery of New Polyolefin Catalysts: Discovery of a New Class of High Temperature Single-Site Group (IV) Copolymerization Catalysts. *J. Am. Chem. Soc.* **2003**, *125*, 4306–4317.
11. Taylor, S. J.; Morken, J. P. Termographic Selection of Effective Catalysts From an Encoded Polymer-Bound Library. *Science* **1998**, *280*, 267–270.

12. Falivene, L.; Cao, Z.; Petta, A.; Serra, L.; Poater, A.; Oliva, R.; Scarano, V.; Cavallo, L. Towards the Online Computer-Aided Design of Catalytic Pockets. *Nat. Chem.* **2019**, *11*, 872–879.
13. Hohenberg, P.; Kohn, W. Inhomogeneous Electron Gas. *Phys. Rev.* **1964**, *136*, B864–B871.
14. Nørskov, K. J.; Abild-Pedersen, F.; Studt, F.; Bligaard, T. Density Functional Theory in Surface Chemistry and Catalysis. *PNAS* **2011**, *108*, 937-943.
15. Nuyken, O.; Pask, D. S. Ring-Opening Polymerization-An Introductory Review. *Polymers* **2013**, *5*(2), 361-403.
16. Tschan, J.L.; Brulé, E.; Haquette, P.; Thomas, C. M.; Synthesis of Biodegradable Polymers from Renewable Resources. *Polymer Chem.* **2012**, *3*, 836.
17. IUPAC. Compendium of Chemical Terminology, 2nd ed. (the "Gold Book"). Compiled by A. D. McNaught and A. Wilkinson. Blackwell Scientific Publications, Oxford (**1997**).
18. Duda, A.; Kowalski, A. Thermodynamics and Kinetics of Ring Opening Polymerisation in Handbook of Ring Opening Polymerization Dubois P., Coulembier O., Raquez J-M., Eds.; Wiley-VCH Verlag: Weinheim, Germany, **2009**; 1–51.
19. Castro-Aguirre, E.; Iniguez-Franco, F.; Samsudin, H.; Fang, X.; Auras, R. Poly(lactic acid)—Mass Production, Processing, Industrial Applications, and End of Life. *Adv. Drug Deliv. Rev.* **2016**, *107*, 333-366.
20. Saeidlou, M. A.; Huneault, H.; Li, C.; Park, B. Poly(lactic acid) Crystallization. *Progr. Polym. Sci.* **2012**, *37*, 1657-1677.
21. Spassky, N.; Wisniewski, M.; Pluta, C.; Le Borgne, A., Highly Stereoelective Polymerization of *rac*-(D,L)-Lactide with a Chiral Schiff's Base/Aluminium Alkoxide Initiator. *Macromol. Chem. Phys.* **1996,** *197*, 2627-2637.

22. Thomas, C. M. Stereocontrolled Ring-Opening Polymerization of Cyclic Esters: Synthesis of New Polyester Microstructures. *Chem. Soc. Rev.* **2010**, *39*, 165-173.
23. Ovitt, T. M.; Coates, G. W. Stereochemistry of Lactide Polymerization with Chiral Catalysts: New Opportunities for Stereocontrol Using Polymer Exchange Mechanisms. *J. Am. Chem. Soc.* **2002**, *124*, 1316-1326.
24. Press, K.; Goldberg, I.; Kol, M. Mechanistic Insight into the Stereochemical Control of Lactide Polymerization by Salan–Aluminum Catalysts. *Angew. Chem., Int. Ed.* **2015**, *54*, 14858-14861.
25. Hillmyer, M. A.; Tolman, W. B. Aliphatic Polyester Block Polymers: Renewable, Degradable, and Sustainable. *Acc. Chem. Res.* **2014**, *47*, 2390-2396.
26. Rosen, T.; Goldberg, I.; Venditto, V.; Kol, M. Tailor-Made Stereoblock Copolymers of Poly(lactic acid) by a Truly Living Polymerization Catalyst. *J. Am. Chem. Soc.* **2016**, *138*, 12041-12044.
27. Keram, M.; Ma, H. Ring-Opening Polymerization of Lactide, ε-Caprolactone and their Copolymerization Catalyzed by β-Diketiminate Zinc Complexes. *Appl. Organometal. Chem.* **2017**, *31*, 3893.
28. Rosen, T.; Goldberg, I.; Navarra, W.; Venditto, V.; Kol, M. Block–Stereoblock Copolymers of Poly(ε-Caprolactone) and Poly(Lactic Acid), *Angew. Chem.* **2018**, *130*, 7309-7313.
29. Artz, J.; Mueller, T. E.; Thenert, K.; Kleinekorte, J.; Meys, R.; Sternberg, A.; Bardow, A.; Leitner, W. Sustainable Conversion of Carbon Dioxide: An Integrated Review of Catalysis and Life Cycle Assessment. *Chem. Rev*. **2018**, *118*, 434-504.
30. Darensburg, D. J. Making Plastics from Carbon Dioxide: Salen Metal Complexes as Catalysts for the Production of Polycarbonates from Epoxides and $CO_2$. *Chem. Rev*. **2007**, *107*, 2388-2410.
31. Noyori, R. Synthesizing our Future. *Nat. Chem.* **2009**, *1*, 5-6;
32. Sanderson, K. Chemistry: It's Not Easy Being Green. *Nature* **2011**, *469*, 18-20.

33. Sheldon, R. A. Fundamentals of Green Chemistry: Efficiency in Reaction Design. *Chem. Soc. Rev.* **2012**, *41*, 1437-1451.
34. Rothenberg, G. Catalysis: Concepts and Green Applications, Wiley-VCH, Weinheim, **2008**.
35. Franke, R.; Selen, D.; Borner, A. Applied Hydroformylation, *Chem. Rev.*, **2012**, *112*, 5675-5732.
36. Livingstone, S. E. The Chemistry of Ruthenium, Rhodium, Palladium, Osmium, Iridium and Platinum, Pergamon Texts in Inorganic Chemistry, Elsevier, **1973**.
37. Hartwig, J. F. Organotransition Metal Chemistry: From Bonding to Catalysis, University Science Books, Sausalito, **2009**.
38. Beller, M.; Bolm, C. Transition Metals for Organic Synthesis, Wiley-VCH, Weinheim, **2004**.
39. De Meijere, A.; Diederich, F. Metal-Catalyzed Cross-Coupling Reactions, 2nd ed., Wiley-VCH, Weinheim, **2004**.
40. De Meijere, A.; Braese, S.; Oestreich, M. Metal-Catalyzed Cross-Coupling Reactions and More, Wiley-VCH, Weinheim, **2014**.
41. Seddon, E. A.; Seddon, K. R. The Chemistry of Ruthenium, Elsevier Science, **1984**.
42. Murahashi, S. I. Ruthenium in Organic Synthesis, Wiley-VCH, Weinheim, Germany, **2004**.
43. Bruneau, C.; Dixneuf, P. H. Ruthenium in Catalysis, Top. Organomet. Chem., 48, Springer-Verlag, Berlin-Heidelberg, Germany, **2014**.
44. Bauer, I.; Knölker, H. J. Iron Catalysis in Organic Synthesis. *Chem. Rev.* **2015**, *115*, *9*, 3170-3387.
45. Yuan, Y.C.; Kamaraj, R.; Bruneau, C.; Labasque, T.; Roisnel, T.; Gramage-Doria, R. Unmasking Amides: Ruthenium-Catalyzed Protodecarbonylation of N-Substituted Phthalimide Derivative. *Org. Lett.* **2017**, *19*, 6404-6407.

# Chapter 1

## Modelling stereoselective lactide polymerization: the challenge of chiral catalyst recognition


## Abstract

A general model for stereoselective ROP of *rac*-LA promoted by chiral aluminum systems is reported based on DFT calculations. The mechanism of enantiomorphic site control dictated by the chiral catalyst shows unusual features, including active site reorganization on the reaction path, that add complexity and need to be taken into account when addressing the challenge of chiral catalyst recognition.


## 1.1 Introduction

Stereoselective polymerization catalysis promoted by transition metal (TM) is one of the most powerful methods to create polymeric materials with targeted properties.[1] The synergic efforts of catalyst synthesis aided by computational design has achieved extraordinary success in stereoselective α-olefin polymerization catalyzed by homogeneous TM complexes.[2,3] The depletion of non-renewable resources and recent concerns about accumulation of plastic waste in the environment propel the development of biodegradable materials produced from renewable feedstock.[4] Polylactide (PLA) is a biodegradable aliphatic polyester set to compete with the most commercially relevant polyolefins (like polyethylene and isotactic polypropylene) in terms of physical/mechanical properties.[5,6] Since pioneering work by Spassky on the stereoselective lactide polymerization promoted by chiral salen-Al complexes via ring opening polymerization (ROP) of lactide (LA),[7] intensive research efforts have been aimed at the development of better catalysts for tailored polymer microstructures.[8]

The ROP of racemic mixture (*rac*-LA) of lactide D-LA (*RR*-LA), and L-LA (*SS*-LA) can lead to isotactic PLLA (Figure 1.1-A) or PDLA (Figure 1.1-B) if the catalyst is able to select one the two monomers in the racemic mixture. Catalysts capable of produce isotactic stereoblock PLA (Figure 1.1-C) have also been reported.[9,10] Atactic microstructure is afforded from both *rac*-LA and *meso*-LA when the monomers are randomly concatenated (Figure 1.1-D). Heterotactic microstructure (Figure 1.1-E) can be afforded from both *rac*-LA[11] and *meso*-LA.[12] The obtaining from *rac*-LA is achieved when the *RR*-LA monomer and *SS*-LA monomer are concatenated in a perfect alternated fashion.

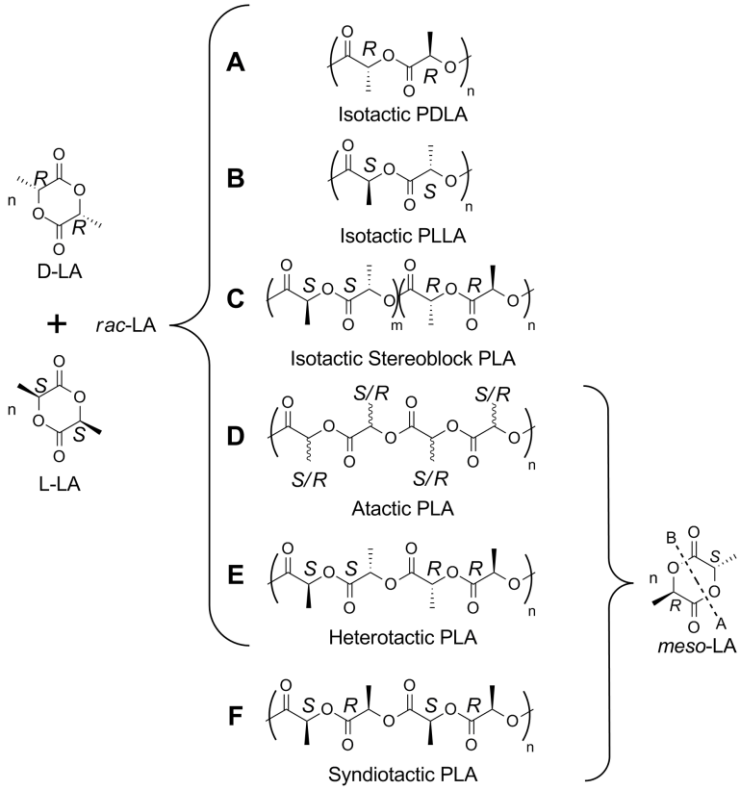


**Figure 1.1.** All the possible PLA microstructures affordable from *rac*-LA and *meso*-LA

In order to explain the *meso*-LA reactivity, it is useful to define *meso*-A as the *meso*-LA which reacts with acyl-oxygen group next to *R*-methine and *meso*-B as the

*meso*-LA which reacts with acyl-oxygen group next to *S*-methine. Heterotactic PLA is afforded by *meso*-LA if the catalyst is able to perform the ring-opening of the *meso*-LA at the two differents enantiotopic acyl-oxygen group in a perfect alternated manner (Figure 1.1-E). Syndiotactic PLA[13,14] (Figure 1.1-F) is produced from *meso*-LA if the catalyst is able to perform the ring-opening of the *meso*-LA always at the same enantiotopic acyl-oxygen group.

Spassky reported that **1** acts on *rac*-LA at 70°C in toluene ([*rac*-LA]/[*R*-cat]=50) and preferentially polymerizes D-LA (20 times faster than L-LA). At 19% of conversion (5 h) predominantly isotactic PDLA (88% of optical purity) is obtained with a $T_m$=145°C (Figure 1.2, top). At higher conversion (38%, 62.5% and 90%), as the reaction feed becomes poor in D-LA, the **1** starts to polymerize, even if slowly, the L-LA monomer. As a matter of fact, the optical purity decreases (respectively 80%, 68% and 13%). The polymer obtained at higher level of conversion shows better thermal properties ($T_m$=185°C at 13% of optical purity) since it has both PDLA and PLLA blocks, which are able to form the stereocomplex.

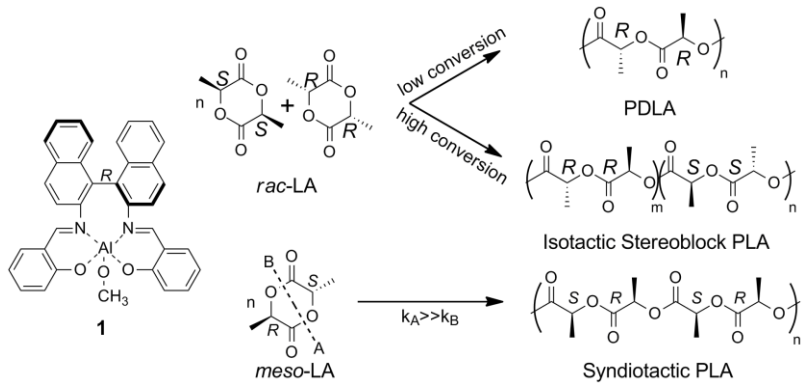


**Figure 1.2.** The Spassky system (**1**) for the stereoselective polymerization of *rac*-LA (top) and *meso*-LA (bottom).

Coates demonstrated that **1** on *meso*-LA at 70°C in toluene [*meso*-LA]/[*R*-cat]=100 results in a very stereoregular syndiotactic-PLA when the range of conversion is between 46% (5h) and 92% (40 h) (Figure 1.2, bottom).[13] Therefore the production

of a highly stereoregular syndiotactic PLA is a proof of a direct influence of the catalyst on the monomer, since a good syndiotactic PLA is produced if the rate constant of the ring opening of *meso*-A ($k_A$) is much bigger than the rate costant of *meso*-B ($k_B$) (or viceversa). Indeed, the study of the chain terminal revealed that **1** preferentially reacts with *meso*-A. It is worth noting that this catalytic system shows a higher activity toward the polymerization of *meso*-LA respect to *rac*-LA.

The two main mechanisms of chiral recognition have been identified as the enantiomorphic-site (ESM) and chain end (CEM) control; in the former the chiral catalyst environment selects preferentially one of the two enantiomers[15] while in the latter the isotactic, syndiotactic or heterotactic enchainment is due to the control by the last inserted monomeric unit.[16] Despite the intense development of new catalysts, a general model for ESM control in the ROP of *rac*-LA is still missing.[17] This is a severe drawback that may limit the rational design of suitable ligands.[2,18] Indeed a model capable of predicting stereoselectivity would obviously of great help in the search of new and improved catalysts. In this chapter we present an extended model that is capable of useful predictions.

## 1.2 Computational details

All the DFT static calculations have been performed with the Gaussian09 set of programs,[19] using the B3LYP functional of Becke and Perdew.[20,21] The electronic configuration has been described with two different layers of basis set: 6-311G(d,p)[22] at the Al center to achieve a better description of the coordination geometry and SVP with the standard split-valence basis set with a polarization function of Ahlrichs and co-workers for H, C, N, and O.[23] Stationary points were characterized using vibrational analysis, and this analysis has been also used to calculate zero-point energies and thermal (enthalpy and entropy) corrections (298.15 K, 1 bar). We obtained improved electronic energies from single-point energy calculations using a 6-311G(d,p) basis set on all the atoms, an implicit solvation

contribution to consider the dielectric constant of the solvent (PCM model,[25] toluene) and the dispersion corrections (EmpiricalDispersion=GD3BJ in the Gaussian09 E.01 package).[24] These energies added to the SVP-level thermal corrections are named $\Delta G$.

The catalyst interconversion paths for the **M3** mechanism reported in Figures 1.7-1.9 have been calculated by freezing the O-Al-O angles at different values and optimizing the geometries; once we reached the maximum of the energetic path, we started for a real transition state search without constrains (in red).

For the path corresponding to the *RR re* insertion in Al-(*RR*-chain) we also optimized the structures including the dispersion correction (Table 1.11). For each TS calculation of the second insertion, several chain conformations have been used in order to find the lowest energetic path, using as a starting point the conformation of minimum energy reported for the crystallographic structure of PLLA and PDLA.[26]

Additionally, to verify the robustness of our theoretical approach we performed several single point calculations on the rate determining step of each assembly mode by means of functionals with a different percentage of exact Hartree-Fock exchange, BP86[27,28,29] and M06-2X.[30] Finally, for BP86 and B3LYP we verified the effect of the dispersion correction by adding or not the contribution (see Tables 1.12-1.20).

## 1.3 Results and discussion

### 1.3.1 The ROP mechanism

The ROP operates with a coordination-insertion mechanism in which the first transition state (TS) for the nucleophilic addition (TS1) is followed by a second TS for the ring opening (TS2, see Scheme 1.1). The occurrence of (at least) two TSs complicates the identification of the rate limiting step (RLS) and hence the analysis of the factor(s) that give rise to the catalyst chiral control.[31] The focus of this work is to build a general model based on DFT calculations capable of explaining

stereoselection in the *rac*-LA polymerization promoted by Spassky's catalyst **1** (Figure 1.2) which has been reported as one the most efficient catalysts with ESM control.[4,7,10]

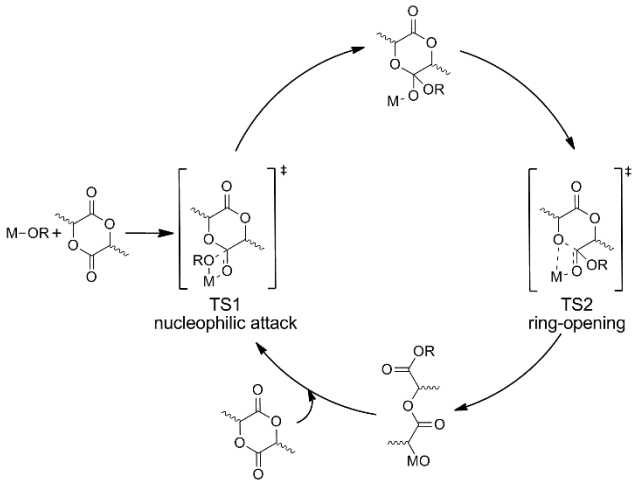


**Scheme 1.1.** Coordination-insertion mechanism for ROP steps.

As we will show in the following, the ROP stereoselection mechanism shows features unusual for ESM control, which make designing for stereoselectivity a challenging proposition. All the elements of chirality are summarized in Figure 1.3. We fixed the chirality of the catalyst, modelling the *R* enantiomer of **1** in two conformations: *fac-fac* (*ff*) and *fac-mer* (*fm*). For the *fm* conformation two *fm* wrapping modes (*fm* 1 and *fm* 2) had to be computed due to the asymmetry of the two coordination sites when monomer and growing chain are present (see Figure 1.3-a). Additional elements of chirality are the configuration of the monomer (*RR*-LA and *SS*-LA as well as the monomer enantiofaces (*re* and *si*, Figure 1.3-b) and the chirality of the growing chain dictated by the last inserted unit (Figure 1.3-c). The *meso*-LA monomer is modeled as follows: *meso*-A is *meso*-LA which reacts with acyl-oxygen group next to *R*-methine and *meso*-B is the *meso*-LA which reacts with acyl-oxygen group next to *S*-methine. Furthermore, *meso*-LA is prochiral, therefore two enantiofaces exist for each monomer (*re* and *si*) (Figure 1.3-D). The *meso*-A chain brings, in sequence, starting from the O coordinated to the Al center, a

*S*-methine and a *R*-methine. The *meso*-B chain brings, in sequence, starting from the O coordinated to the Al center, a *S*-methine and a *R*-methine (Figure 1.3-E).

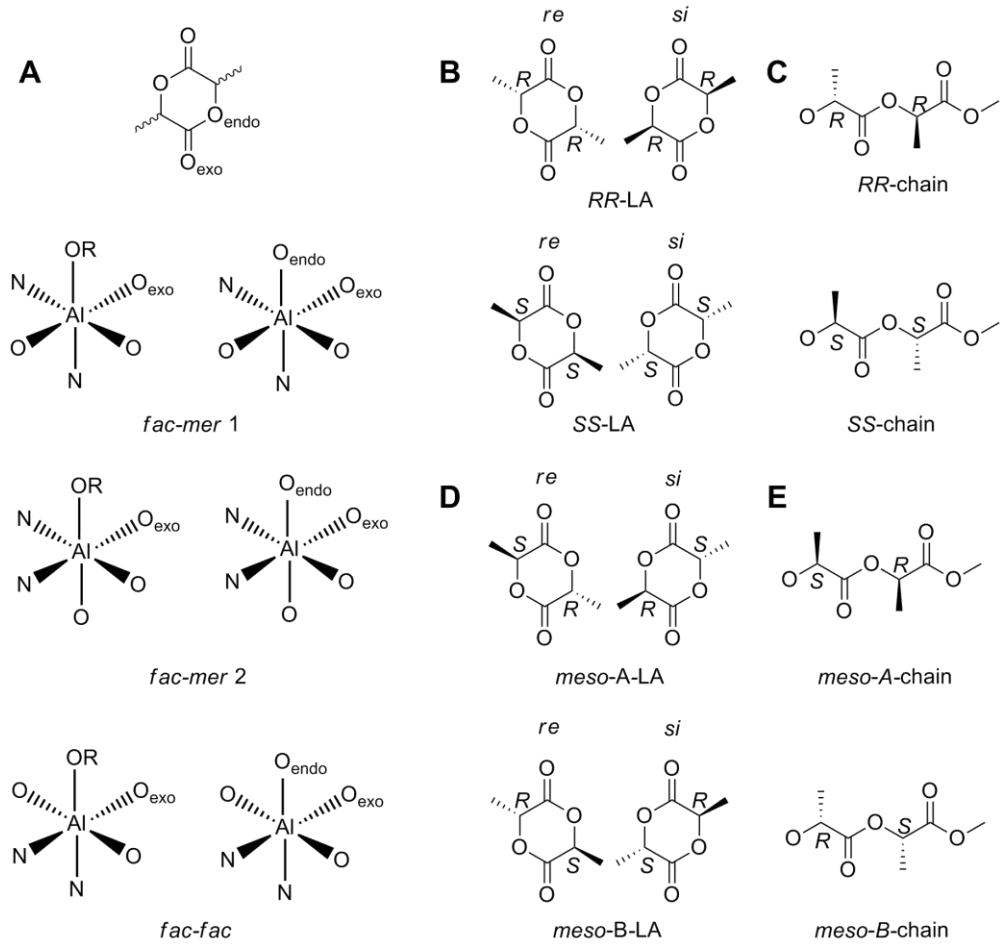


**Figure 1.3**. Elements of chirality; in A with OR we called the OMe or PLA chain; and with $O_{endo}$ and/or $O_{exo}$ we called the endocyclic and exocyclic O of lactide. In B we show the two different monomers (*RR*-LA and *SS*-LA) and in C the two different chains (*RR*-chain and *SS*-chain). In D we show *meso* monomer, assumed as *meso*-A and *meso*-B (see Figure 1.2) and in E *meso*-A chain and *meso*-B chain.

In Table 1.1 we resume the modeled PLA microstructure depending of *rac*-LA or *meso*-LA concatenation:

**Table 1.1**. All the possible assembly modes for *meso*-LA and *rac*-LA.

| Monomer | Isotactic | Heterotactic | Syndiotactic |
|---|---|---|---|
| *rac-LA* | *RR*-chain+*RR*-LA | *RR*-chain+*SS*-LA | no |
| | *SS*-chain+*SS*-LA | *SS*-chain+*RR*-LA | no |
| *meso*-LA | no | A-chain+*meso*-B LA | A-chain+*meso*-A LA |
| | no | B-chain+*meso*-A LA | B-chain+*meso*-B LA |

We summarize the LA ROP promoted by **1** within three main reaction mechanisms called mechanisms 1, 2 and 3. Mechanism 1 (**M1**) is the "classical" path reported in literature, where the wrapping mode (*ff*, *fm* 1 or *fm* 2) of the catalyst is maintained during the nucleophilic addition (TS1), in the formation of the first (Int1) and the second intermediate (Int2) and at the ring-opening step (TS2).[32-34] We modeled three corresponding reaction paths (**M1**-A-C of Figure 1.4).

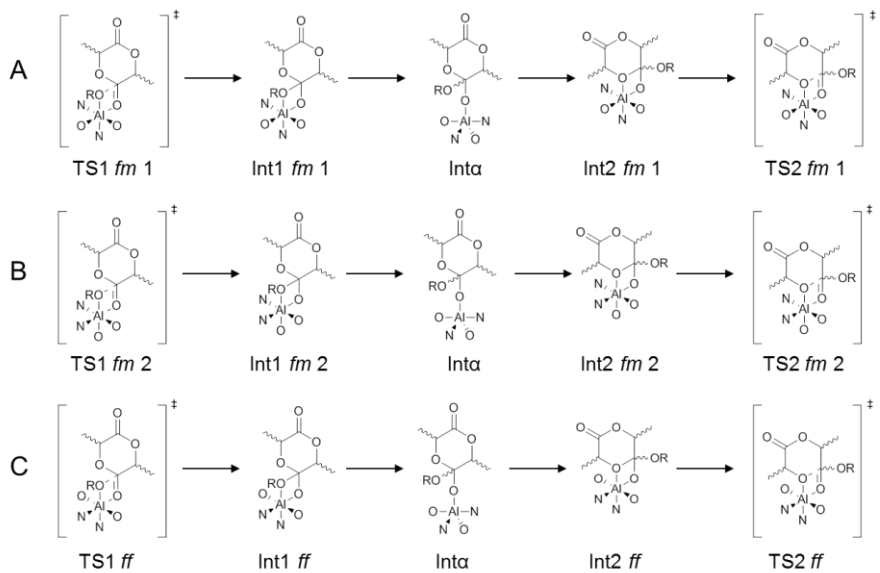


**Figure 1.4.** The three different paths computed for the mechanism 1 (**M1**).

Mechanism 2 (**M2**) still preserves the ligand wrapping mode, but it includes as novel feature a fast exchange of the monomer and growing chain between their coordination sites (**M2**-A-B Figure 1.5).[35] This effectively happens by switching the coordination of the two LA oxygens ($O_{exo}$ and $O_{endo,}$ Figure 1.3 A). This kind of rotation can easily occurs through a rotation of the dihedral angle constituted by the single Al-O-C-OR bond.

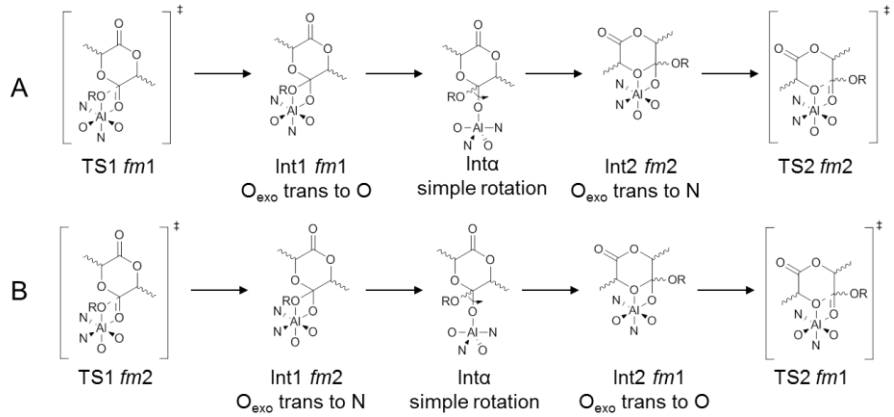


**Figure 1.5.** The two different paths computed for the mechanism 2 (**M2**).

Finally, mechanism 3 (**M3**) includes a change in ligand wrapping mode between TS1 and TS2 (**M3**-A-D Figure 1.6). The five-coordinated Intα is necessary to create the connections between the reactions path for what concern **M2** and **M3** while is not compulsory to consider it in **M1**. Moreover a new TS (here defined as TSα) for the catalyst modification has been calculated for the **M3** reaction paths.

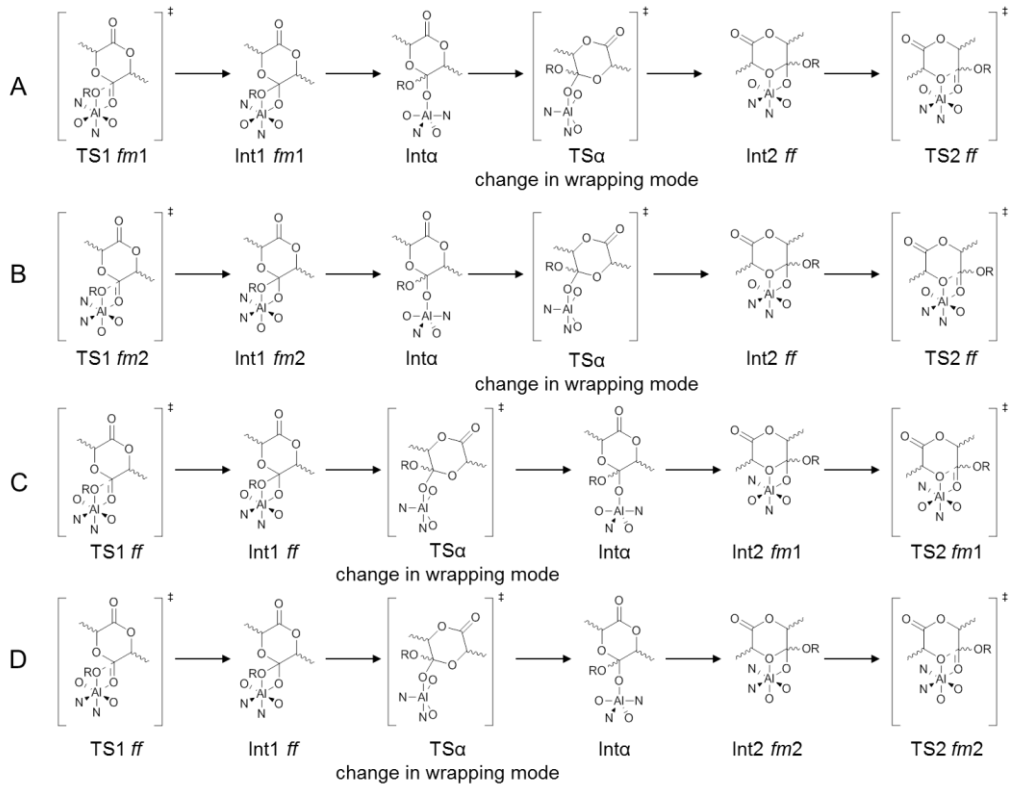


**Figure 1.6.** The four different paths computed for the mechanism 3 (**M3**).

The TSα is crucial in terms of the catalyst interconversion paths for the **M3** mechanism reported in Figure 1.6 and has been calculated by fixing the O-Al-O angles. Once we reached the maximum energetic path, we started for a real transition state search without constrains. We report the results of the interconversion of the catalyst after the first *RR*-LA insertion (Figure 1.7) and the second *RR*-LA insertion in a *RR*-chain (Figure 1.8) and they correspond to mechanism 3-A. In both cases the O-Al-O angle corresponding to TSα is approximately 150° and hence, we assume this value as the starting point for all the computed TSα.

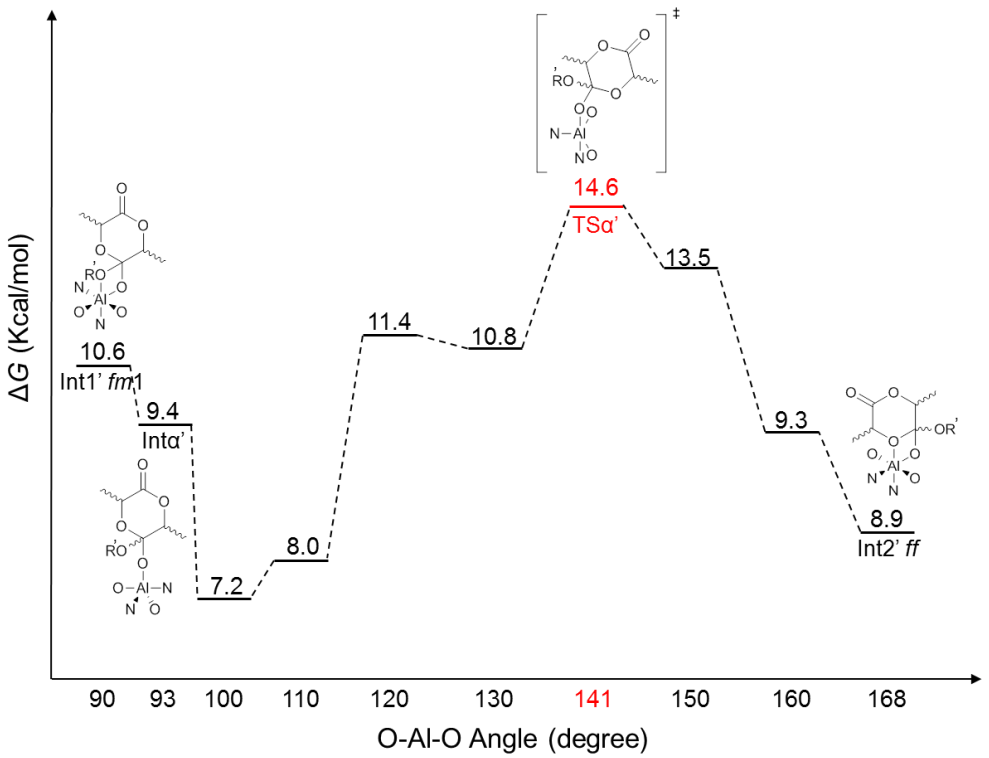


**Figure 1.7.** Free energy path for the catalyst **1** interconversion following the **M3**-A mechanism for the first *RR*-LA insertion in Al-$OCH_3$ bond. The path has been calculated by fixing the O-Al-O angle and TSα (in red) has been obtained as real transition state without constraints (see computational details).

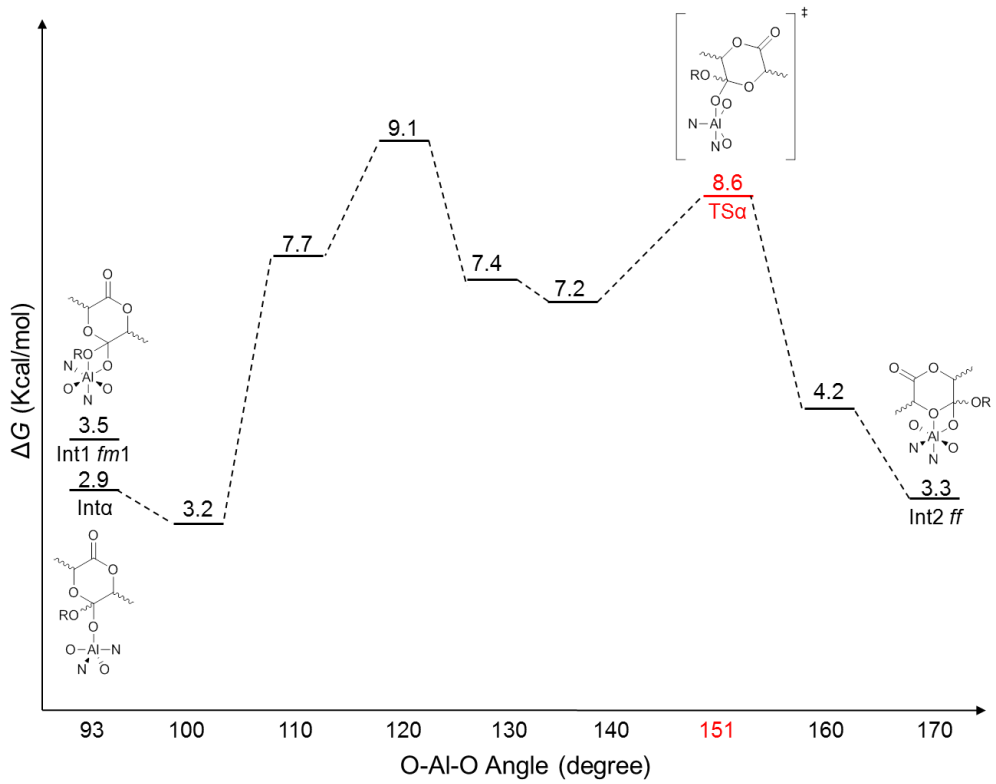


**Figure 1.8.** Free energy path for the catalyst **1** interconversion following the **M3**-A mechanism for the second *RR*-LA insertion on Al-(*RR* chain) bond. The path has been calculated by fixing the O-Al-O angle and TSα‘ (in red) has been obtained as real transition state without constraints (see computational details). The INTα’ and TSα’ are similar to INTα and TSα of Figure 1.7 but with longer polymer chain.

In Figure 1.9 we report the results for the interconversion of the catalyst after the first *SS*-LA insertion, corresponding to **M3**-D path. It is important to specify that for **M3**-C and **M3**-D the TSα occurs between Int1 FF and Intα. This is a direct consequence of the fact that in TSα the O-Al-O angle is always ≈ 150°. Therefore, by following this reaction coordinate is possible to understand why TSα is the same for all the kind of **M3**.

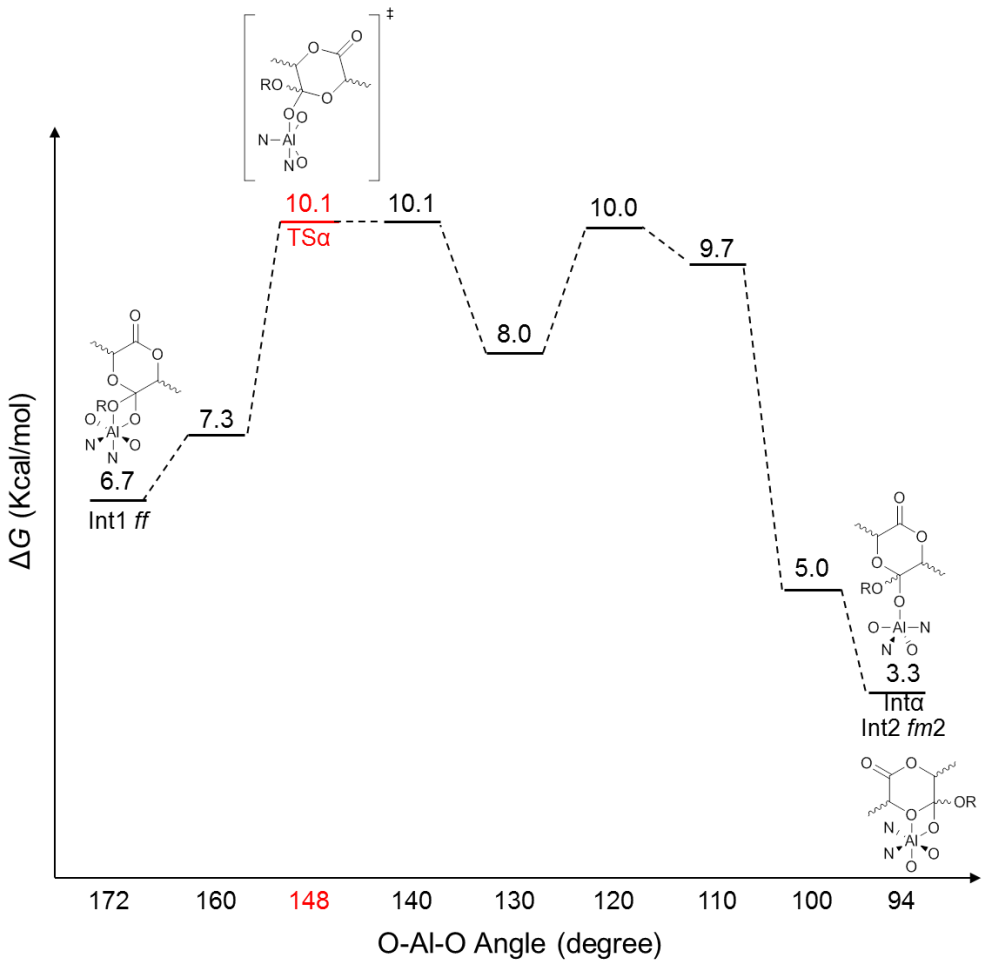


**Figure 1.9.** Free energy path for the catalyst 1 interconversion following the M3-A mechanism for the first *SS*-LA insertion in Al-$OCH_3$ bond. The path has been calculated by fixing the O-Al-O angle and TSα (in red) has been obtained as real transition state without constraints (see computational details).

### 1.3.2 Modeling of *rac*-LA polymerization

The free energies paths ($\Delta G$) for the first *RR* and *SS*-LA insertions at **1** following the lowest **M1**-**M3** reaction paths are reported in Figure 1.10, whereas the complete descriptions of all mechanistic paths are reported in Tables 1.2-1.3.

**Table 1.2.** TSs free energies ($\Delta G$, in kcal/mol) for all reaction paths computed for the first *RR*-LA insertion in Al-$OCH_3$ bond. In red the low-lying paths following the **M1**-**M3** mechanisms are reported.

| Monomer Enantioface | *RR re* | | | | Monomer Enantioface | *RR si* | | | |
|---|---|---|---|---|---|---|---|---|---|
| Mechanism 1 (**M1**) | | **TS1** | | **TS2** | Mechanism 1 (**M1**) | | **TS1** | | **TS2** |
| | A | 5.4 | | 9.3 | | A | 13.4 | | 6.4 |
| | B | 9.4 | | 7.5 | | B | 9.6 | | 6.0 |
| | C | 9.6 | | 5.2 | | C | 11.0 | | 5.0 |
| Mechanism 2 (**M2**) | | **TS1** | | **TS2** | Mechanism 2 (**M2**) | | **TS1** | | **TS2** |
| | A | 5.4 | | 7.5 | | A | 13.4 | | 6.0 |
| | B | 9.4 | | 9.3 | | B | 9.6 | | 6.4 |
| Mechanism 3 (**M3**) | | **TS1** | **TS*α*** | **TS2** | Mechanism 3 (**M3**) | | **TS1** | **TS*α*** | **TS2** |
| | A | 5.4 | 8.6 | 5.2 | | A | 13.4 | 9.3 | 5.0 |
| | B | 9.3 | 8.6 | 5.2 | | B | 9.6 | 9.3 | 5.0 |
| | C | 9.6 | 8.6 | 9.4 | | C | 11.0 | 9.3 | 6.4 |
| | D | 9.6 | 8.6 | 7.5 | | D | 11.0 | 9.3 | 6.0 |

**Table 1.3.** TSs free energies ($\Delta G$, in kcal/mol) for all reaction paths computed for the first *SS*-LA insertion in Al-$OCH_3$ bond. In red the low-lying paths following the **M1**-**M3** mechanisms are reported .

| Monomer Enantioface | *SS re* | | | | Monomer Enantioface | *SS si* | | | |
|---|---|---|---|---|---|---|---|---|---|
| Mechanism 1 (**M1**) | | **TS1** | | **TS2** | Mechanism 1 (**M1**) | | **TS1** | | **TS2** |
| | A | 10.3 | | 7.7 | | A | 8.4 | | 10.2 |
| | B | 12.1 | | 4.3 | | B | 5.7 | | 12.5 |
| | C | 9.1 | | 4.1 | | C | 8.4 | | 9.8 |
| Mechanism 2 (**M2**) | | **TS1** | | **TS2** | Mechanism 2 (**M2**) | | **TS1** | | **TS2** |
| | A | 10.3 | | 4.3 | | A | 8.4 | | 12.5 |
| | B | 12.1 | | 7.7 | | B | 5.7 | | 10.3 |
| Mechanism 3 (**M3**) | | **TS1** | **TS*α*** | **TS2** | Mechanism 3 (**M3**) | | **TS1** | **TS*α*** | **TS2** |
| | A | 10.3 | 10.1 | 4.1 | | A | 8.4 | 10.6 | 9.8 |
| | B | 12.1 | 10.1 | 4.1 | | B | 5.7 | 10.6 | 9.8 |
| | C | 9.1 | 10.1 | 7.7 | | C | 8.4 | 10.6 | 10.2 |
| | D | 9.1 | 10.1 | 4.3 | | D | 8.4 | 10.6 | 12.5 |

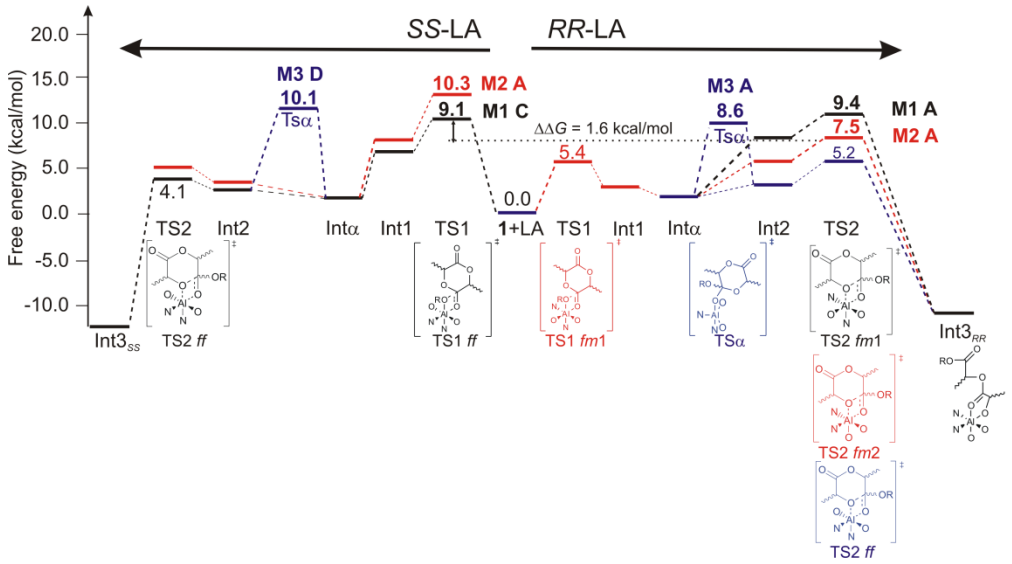


**Figure 1.10.** Free energy paths for the first *RR* (right) and *SS* (left) LA insertions at the chiral system **1** following the **M1**-**M3** mechanisms (see text).

The data reported in Figure 1.10 deserve some comments:

1) the minimum energy paths (MEP) for the *RR*- and *SS*-LA insertions are obtained for active species with different ligand coordination modes (*fm* for *RR*-LA and *ff* for *SS*-LA, respectively). This is really unusual, and we do not know other examples in stereoselective polymerization catalysis where the active site geometry depends on the relative chirality of the monomer.[36]

2) DFT calculations following the classical **M1** mechanism *did not find* preference for *RR*- versus *SS*-LA insertion promoted by system **1**. The calculated values of $\Delta G$ for *RR*-LA RLS (9.4 kcal/mol) are very close to the RLS for *SS*-LA (9.1 kcal/mol, see Figure 1.10). The stereoselection is recovered only by mechanism **M2** (1.6 kcal/mol) with **M3** (0.5 kcal/mol) acting as a further refinement.

These findings are finally confirmed by modeling the second LA insertions to achieve a complete picture for the ROP stereoselectivity process.[37] The low-lying $\Delta G$ for the second *RR*- and *SS*-LA insertions at **1** following the **M1**-**M3** mechanisms

are reported in Figure 1.11 whereas the complete descriptions of all mechanistic paths are reported in Tables 1.4-1.7.

**Table 1.4.** TSs free energies ($\Delta G$, in kcal/mol) for all reaction paths computed for the second *RR*-LA insertion in Al-(*RR* chain) bond. In red the low-lying paths following the **M1**-**M3** mechanisms are reported. In parenthesis we report the energies for the optimized structures including the D3 empirical dispersion with the Becke-Johnson dumping function.

| Chain Monomer Enantioface | *RR* *re* | | | | Chain Monomer Enantioface | *RR* *si* | | | |
|---|---|---|---|---|---|---|---|---|---|
| Mechanism 1 (**M1**) | | **TS1** | | **TS2** | Mechanism 1 (**M1**) | | **TS1** | | **TS2** |
| | A | 12.7 | | 16.3 | | A | 19.9 | | 14.4 |
| | B | 20.0 | | 14.4 | | B | 17.6 | | 13.0 |
| | C | 17.1 | | 10.8 | | C | 17.9 | | 13.1 |
| Mechanism 2 (**M2**) | | **TS1** | | **TS2** | Mechanism 2 (**M2**) | | **TS1** | | **TS2** |
| | A | 12.7 | | 14.4 | | A | 19.9 | | 13.0 |
| | B | 20.0 | | 16.3 | | B | 17.6 | | 14.4 |
| Mechanism 3 (**M3**) | | **TS1** | **TSα** | **TS2** | Mechanism 3 (**M3**) | | **TS1** | **TSα** | **TS2** |
| | A | 12.7 | 14.6 | 10.8 | | A | 19.9 | 22.2 | 13.1 |
| | B | 20.0 | 14.6 | 10.8 | | B | 17.6 | 22.2 | 13.1 |
| | C | 17.1 | 14.6 | 16.3 | | C | 17.9 | 22.2 | 14.4 |
| | D | 17.1 | 14.6 | 14.9 | | D | 17.9 | 22.2 | 13.0 |

**Table 1.5.** TSs free energies (Δ*G*, in kcal/mol) for all reaction paths computed for the second *RR*-LA insertion in Al-(*SS* chain) bond. In red the low-lying paths following the **M1**-**M3** mechanisms are reported.

| Chain<br>Monomer<br>Enantioface | *SS*<br>*RR*<br>*re* | | | | Chain<br>Monomer<br>Enantioface | *SS*<br>*RR*<br>*si* | | | |
|---|---|---|---|---|---|---|---|---|---|
| Mechanism 1<br>(**M1**) | | **TS1** | | **TS2** | Mechanism 1<br>(**M1**) | | **TS1** | | **TS2** |
| | A | 14.9 | | 19.4 | | A | 21.3 | | 15.4 |
| | B | 19.6 | | 15.9 | | B | 17.9 | | 12.5 |
| | C | 17.8 | | 13.9 | | C | 19.3 | | 13.0 |
| Mechanism 2<br>(**M2**) | | **TS1** | | **TS2** | Mechanism 2<br>(**M2**) | | **TS1** | | **TS2** |
| | A | 14.9 | | 15.9 | | A | 21.3 | | 12.5 |
| | B | 19.6 | | 19.4 | | B | 17.8 | | 15.4 |
| Mechanism 3<br>(**M3**) | | **TS1** | **TSα** | **TS2** | Mechanism 3<br>(**M3**) | | **TS1** | **TSα** | **TS2** |
| | A | 17.9 | 14.1 | 19.4 | | A | 19.3 | 17.3 | 15.4 |
| | B | 17.9 | 14.1 | 15.9 | | B | 19.3 | 17.3 | 12.5 |
| | C | 14.9 | 14.1 | 13.9 | | C | 21.3 | 17.3 | 13.0 |
| | D | 19.6 | 14.1 | 13.9 | | D | 17.8 | 17.3 | 13.0 |

**Table 1.6.** TSs free energies (Δ*G*, in kcal/mol) for all reaction paths computed for the second *SS*-LA insertion in Al-(*SS* chain) bond. In red the low-lying paths following the **M1**-**M3** mechanisms are reported .

| Chain Monomer Enantioface | *SS* *SS* *re* | | | | Chain Monomer Enantioface | *SS* *SS* *si* | | | |
|---|---|---|---|---|---|---|---|---|---|
| Mechanism 1 (**M1**) | | **TS1** | | **TS2** | Mechanism 1 (**M1**) | | **TS1** | | **TS2** |
| | A | 20.3 | | 18.5 | | A | 17.3 | | 21.9 |
| | B | 20.4 | | 15.3 | | B | 18.9 | | 19.1 |
| | C | 16.2 | | 12.1 | | C | 18.4 | | 17.7 |
| Mechanism 2 (**M2**) | | **TS1** | | **TS2** | Mechanism 2 (**M2**) | | **TS1** | | **TS2** |
| | A | 20.3 | | 15.3 | | A | 17.3 | | 19.1 |
| | B | 20.4 | | 18.5 | | B | 18.9 | | 21.9 |
| Mechanism 3 (**M3**) | | **TS1** | **TSα** | **TS2** | Mechanism 3 (**M3**) | | **TS1** | **TSα** | **TS2** |
| | A | 16.2 | 17.3 | 18.5 | | A | 18.4 | 16.4 | 21.9 |
| | B | 16.2 | 17.3 | 15.3 | | B | 18.4 | 16.4 | 19.1 |
| | C | 20.3 | 17.3 | 12.1 | | C | 17.3 | 16.4 | 17.7 |
| | D | 20.4 | 17.3 | 12.1 | | D | 18.9 | 16.4 | 17.7 |

**Table 1.7.** TSs free energies (Δ*G*, in kcal/mol) for all reaction paths computed for the second *RR*-LA insertion in Al-(*SS* chain) bond. In red the low-lying paths following the **M1**-**M3** mechanisms are reported.

| Chain Monomer Enantioface | *RR SS re* | | | | Chain Monomer Enantioface | *RR SS si* | | | |
|---|---|---|---|---|---|---|---|---|---|
| Mechanism 1 (**M1**) | | **TS1** | | **TS2** | Mechanism 1 (**M1**) | | **TS1** | | **TS2** |
| | A | 16.8 | | 14.1 | | A | 14.5 | | 20.2 |
| | B | 22.7 | | 11.0 | | B | 15.9 | | 20.8 |
| | C | 15.2 | | 10.1 | | C | 17.0 | | 17.9 |
| Mechanism 2 (**M2**) | | **TS1** | | **TS2** | Mechanism 2 (**M2**) | | **TS1** | | **TS2** |
| | A | 16.8 | | 11.0 | | A | 14.5 | | 20.8 |
| | B | 22.7 | | 14.1 | | B | 15.9 | | 20.2 |
| Mechanism 3 (**M3**) | | **TS1** | **TSα** | **TS2** | Mechanism 3 (**M3**) | | **TS1** | **TSα** | **TS2** |
| | A | 15.2 | 15.7 | 14.1 | | A | 17.0 | 15.6 | 20.2 |
| | B | 15.2 | 15.7 | 11.0 | | B | 17.0 | 15.6 | 20.8 |
| | C | 16.8 | 15.7 | 10.1 | | C | 14.5 | 15.6 | 17.9 |
| | D | 22.7 | 15.7 | 10.1 | | D | 15.9 | 15.6 | 17.9 |

The Δ*G* paths reported in Figure 1.11 show that the experimental *RR*-LA preference of around 2.0 kcal/mol[38] is due to both the **M2** and **M3** mechanisms which are almost isoenergetic (14.4 and 14.6 kcal/mol) and respectively 1.8 and 1.6 kcal/mol lower than the *SS* polymerization. The free energies of activation differences relative to the most favored mechanism (ΔΔ*G)* depending on the assembly mode are reported in Table 1.8. Our DFT calculations show that the occasional insertion of the *SS*-LA, although feasible (entry 4 of Table 1.8) is likely to be corrected by the next *RR*-LA (entry 3 of Table 1.8) before the formation of *SS*-blocks (entry 5 of Table 1.8) achieved after consuming the *RR*-LA in the feed. Overall, the results of Table 1.8 nicely match, and at the same time explain, the experimental kinetic data reported by Spassky.[7,38]

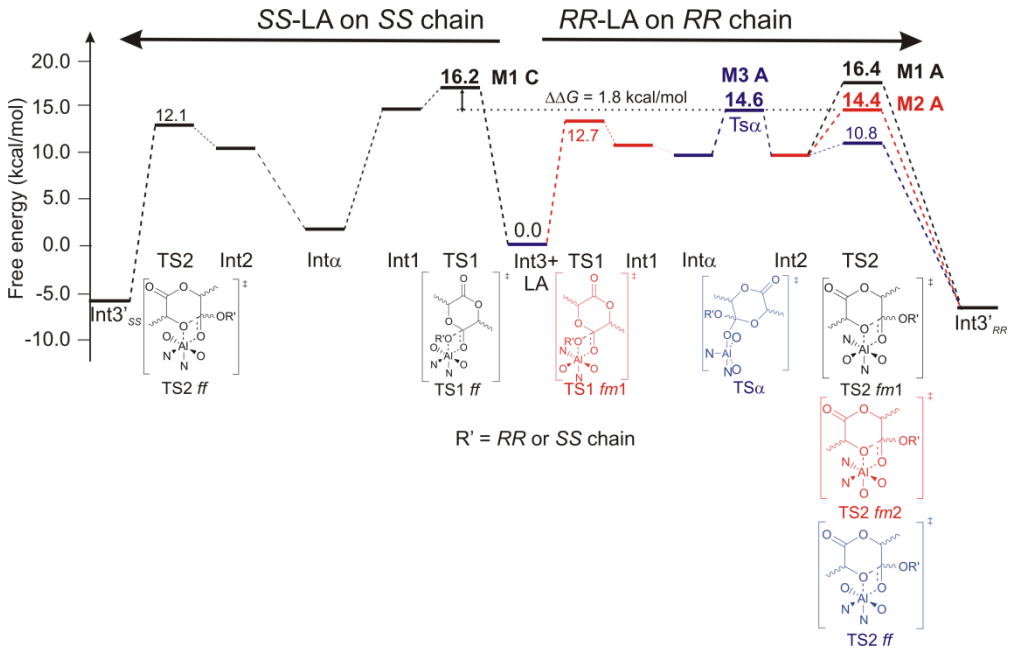


**Figure 1.11.** Free energy paths for the second *RR*- and *SS*-LA insertions at the chiral system **1** following the **M1**-**M3** mechanisms (see text).

**Table 1.8.** Free energies of activation for the RLS steps ($\Delta G^{\ddagger}_{RLS}$) and activation free energy differences ($\Delta\Delta G$) relative to the most stable path for the *RR*- and *SS*-LA insertions at 1 depending on the assembly mode.[37]

| Entry | Assembly mode | $\Delta G^{\ddagger}_{RLS}$ (kcal/mol) | $\Delta\Delta G$ (kcal/mol) |
|---|---|---|---|
| 1 | *RR chain* + *RR* | 14.4 (TS2) | 0.0 |
| 2 | *RR chain* + *RR* | 14.6 (TSα) | 0.2 |
| 3 | *SS chain* + *RR* | 14.9 (TS1) | 0.5 |
| 4 | *RR chain* + *SS* | 15.2 (TS1) | 0.8 |
| 5 | *SS chain* + *SS* | 16.2 (TS1) | 1.8 |

A more detailed analysis of the RLS TSs for the **M1**-**M3** mechanisms yields some insights useful in rational catalyst design. In Figure 1.12 we report the geometries for the RLS of **M3** (TSα, Figure 1.12-A) and **M2** (TS2, Figure 1.12-B) both leading

to *RR*-LA insertion compared with the RLS for the *SS*-LA insertion (TS1 of **M1**, Figure 1.12-C). The energetic balance of these three TSs is crucial for the ROP stereoselection and may explain several experimental results. First of all, the TSα (Figure 1.12-A) free energy is dependent on the flexibility of the backbone linker (see Figures 1.7-1.9 and Table 1.21 in paragraph 1.3.4 for major details); decreasing the flexibility by using a shorter linker[39] increases its energy. This result enlightens the experimental observation of Gibson et al. on the higher isoselectivity obtained by increasing the flexibility of backbone linker for aluminum salen-type complexes.[40] Secondly, the (small) $\Delta\Delta G$ differences of Table 1.8 indicate that subtle ligand modification may induce a significant switch in tacticity control.[41,42] Finally, the classical design strategy by using repulsive non-bonded interaction to increase the energy of RLS for the *SS*- insertion (e.g. by adding substituents at the phenolate *ortho* position, see Figure 1.12-C) is less straightforward because of the corresponding increasing of the TS2 energy for *RR*- insertion following the **M2** mechanism (see the distance of 3.34 Å in Figure 1.12-B between the exocyclic O lactide and the *ortho* position of the salen-moiety).[40,42]

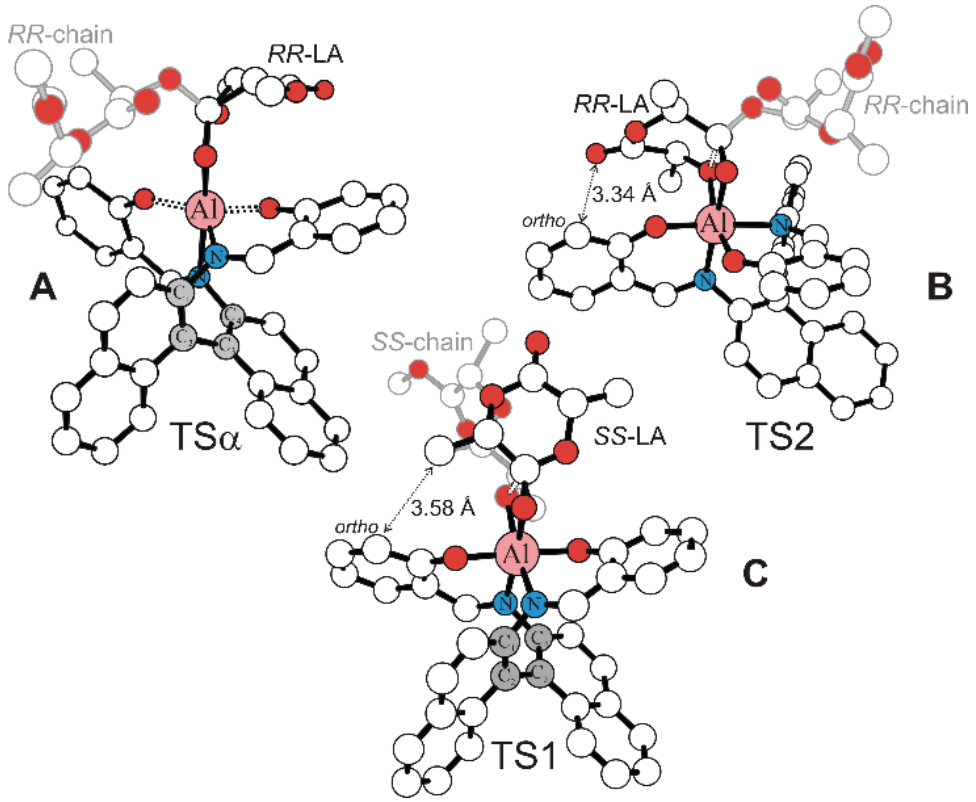


**Figure 1.12.** TSs geometries for the RLS of *RR*-LA insertion corresponding to the TSα (**A**) and TS2 (**B**) following the **M3** and **M2** mechanisms compared with the RLS of *SS*-LA insertion corresponding to the TS1 following the **M1** mechanism (**C**). The backbone linker of four C atoms is reported in **A** and **C**. H atoms omitted for clarity. Distances in Å.

### 1.3.3 Modeling of first *meso*-LA insertion

As mentioned in the introduction, the system **1** is stereoselective also in polymerization of *meso*-LA. In paragraph 1.3.2 we demonstrated the microscopic intricacies at the basis of mechanism(s) acting toward the polymerization of *rac*-LA, now the proposal is to confirm our findings by modeling *meso*-LA polymerization by adopting the same methodology. The complete descriptions of all mechanistic paths are reported in Tables 1.9-1.10.

**Table 1.9.** TSs free energies ($\Delta G$, in kcal/mol) for all reaction paths computed for the first *meso*-A-LA insertion in Al-$OCH_3$ bond. In red the low-lying paths following the **M1**-**M3** mechanisms are reported.

| Monomer Enantioface | *meso*-A *re* | | | | Monomer Enantioface | *meso*-A *si* | | | |
|---|---|---|---|---|---|---|---|---|---|
| Mechanism 1 (**M1**) | | **TS1** | | **TS2** | Mechanism 1 (**M1**) | | **TS1** | | **TS2** |
| | A | 4.6 | | 7.6 | | A | 10.6 | | 8.2 |
| | B | 8.0 | | 7.2 | | B | 7.4 | | 6.0 |
| | C | 7.6 | | 4.2 | | C | 10.8 | | 6.5 |
| Mechanism 2 (**M2**) | | **TS1** | | **TS2** | Mechanism 2 (**M2**) | | **TS1** | | **TS2** |
| | A | 4.6 | | 7.2 | | A | 10.6 | | 6.0 |
| | B | 8.0 | | 7.6 | | B | 7.4 | | 8.2 |
| Mechanism 3 (**M3**) | | **TS1** | **TSα** | **TS2** | Mechanism 3 (**M3**) | | **TS1** | **TSα** | **TS2** |
| | A | 4.6 | 10.3 | 4.2 | | A | 10.6 | 7.1 | 6.5 |
| | B | 8.0 | 10.3 | 4.2 | | B | 7.4 | 7.1 | 6.5 |
| | C | 8.0 | 10.3 | 7.6 | | C | 10.8 | 7.1 | 12.0 |
| | D | 8.0 | 10.3 | 7.2 | | D | 10.8 | 7.1 | 10.4 |

**Table 1.10.** TSs free energies (Δ*G*, in kcal/mol) for all reaction paths computed for the first *meso*-B-LA insertion in Al-$OCH_3$ bond. In red the low-lying paths following the **M1**-**M3** mechanisms are reported.

| Monomer Enantioface | *meso*-B *re* | | | | Monomer Enantioface | *meso*-B *si* | | | |
|---|---|---|---|---|---|---|---|---|---|
| Mechanism 1 (**M1**) | | **TS1** | | **TS2** | Mechanism 1 (**M1**) | | **TS1** | | **TS2** |
| | A | 9.4 | | 8.8 | | A | 6.6 | | 12.0 |
| | B | 11.9 | | 5.0 | | B | 4.6 | | 10.4 |
| | C | 9.0 | | 5.0 | | C | 8.2 | | 10.8 |
| Mechanism 2 (**M2**) | | **TS1** | | **TS2** | Mechanism 2 (**M2**) | | **TS1** | | **TS2** |
| | A | 9.4 | | 5.0 | | A | 6.6 | | 10.4 |
| | B | 11.9 | | 8.8 | | B | 4.6 | | 12.0 |
| Mechanism 3 (**M3**) | | **TS1** | **TSα** | **TS2** | Mechanism 3 (**M3**) | | **TS1** | **TSα** | **TS2** |
| | A | 9.4 | 8.2 | 5.0 | | A | 6.6 | 10.5 | 10.8 |
| | B | 11.9 | 8.2 | 5.0 | | B | 4.6 | 10.5 | 10.8 |
| | C | 9.0 | 8.2 | 8.8 | | C | 8.2 | 10.5 | 12.0 |
| | D | 9.0 | 8.2 | 5.0 | | D | 8.2 | 10.5 | 10.4 |

The data reported in Table 1.9 and Table 1.10 deserve some comments:

DFT calculations following both mechanism 1 (**M1**) and mechanism 2 (**M2**) found a preference for *meso*-A versus *meso*-B insertion promoted by system **1**. In particular, the calculated Δ*G* values for the RLS of *meso*-A **M1** (7.6 kcal/mol, see Table 1.9) and **M2** (7.2 kcal/mol, see Table 1.9) are both lower than the RLS for *meso*-B-LA (9.0 kcal/mol, see Table 1.10). The stereoselection can be evaluated as 1.8 kcal/mol by **M2**. A further look to the optimized structures of the RLS is helpful to explain the reason why system **1** reacts preferentially with *meso*-A rather than *meso*-B. In the RLS of *meso-B* insertions (right of Figure 1.13) one of the two methyls clashes with C in *ortho* position of the SALEN moiety. It is worth to note that this kind of interaction is the same found to be responsible of the stereoselectivity of system **1** catalyst toward *rac*-LA polymerization.

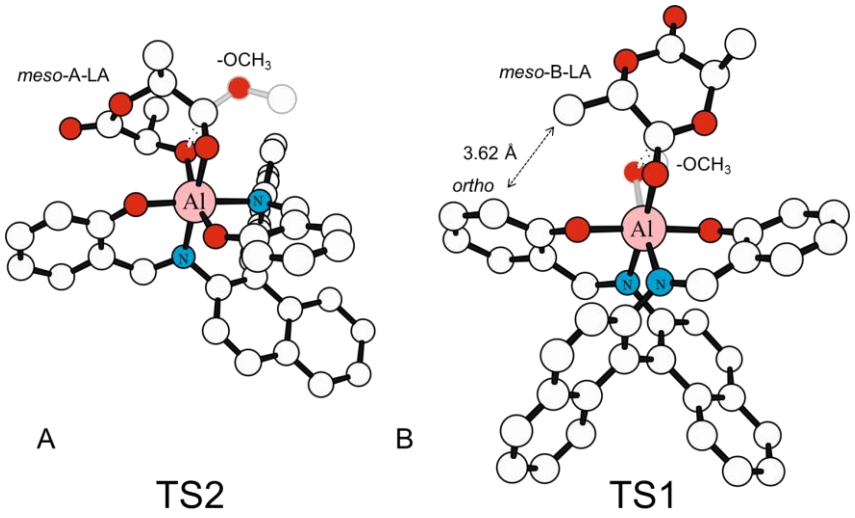


**Figure 1.13.** TSs geometries for the RLS of *meso*-A-LA insertion corresponding to the TS2 (**A**) following the **M2** mechanism compared with the RLS *meso*-B-LA insertion corresponding to the TS1 following the **M1** mechanism (**B**). H atoms omitted for clarity. Distances in Å.

This theoretical result is in nice agreement with the experimental results reported by Coates, who found that system **1** preferentially opens the *meso*-LA which reacts with acyl-oxygen group next to *R*-methine (*meso*-A) by studying the chain-terminal.[9] It is worth to note if we consider the effect of the chain on the stereoselectivity negligible as demonstrated for *rac*-LA polymerization modeling (see paragraph 1.3.2, Table 1.8), our results will reproduce also the experimental syndiotactic microstructure of the polymer by assuming that the sequential insertion of *meso*-A is the most rapid. Further study on the second insertion will follow.

### 1.3.4 Benchmark of the model

In this paragraph the results of additional calculations to assess the robustness of our method and model are shown.

In Table 1.11 we report the results for the path corresponding to the *RR re* insertion in Al-(*RR*-chain) by optimizing the structures including the dispersion correction, but no significant change in trend are observed rather than the optimization without dispersion.

**Table 1.11.** Comparison between the TSs free energies (Δ*G*, in kcal/mol) for the optimized structures of all the reaction paths computed for the second *RR*-LA *re* insertion in Al-(*RR* chain) bond including or not (see values in parenthesis) the D3 empirical dispersion with the Becke-Johnson dumping function. In red the low-lying paths following the **M1**-**M3** mechanisms are reported.

| Chain<br>Monomer<br>Enantioface | *RR*<br>*RR*<br>*re* | | | |
|---|---|---|---|---|
| Mechanism 1 (**M1**) | | **TS1** | | **TS2** |
| | A | (12.7) 11.5 | | (16.3) 14.5 |
| | B | (19.5) 20.0 | | (14.4) 13.2 |
| | C | (17.1 ) 16.6 | | (10.8) 10.1 |
| Mechanism 2 (**M2**) | | **TS1** | | **TS2** |
| | A | (12.7) 11.5 | | (14.4) 13.2 |
| | B | (20.0) 19.5 | | (16.3) 14.5 |
| Mechanism 3 (**M3**) | | **TS1** | **TSα** | **TS2** |
| | A | (12.7) 11.5 | (14.6) 14.3 | (10.8) 10.1 |
| | B | (20.0) 19.5 | (14.6) 14.3 | (10.8) 10.1 |
| | C | (17.1) 16.6 | (14.6) 14.3 | (16.3) 14.5 |
| | D | (17.1) 16.6 | (14.6) 14.3 | (14.9) 13.2 |

With the aim to expand the computational approach we performed several single point calculations on the rate determining step of each assembly mode (see Table 1.8) by means of functionals with a different percentage of exact Hartree-Fock exchange, BP86[27,28,29] and M06-2X,[30] for BP86 and B3LYP we verified the effect of the dispersion correction by adding or not the contribution (Tables 1.12-1.20). Overall the stereoselectivity is well reproduced providing single point calculations with D3 correction or M06-2X are used. Small differences are reported for the TSα

and TS2 depending of the computational approach. In any case, the two mechanisms we proposed for the stereoselection are almost isoenergetic therefore it is reasonable that differences depending on the functional used can sort out.

**Table 1.12.** Free energies of activation for the RLS steps ($\Delta G^{\ddagger}_{RLS}$) and activation free energy differences ($\Delta\Delta G$) relative to the most stable path for the *RR*- and *SS*-LA insertions at **1** depending on the assembly mode. Geometry optimization performed at B3LYP level with 6-311G(d,p) basis set on Al and SVP on C, H, N and O and single point calculations performed at B3LYP/PCM(Toluene) level with 6-311G(d,p) on all the atoms.

| Entry | Assembly mode | $\Delta G^{\ddagger}_{RLS}$(kcal/mol) | $\Delta\Delta G$ (kcal/mol) |
|---|---|---|---|
| 1 | *RR chain* + *RR* | 25.7 (TSα) | 0.0 |
| 2 | *SS chain* + *RR* | 27.1 (TS1) | 1.4 |
| 3 | *SS chain* + *SS* | 30.9 (TS1) | 5.2 |
| 4 | *RR chain* + *RR* | 31.7 (TS2) | 6.0 |
| 5 | *RR chain* + *SS* | 31.8 (TS1) | 6.1 |

**Table 1.13.** Free energies of activation for the RLS steps ($\Delta G^{\ddagger}_{RLS}$) and activation free energy differences ($\Delta\Delta G$) relative to the most stable path for the *RR*- and *SS*-LA insertions at **1** depending on the assembly mode. Geometry optimization performed at B3LYP level with 6-311G(d,p) basis set on Al and SVP on C, H, N and O and single point calculations performed at BP86/D3BJ/PCM(Toluene) level with 6-311G(d,p) on all the atoms.

| Entry | Assembly mode | $\Delta G^{\ddagger}_{RLS}$(kcal/mol) | $\Delta\Delta G$ (kcal/mol) |
|---|---|---|---|
| 1 | *RR chain* + *RR* | 11.1 (TS2) | 0.0 |
| 2 | *RR chain* +*SS* | 12.1 (TS1) | 1.0 |
| 3 | *SS chain* + *RR* | 13.0 (TS1) | 1.9 |
| 4 | *SS chain* + *SS* | 13.4 (TS1) | 2.3 |
| 5 | *RR chain* + *RR* | 15.5 (TSα) | 4.4 |

**Table 1.14.** Free energies of activation for the RLS steps ($\Delta G^{\ddagger}_{RLS}$) and activation free energy differences ($\Delta\Delta G$) relative to the most stable path for the *RR*- and *SS*-LA insertions at **1** depending on the assembly mode. Geometry optimization performed at B3LYP level with 6-311G(d,p) basis set on Al and SVP on C, H, N and O and single point calculations performed at BP86/PCM(Toluene) level with 6-311G(d,p) on all the atoms.

| Entry | Assembly mode | $\Delta G^{\ddagger}_{RLS}$(kcal/mol) | $\Delta\Delta G$ (kcal/mol) |
|---|---|---|---|
| 1 | *SS chain* + *RR* | 26.1 (TS1) | 0.0 |
| 2 | *RR chain* + *RR* | 27.6 (TSα) | 1.5 |
| 3 | *SS chain* + *SS* | 29.3 (TS1) | 3.2 |
| 4 | *RR chain* + *RR* | 29.8 (TS2) | 3.7 |
| 5 | *RR chain* + *SS* | 30.1 (TS1) | 4.0 |

**Table 1.15.** Free energies of activation for the RLS steps ($\Delta G^{\ddagger}_{RLS}$) and activation free energy differences ($\Delta\Delta G$) relative to the most stable path for the *RR*- and *SS*-LA insertions at **1** depending on the assembly mode. Geometry optimization performed at B3LYP level with 6-311G(d,p) basis set on Al and SVP on C, H, N and O and single point calculations performed at M06-2X/PCM(Toluene) level with 6-311G(d,p) on all the atoms.

| Entry | Assembly mode | $\Delta G^{\ddagger}_{RLS}$(kcal/mol) | $\Delta\Delta G$ (kcal/mol) |
|---|---|---|---|
| 1 | *RR chain* + *RR* | 11.8 (TSα) | 0.0 |
| 2 | *RR chain* + *RR* | 14.1 (TS2) | 2.3 |
| 3 | *SS chain* + *RR* | 14.6 (TS1) | 2.8 |
| 4 | *RR chain* + *SS* | 14.9 (TS1) | 3.1 |
| 5 | *SS chain* + *SS* | 16.3 (TS1) | 4.5 |

**Table 1.16.** Free energies of activation for the RLS steps ($\Delta G^{\ddagger}_{RLS}$) and activation free energy differences ($\Delta\Delta G$) relative to the most stable path for the *RR*- and *SS*-LA insertions at **1** depending on the assembly mode. Geometry optimization performed at B3LYP/D3BJ level with 6-311G(d,p) basis set on Al and SVP on C, H, N and O and single point calculations performed at B3LYP/D3BJ/PCM(Toluene) level with 6-311G(d,p) on all the atoms.

| Entry | Assembly mode | $\Delta G^{\ddagger}_{RLS}$(kcal/mol) | $\Delta\Delta G$ (kcal/mol) |
|---|---|---|---|
| 1 | *SS chain* + *RR* | 12.5 (TS1) | 0.0 |
| 2 | *RR chain* + *RR* | 13.2 (TS2) | 0.7 |
| 3 | *RR chain* + *RR* | 14.3 (TSα) | 1.8 |
| 4 | *SS chain* + *SS* | 14.9 (TS1) | 2.4 |
| 5 | *RR chain* + *SS* | 15.1 (TS1) | 3.6 |

**Table 1.17.** Free energies of activation for the RLS steps ($\Delta G^{\ddagger}_{RLS}$) and activation free energy differences ($\Delta\Delta G$) relative to the most stable path for the *RR*- and *SS*-LA insertions at **1** depending on the assembly mode. Geometry optimization performed at B3LYP/D3BJ level with 6-311G(d,p) basis set on Al and SVP on C, H, N and O and single point calculations performed at B3LYP/PCM(Toluene) level with 6-311G(d,p) on all the atoms.

| Entry | Assembly mode | $\Delta G^{\ddagger}_{RLS}$(kcal/mol) | $\Delta\Delta G$ (kcal/mol) |
|---|---|---|---|
| 1 | *RR chain* + *RR* | 24.4 (TSα) | 0.0 |
| 2 | *SS chain* + *RR* | 25.9 (TS1) | 1.5 |
| 3 | *SS chain* + *SS* | 27.2 (TS1) | 2.8 |
| 4 | *RR chain* + *RR* | 27.7 (TS2) | 3.3 |
| 5 | *RR chain* + *SS* | 30.3 (TS1) | 4.9 |

**Table 1.18.** Free energies of activation for the RLS steps ($\Delta G^{\ddagger}_{RLS}$) and activation free energy differences ($\Delta\Delta G$) relative to the most stable path for the *RR*- and *SS*-LA insertions at **1** depending on the assembly mode. Geometry optimization performed at B3LYP/D3BJ level with 6-311G(d,p) basis set on Al and SVP on C, H, N and O and single point calculations performed at BP86/D3BJ/PCM(Toluene) level with 6-311G(d,p) on all the atoms.

| Entry | Assembly mode | $\Delta G^{\ddagger}_{RLS}$(kcal/mol) | $\Delta\Delta G$ (kcal/mol) |
|---|---|---|---|
| 1 | *RR chain* + *RR* | 10.5 (TS2) | 0.0 |
| 2 | *SS chain* + *RR* | 11.2 (TS1) | 0.7 |
| 3 | *RR chain* + *SS* | 12.9 (TS1) | 2.4 |
| 4 | *SS chain* + *SS* | 13.0 (TS1) | 2.5 |
| 5 | *RR chain* + *RR* | 15.0 (TSα) | 4.5 |

**Table 1.19.** Free energies of activation for the RLS steps ($\Delta G^{\ddagger}_{RLS}$) and activation free energy differences ($\Delta\Delta G$) relative to the most stable path for the *RR*- and *SS*-LA insertions at **1** depending on the assembly mode. Geometry optimization performed at B3LYP/D3BJ level with 6-311G(d,p) basis set on Al and SVP on C, H, N and O and single point calculations performed at BP86/PCM(Toluene) level with 6-311G(d,p) on all the atoms.

| Entry | Assembly mode | $\Delta G^{\ddagger}_{RLS}$(kcal/mol) | $\Delta\Delta G$ (kcal/mol) |
|---|---|---|---|
| 1 | *SS chain* + *RR* | 25.3 (TS1) | 0.0 |
| 2 | *RR chain* + *RR* | 25.6 (TSα) | 0.3 |
| 3 | *RR chain* + *RR* | 25.8 (TS2) | 0.5 |
| 4 | *SS chain* + *SS* | 26.0 (TS1) | 0.7 |
| 5 | *RR chain* + *SS* | 29.0 (TS1) | 3.4 |

**Table 1.20.** Free energies of activation for the RLS steps ($\Delta G^{\ddagger}_{RLS}$) and activation free energy differences ($\Delta\Delta G$) relative to the most stable path for the *RR*- and *SS*-LA insertions at **1** depending on the assembly mode. Geometry optimization performed at B3LYP/D3BJ level with 6-311G(d,p) basis set on Al and SVP on C, H, N and O and single point calculations performed at M06-2X/PCM(Toluene) level with 6-311G(d,p) on all the atoms.

| Entry | Assembly mode | $\Delta G^{\ddagger}_{RLS}$(kcal/mol) | $\Delta\Delta G$ (kcal/mol) |
|---|---|---|---|
| 1 | *SS chain* + *RR* | 9.0 (TS1) | 0.0 |
| 2 | *RR chain* + *RR* | 10.6 (TSα) | 1.7 |
| 3 | *RR chain* + *RR* | 12.3 (TS2) | 2.1 |
| 4 | *SS chain* + *SS* | 13.1 (TS1) | 2.5 |
| 5 | *RR chain* + *SS* | 14.2 (TS1) | 3.6 |

Finally, to get confirmation on statements of paragraph 1.3.2 about the possible variability induced by the flexibility of the backbone linker and substitution in *ortho* on the salen moiety of system **1**, we performed additional calculations (Tables 1.21-1.23) for the first insertion at the two system reported in Figure 1.14, that are respectively salen-system with the less flexible $–CH_2-CH_2-$ backbone linker[39] (Figure 1.14-A) and system **1** with a dichloro sostitution in the ortho position of salen moiety (Figure 1.14-B, never tested in ROP).

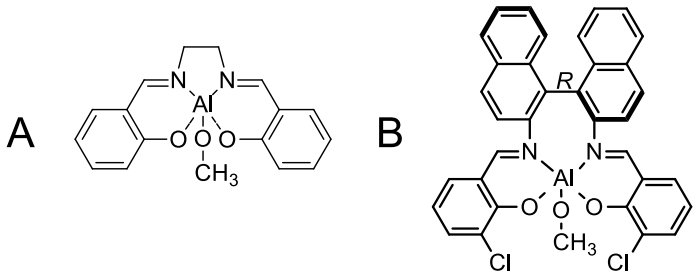


**Figure 1.14.** In **A** we report the salen-system with the less flexible $–CH_2-CH_2-$ backbone linker whose results are reported in Table 1.21, in **B** we report the system **1** with Cl in *ortho* position whose results are reported in Tables 1.22-1.23.

The results of Table 1.21 show clearly that *fac-fac* geometry for this system is extremely destabilized. We obtained very high free energy fot TS1 and TS2 for this geometry (>20 kcal/mol rather than *fac-mer* 1 and *fac-mer* 2) and even TSα is strongly influenced.

**Table 1.21.** TSs free energies ($\Delta G$, in kcal/mol) for all reaction paths computed for the first *RR*-LA *re* insertion in Al-$OCH_3$ bond for the salen system with $–CH_2$-$CH_2$- as backbone linker. In red the low-lying paths following the **M1**-**M3** mechanisms are reported.

| Monomer Enantioface | *RR re* | | | |
|---|---|---|---|---|
| Mechanism 1 (**M1**) | | **TS1** | | **TS2** |
| | A | 11.2 | | 8.8 |
| | B | 11.3 | | 12.5 |
| | C | 31.8 | | 26.8 |
| Mechanism 2 (**M2**) | | **TS1** | | **TS2** |
| | A | 11.2 | | 12.5 |
| | B | 11.3 | | 8.8 |
| Mechanism 3 (**M3**) | | **TS1** | **TSα** | **TS2** |
| | A | 11.2 | 31.9 | 26.8 |
| | B | 11.3 | 31.9 | 26.8 |
| | C | 31.8 | 31.9 | 8.8 |
| | D | 31.8 | 31.9 | 12.5 |

Our computational results during the first insertion (Tables 1.22-1.23) by adding Cl atoms in ortho position of system **1** (Figure 1.14-B) predict an inversion of preference for *RR*-LA versus *SS*-LA (the RLS is 1.0 kcal/mol lower for *SS*-LA). The TS2 following the **M2** for *RR*-LA is now destabilized due to the repulsive interaction between Cl and the exocyclic O of the LA (see Figure 1.12).

**Table 1.22.** TSs free energies (Δ*G*, in kcal/mol) for all reaction paths computed for the first *RR*-LA insertion in Al-$OCH_3$ bond for **1** with Cl in *ortho* position. In red the low-lying paths following the **M1**-**M3** mechanisms are reported.

| Monomer Enantioface | *RR re* | | | | Monomer Enantioface | *RR si* | | | |
|---|---|---|---|---|---|---|---|---|---|
| Mechanism 1 (**M1**) | | **TS1** | | **TS2** | Mechanism 1 (**M1**) | | **TS1** | | **TS2** |
| | A | 4.0 | | 8.3 | | A | 13.6 | | 7.7 |
| | B | 8.9 | | 8.1 | | B | 8.0 | | 5.9 |
| | C | 7.0 | | 7.9 | | C | 9.0 | | 3.0 |
| Mechanism 2 (**M2**) | | **TS1** | | **TS2** | Mechanism 2 (**M2**) | | **TS1** | | **TS2** |
| | A | 4.0 | | 8.1 | | A | 13.6 | | 5.9 |
| | B | 8.9 | | 8.3 | | B | 8.0 | | 7.7 |
| Mechanism 3 (**M3**) | | **TS1** | **TSα** | **TS2** | Mechanism 3 (**M3**) | | **TS1** | **TSα** | **TS2** |
| | A | 4.0 | 8.5 | 7.9 | | A | 13.6 | 6.5 | 3.0 |
| | B | 8.9 | 8.5 | 7.9 | | B | 8.0 | 6.5 | 3.0 |
| | C | 7.0 | 8.5 | 8.3 | | C | 9.0 | 6.5 | 7.7 |
| | D | 7.0 | 8.5 | 8.1 | | D | 9.0 | 6.5 | 5.9 |

**Table 1.23.** TSs free energies (Δ*G*, in kcal/mol) for all reaction paths computed for the first *SS*-LA insertion in Al-$OCH_3$ bond for **1** with Cl in *ortho* position. In red the low-lying paths following the **M1**-**M3** mechanisms are reported.

| Monomer Enantioface | *SS re* | | | | Monomer Enantioface | *SS si* | | | |
|---|---|---|---|---|---|---|---|---|---|
| Mechanism 1 (**M1**) | | **TS1** | | **TS2** | Mechanism 1 (**M1**) | | **TS1** | | **TS2** |
| | A | 8.5 | | 6.8 | | A | 6.0 | | 16.1 |
| | B | 12.0 | | 3.7 | | B | 4.6 | | 13.4 |
| | C | 6.9 | | 2.2 | | C | 6.7 | | 7.8 |
| Mechanism 2 (**M2**) | | **TS1** | | **TS2** | Mechanism 2 (**M2**) | | **TS1** | | **TS2** |
| | A | 8.5 | | 3.7 | | A | 6.0 | | 13.4 |
| | B | 12.0 | | 6.8 | | B | 4.6 | | 16.1 |
| Mechanism 3 (**M3**) | | **TS1** | **TSα** | **TS2** | Mechanism 3 (**M3**) | | **TS1** | **TSα** | **TS2** |
| | A | 8.5 | 5.6 | 2.2 | | A | 6.0 | 8.6 | 7.8 |
| | B | 12.0 | 5.6 | 2.2 | | B | 4.6 | 8.6 | 7.8 |
| | C | 6.9 | 5.6 | 6.8 | | C | 6.7 | 8.6 | 16.1 |
| | D | 6.9 | 5.6 | 3.7 | | D | 6.7 | 8.6 | 13.4 |

## 1.4 Conclusions

In summary, a model for the challenging goal[19] of metal catalyst stereoselection of *rac*-LA by the prototypical Spassky system[7] has been obtained by DFT calculations. The ROP chiral control to discriminate D- and L-LA in *rac*-mixture combines complexity (large number of mechanistic pathways) with novel mechanistic steps different from the classical ESM reported so far.[32,33] It is worth noting that the mechanisms we proposed can easily explain also the syndiotactic microstructure obtained by ROP of *meso*-LA promoted by **1**.[13] Furthermore, the procedure of computing the **M1**-**M3** mechanisms appears to be very general but their relative importance will depend on the metal[43-45] and the ligand framework.[46,47]

## References


1. Stürzel, M.; Mihan, S.; Mülhaupt, R. From Multisite Polymerization Catalysis to Sustainable Materials and All-Polyolefin Composites. *Chem. Rev.* **2016**, *116*, 1398-1433.
2. Resconi, L.; Cavallo, L.; Fait, A.; Piemontesi, F. Selectivity in Propene Polymerization with Metallocene Catalysts. *Chem. Rev.* **2000**, *100*, 1253-1346.
3. Busico, V.; Cipullo, R.; Pellecchia, R.; Ronca, S.; Roviello, G.; Talarico, G. Design of Stereoselective Ziegler–Natta Propene Polymerization Catalysts. *Proc. Natl. Acad. Sci.* **2006**, *103*, 15321-15326.
4. Zhang, X.; Fevre, M.; Jones, G. O.; Waymouth, R. M. Catalysis as an Enabling Science for Sustainable Polymers. *Chem. Rev.* **2018**, *118*, 839-885.
5. Drumright, R. E.; Gruber, P. R.; Henton, D. E. Polylactic Acid Technology. *Adv. Mater*. **2000**, *12*, 1841-1846.
6. Stanford, M. J.; Dove, A. P. Stereocontrolled Ring-Opening Polymerisation of Lactide. *Chem. Soc. Rev.* **2010**, *39*, 486-494.

7. Spassky, N.; Wisniewski, M.; Pluta, C.; Le Borgne, A. Highly Stereoelective Polymerization of *rac*-(D,L)-Lactide with a Chiral Schiff's Base/Aluminium Alkoxide Initiator. *Macromol. Chem. Phys.* **1996**, *197*, 2627-2637.
8. Thomas, C. M. Stereocontrolled Ring-Opening Polymerization of Cyclic Esters: Synthesis of New Polyester Microstructures. *Chem. Soc. Rev.* **2010**, *39*, 165-173.
9. Ovitt, T. M.; Coates, G. W. Stereochemistry of Lactide Polymerization with Chiral Catalysts: New Opportunities for Stereocontrol Using Polymer Exchange Mechanisms. *J. Am. Chem. Soc.* **2002**, *124*, 1316-1326.
10. Press, K.; Goldberg, I.; Kol, M. Mechanistic Insight into the Stereochemical Control of Lactide Polymerization by Salan–Aluminum Catalysts. *Angew. Chem., Int. Ed.* **2015**, *54*, 14858-14861.
11. (a) Ma, H.; Spaniol, T. P.; Okuda, J. Highly Heteroselective Ring-Opening Polymerization of *rac*-Lactide Initiated by Bis(phenolato)Scandium Complexes. *Angew. Chem., Int. Ed.* **2006**, *45*, 7818-7821; (b) Cheng, M.; Attygalle, A. B.; Lobkovsky, E. B.; Coates, G. W. Single-Site Catalysts for Ring-Opening Polymerization: Synthesis of Heterotactic Poly(lactic acid) from *rac*-Lactide. *J. Am. Chem. Soc.* **1999**, *121* (49), 11583-11584.
12. Buffet, J. C.; Okuda, J. Initiators for the Stereoselective Ring-Opening Polymerization of *meso*-Lactide. *Polym. Chem.* **2011,** *2*, 2758-2763.
13. Ovitt, T. M.; Coates, G. W. Stereoselective Ring-Opening Polymerization of *meso*-Lactide: Synthesis of Syndiotactic Poly(lactic acid). *J. Am. Chem. Soc.* **1999,** *121*, 4072-4073.
14. Hador, R.; Botta, A.; Venditto, V.; Lipstman, S.; Goldberg, I.; Kol, M. The Dual-Stereocontrol Mechanism: Heteroselective Polymerization of *rac*-Lactide and Syndioselective Polymerization of *meso*-Lactide by Chiral Aluminum Salan Catalysts. *Angew. Chem., Int. Ed.* **2019**, *58*, 14679-14685.

15. Zhong, Z.; Dijkstra, P. J.; Feijen, J. Controlled and Stereoselective Polymerization of Lactide: Kinetics, Selectivity, and Microstructures. *J. Am. Chem. Soc.* **2003**, *125*, 11291-11298.
16. Nomura, N.; Ishii, R.; Akakura, M.; Aoi, K. Stereoselective Ring-Opening Polymerization of Racemic Lactide Using Aluminum-Achiral Ligand Complexes: Exploration of a Chain-End Control Mechanism. *J. Am. Chem. Soc.* **2002**, *124*, 5938-5939.
17. The mechanism of the heterotactic enchainment operated by β-diketiminate Mg systems has been rationalized by Gibson et al. see Marshall, E. L.; Gibson, V. C.; Rzepa, H. S. A Computational Analysis of the Ring-Opening Polymerization of *rac*-Lactide Initiated by Single-Site β-Diketiminate Metal Complexes: Defining the Mechanistic Pathway and the Origin of Stereocontrol. *J. Am. Chem. Soc.* **2005**, *127*, 6048-6051.
18. De Rosa, C.; Di Girolamo, R.; Talarico, G. Expanding the Origin of Stereocontrol in Propene Polymerization Catalysis. *ACS Catal.* **2016**, *6*, 3767-3770.
19. Gaussian 09, Revision D.02, Frisch, M.J.; Trucks, G.W.; Schlegel, H.B.; Scuseria, G.E.; Robb, M.A.; Cheeseman, J.R.; Montgomery, Jr., J.A.; Vreven, T.; Kudin, K.N.; Burant, J.C.; Millam, J.M.; Iyengar, S.S.; Tomasi, J.; Barone, V.; Mennucci, B.; Cossi, M.; Scalmani, G.; Rega, N.; Petersson, G.A.; Nakatsuji, H.; Hada,M.; Ehara, M.; Toyota, K.; Fukuda, R.; Hasegawa, J.; Ishida, M.; Nakajima, T.; Honda, Y.; Kitao, O.; Nakai, H.; Klene, M.; Li, X.; Knox, J.E.; Hratchian, H.P.; Cross, J. B.; Bakken, V.; Adamo, C.; Jaramillo, J.; Gomperts, R.;Stratmann, R.E.; Yazyev, O.; Austin, A.J.; Cammi, R.; Pomelli, C.; Ochterski, J.W.; Ayala, P.Y.; Morokuma,K.; Voth, G.A.; Salvador, P.; Dannenberg, J.J.; Zakrzewski, V.G.; Dapprich, S.; Daniels, A.D.; Strain, M.C.;Farkas, O.; Malick, D.K.; Rabuck, A.D.; Raghavachari, K.; Foresman, J.B.; Ortiz, J.V.; Cui, Q.; Baboul, A.G.;Clifford, S.; Cioslowski, J.; Stefanov, B.B.; Liu, G.; Liashenko, A.; Piskorz, P.; Komaromi, I.; Martin, R.L.; Fox,D.J.;

Keith, T.; Al-Laham, M.A.; Peng, C.Y.; Nanayakkara, A.; Challacombe, M.; Gill, P.M.W.; Johnson, B.;Chen, W.; Wong, M.W.; Gonzalez, C.; and Pople, J.A. Gaussian, Inc., Wallingford CT, **2004**.

20. Lee, C.; Yang, W.; Parr, R. G. Development of the Colle-Salvetti Correlation-Energy Formula into a Functional of the Electron Density. *Phys. Rev. B* **1988**, *37*, 785-789.
21. (a) Becke, A. D. A New Mixing of Hartree–Fock and Local Density-Functional Theories. J. Chem. Phys. **1993**, *98*, 1372-1377; (b) Becke, A. D. Density-Functional Thermochemistry. III. The Role of Exact Exchange. *J. Chem. Phys*. **1993**, *98*, 5648-5652.
22. McLean, A. D.; Chandler, G. S. Contracted Gaussian Basis Sets for Molecular Calculations. I. Second Row Atoms, Z=11–18. *J. Chem. Phys*. **1980**, *72*, 5639-5648.
23. Schäfer, A.; Horn, H.; Ahlrichs, R. Fully Optimized Contracted Gaussian Basis Sets for Atoms Li to Kr. *J. Chem. Phys.* **1992**, *97*, 2571-2577.
24. Barone, V.; Cossi, M. Quantum Calculation of Molecular Energies and Energy Gradients in Solution by a Conductor Solvent Model. *J. Phys. Chem. A* **1998**, *102*, 1995-2001.
25. (a) Grimme, S.; Antony, J.; Ehrlich, S.; Krieg, H. A Consistent and Accurate Ab Initio Parametrization of Density Functional Dispersion Correction (DFT-D) for the 94 Elements H-Pu. *J. Chem. Phys*. **2010**, *132*, 154104; (b) Grimme, S. Accurate Description of van der Waals Complexes by Density Functional Theory Including Empirical Corrections. *J. Comput. Chem.* **2004**, *12*, 1463-1473.
26. Lin, T. T.; Liu, X. Y.; He, C. A DFT Study on Poly(lactic acid) Polymorphs. *Polymer* **2010**, *51*, 2779-2785.
27. Becke, A. D. Density-Functional Exchange-Energy Approximation with Correct Asymptotic Behavior. *Phys. Rev. A* **1988**, *38*, 3098-3100.

28. Perdew, J. P. Density-Functional Approximation for the Correlation Energy of the Inhomogeneous Electron Gas. *Phys. Rev. B* **1986**, *33*, 8822-8824.
29. Perdew, J. P. Erratum: Density-Functional Approximation for the Correlation Energy of the Inhomogeneous Electron Gas. *Phys. Rev. B* **1986**, *34*, 7406-7406.
30. Zhao, Y.; Truhlar, D. G. The M06 Suite of Density Functionals for Main Group Thermochemistry, Thermochemical Kinetics, Noncovalent Interactions, Excited States, and Transition Elements: Two New Functionals and Systematic Testing of Four M06-Class Functionals and 12 Other Functionals. *Theor. Chem. Acc.* **2008**, *120*, 215-241.
31. Guillaume, S. M.; Kirillov, E.; Sarazin, Y.; Carpentier, J.-F. Beyond Stereoselectivity, Switchable Catalysis: Some of the Last Frontier Challenges in Ring-Opening Polymerization of Cyclic Esters. *Chem. Eur. J.* **2015**, *21*, 7988-8003.
32. Tabthong, S.; Nanok, T.; Sumrit, P.; Kongsaeree, P.; Prabpai, S.; Chuawong, P.; Hormnirun, P. Bis(pyrrolidene) Schiff Base Aluminum Complexes as Isoselective-Biased Initiators for the Controlled Ring-Opening Polymerization of *rac*-Lactide: Experimental and Theoretical Studies. *Macromolecules* **2015**, *48*, 6846−6861.
33. Stasiw, D. E.; Luke, A. M.; Rosen, T.; League, A. B.; Mandal, M.; Neisen, B. D.; Cramer, C. J.; Kol, M.; Tolman, W. B. Mechanism of the Polymerization of *rac*-Lactide by Fast Zinc Alkoxide Catalysts. *Inorg. Chem.* **2017**, *56*, 14366-14372.
34. Vieira, I. d. S.; Whitelaw, E. L.; Jones, M. D.; Herres-Pawlis, S. Synergistic Empirical and Theoretical Study on the Stereoselective Mechanism for the Aluminum Salalen Complex Mediated Polymerization of *rac*-Lactide. *Chem. Eur. J.* **2013,** *19*, 4712-4716.
35. This is relevant for *fm* wrapping mode because the exchange of monomer and growing chain creates not equivalent ring-opening TS2 free energies.

36. We are aware of polymerization active site species showing a coordination environment around the metal different from the metal precursors. A prototypical case may be found in literature for salalen-Ti systems reported by Press, K.; Cohen, A.; Goldberg, I.; Venditto, V.; Mazzeo, M.; Kol, M. Salalen Titanium Complexes in the Highly Isospecific Polymerization of 1-Hexene and Propylene. *Angew. Chem., Int. Ed.* **2011**, *50*, 3529-3532 and revised by us in Talarico, G.; Budzelaar, P. H. M. Ligand Coordination Driven by Monomer and Polymer Chain: The Intriguing Case of Salalen–Ti Catalyst for Propene Polymerization. *Macromolecules* **2017**, *50*, 5332-5336. However, variation of active species framework depending of the relative chirality of the monomers (e.g. *RR* and *SS*) has never been reported to the best of our knowledge.
37. Here we define the *RR chain + SS* the assembly mode formed by the *SS*-monomer insertion at a previously ring-opened (*RR*)-LA unit. The preferred LA enantioface is *re*.
38. Spassky reported that *R*-(**1**) preferentially polymerizes *RR*-LA 20 times faster than *SS*-LA at 70°C in toluene at low monomer conversion (corresponding to a $\Delta\Delta G$ of 2.0 kcal/mol). The *SS*-LA polymerization starts at higher monomer conversion, as the reaction feed becomes poor in *RR*-LA. It is worth to note that no stereoselection is predicted computing the **M1** mechanism for the second LA insertion (compare the $\Delta G$ values of 16.4 kcal/mol for *RR*-LA with 16.2 for *SS*-LA in Figure 1.11).
39. Le Borgne, A.; Vincens, V.; Jouglard, M.; Spassky, N. Ring-opening Oligomerization Reactions Using Aluminium Complexes of Schiff's bBases as Initiators. *Makromol. Chem., Macromol. Symp*. **1993**, *73*, 37-46.
40. Hormnirun, P.; Marshall, E. L.; Gibson, V. C.; Pugh, R. I.; White, A. J. P. Study of Ligand Substituent Effects on the Rate and Stereoselectivity of Lactide Polymerization Using Aluminum Salen-type Initiators. *Proc. Natl. Acad. Sci. U.S.A.* **2006**, *103*, 15343-15348.

41. (a) Nomura, N.; Ishii, R.; Yamamoto, Y.; Kondo, T., Stereoselective Ring-Opening Polymerization of a Racemic Lactide by Using Achiral Salen– and Homosalen–Aluminum Complexes. *Chem. Eur. J.* **2007**, *13*, 4433-4451; (b) Chisholm, M. H.; Patmore, N. J.; Zhou, Z. Concerning the Relative Importance of Enantiomorphic Site *vs*. Chain End Control in the Stereoselective Polymerization of Lactides: Reactions of (*R,R*-salen)- and (*S,S*-salen)-Aluminium Alkoxides $LAlOCH_2R$ Complexes (R = $CH_3$ and *S*-CHMeCl). *Chem. Commun*. **2005**, 127-129.
42. A rough estimate of the energetic (opposite) effect exerted by CEM with respect to the ESM (around 1 kcal/mol) may be obtained by comparing the entries 4 and 5 in Table 1.8, where the $\Delta\Delta G$ is decreased from 1.8 to 0.8 kcal/mol.
43. (a) Chamberlain, B. M.; Cheng, M.; Moore, D. R.; Ovitt, T. M.; Lobkovsky, E. B.; Coates, G. W. Polymerization of Lactide with Zinc and Magnesium β-Diiminate Complexes: Stereocontrol and Mechanism. *J. Am. Chem. Soc.* **2001**, *123*, 3229-3238; (b) Fortun, S.; Daneshmand, P.; Schaper, F. Isotactic *rac*-Lactide Polymerization with Copper Complexes: The Influence of Complex Nuclearity. *Angew. Chem., Int. Ed.* **2015**, *54*, 13669-13672.
44. Bakewell, C.; White, A. J. P.; Long, N. J.; Williams, C. K. Metal-Size Influence in Iso-Selective Lactide Polymerization. *Angew. Chem., Int. Ed.* **2014**, *53*, 9226-9230.
45. (a) Douglas, A. F.; Patrick, B. O.; Mehrkhodavandi, P. A Highly Active Chiral Indium Catalyst for Living Lactide Polymerization. *Angew. Chem., Int. Ed.* **2008**, *47*, 2290-2293; (b) Chisholm, M. H.; Gallucci, J. C.; Quisenberry, K. T.; Zhou, Z. Complexities in the Ring-Opening Polymerization of Lactide by Chiral Salen Aluminum Initiators. *Inorg. Chem.* **2008**, *47*, 2613-2624.
46. Abbina, S.; Du, G. Zinc-Catalyzed Highly Isoselective Ring Opening Polymerization of *rac*-Lactide. *ACS Macro Lett.* **2014**, *3*, 689-692.
47. The high preference for a defined coordination mode around the metal may simplify the number of paths to be calculated for **M1**-**M3** mechanisms.

However, for salalen-Al system (see e.g. ref. 10,14) the **M1** mechanism shows four different paths due to the diasterotopic coordination sites for both *ff* and *fm* coordination modes. Consequently, also the number of paths of **M2** and **M3** are increased.

The work presented in this chapter has been published as: D'Alterio, M. C.; De Rosa, C.; Talarico G. Stereoselective Lactide Polymerization: the Challenge of Chiral Catalyst Recognition. *ACS Catal.* **2020**, *10,* 2221-2225, DOI10.1021/acscatal.9b05109.

# Chapter 2

# Alternating copolymerization of $CO_2$ and cyclohexene oxide by new pyridylamidozinc(II) catalysts


## Abstract

Five new Zn(II) complexes bearing pyridylamido ligands with different substituents at the pyridine and at the amido moieties were synthesized and evaluated as catalysts for the alternating copolymerization of carbon dioxide and cyclohexene oxide. Polymers with carbonate linkages ranging between 86-99 % and a slightly isotactic-enriched structure were selectively obtained under a variety of reaction conditions, including 1 atm of $CO_2$ pressure, without any co-catalyst. Some experimental and theoretical evidence suggest that different initiating species are involved in the catalytic cycle, including dimeric $[(L_x)Zn(\mu\text{-}OR)]_2$ and $[(L_x)Zn(\mu\text{-}O_2COR)]$ complexes similar to those involved in the classical β-diiminate Zn(II) catalysts.


## 2.1 Introduction

The production of synthetic polymers has increased exponentially in the last century, currently resulting in volumes higher than 300 million tons/year, a number which is expected to increase monotonically. Two major environmentally related issues have emerged concerning the continuous growth of polymers: (i) they are essentially manufactured from non-renewable resources, consuming about 8% of oil produced annually, and (ii) they are not biodegradable and only partially recycled, constituting more than 10% by weight (and a much larger fraction in volume) in the municipal solid waste and over 80% of waste that accumulates in shorelines and eventually in the ocean, where microplastic pollution can persist indefinitely and enter the trophic chain.[1] In this framework, the development of biodegradable polymeric materials

derived from renewable resources has gained increasing interest both in the industry and in the research community, also on the basis of political pressure from the main international funding agencies and, more recently, from legislation restricting the use of non-degradable plastics for packaging.[2] On the other hand, the global concern for the increase in $CO_2$ concentration in the atmosphere has boosted research efforts toward $CO_2$ utilization as an abundant and renewable carbon source for chemical production, although it is clear that even extensive incorporation of $CO_2$ feedstock in industrial chemical processes would have only a very limited impact on the *greenhouse effect* problem.[3] The Ring Opening CoPolymerization (ROCOP) of $CO_2$ with energy-rich substrates such as epoxides is a rare example of catalytic process with the potential to deliver large-scale quantities of products from carbon dioxide. The most commonly studied epoxides are cyclohexene oxide (CHO) and propylene oxide (PO). At present, the reaction is applied industrially in relatively large scale to produce low-molecular-weight, dihydroxy-terminated "polycarbonate diols" which are intermediates or additives in the polyurethane industry.[2] A variety of catalytic systems for the ROCOP of $CO_2$ and epoxides have been reported in the last two decades, most notable examples being [salen]MX type complexes (where M = Cr(III), Co(III), Al(III)), usually requiring a ionic compound or a Lewis base as a cocatalyst, possibly covalently bonded to the *salen* ligand (Scheme 2.1a).[4] A second class involves high-performing β-diiminate (BDI) Zn(II) catalysts (Scheme 2.1b) disclosed by Coates,[5,6] not requiring any cocatalyst owing to a bimetallic mechanism being in operation.[7] The latter discovery triggered the development of catalysts featuring bi-nucleating ligands: e. g., Rieger reported Zn(II) catalysts with ligands obtained by tethering two BDI moieties (Scheme 2.1c), resulting in the highest TOFs ever measured in the ROCOP of $CO_2$ and CHO,[8,9] homo- and hetero-binuclear complexes of Robson-type macrocyclic tetraamine-diphenolate ligands with Zn(II), Mg(II), Fe(III), and Co(III) (Scheme 2.1d) were also shown to be highly efficient ROCOP catalysts.[10-12]

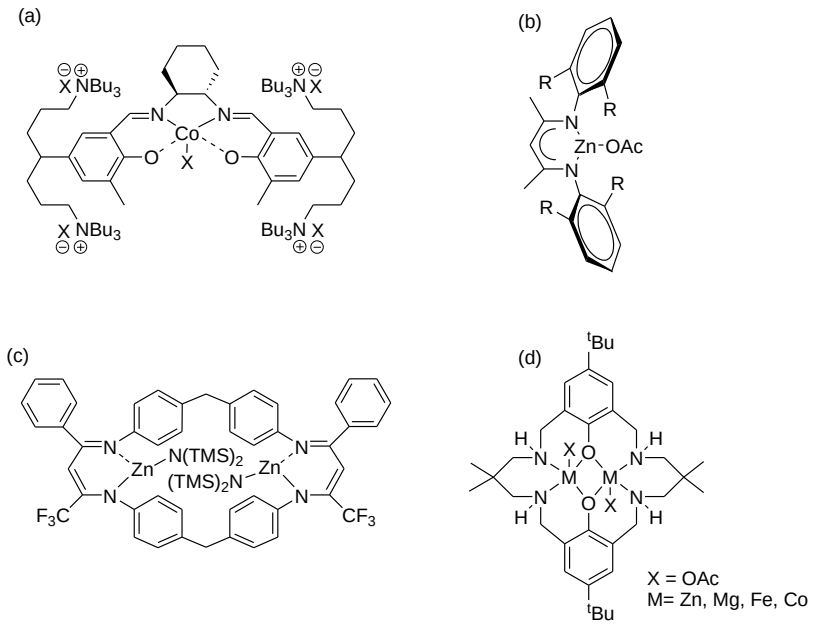


**Scheme 2.1.** Some representative catalysts for $CO_2$-epoxide copolymerization reported in the literature.

Considering the high efficiency of catalysts based on BDI ligands, it is somehow surprising that other classes of chelating monoanionic [N,N] ligands have not been investigated for the synthesis of potential ROCOP catalysts. In previous studies we reported properly designed pyridylamido[13] or pyridylimino[14] complexes of Groups 2, 3, 4, 10 and 13 metals as catalysts for the polymerization of olefins,[15-18] dienes,[19] and cyclic esters.[20] In this paper we report the synthesis of some new Zn(II) complexes bearing pyridylamido ligands (see Scheme 2.2) and their performance as catalysts for the ROCOP of CHO and carbon dioxide.

## 2.2 Experimental

### 2.2.1 General methods

All manipulations involving air and/or moisture-sensitive compounds were performed under an atmosphere of nitrogen in a Braun Labmaster glovebox or using Schlenk techniques. Glassware were dried in an oven at 120 °C overnight and exposed three times to vacuum–nitrogen cycles. Toluene was refluxed over metallic sodium, dichloromethane was refluxed over $CaH_2$, hexane and tetrahydrofurane were refluxed over sodium-benzophenone and distilled under nitrogen before use. Deuterated solvents were purchased from Aldrich and stored in the glovebox over 3 Å molecular sieves before use. Cyclohexene oxide were distilled under reduced pressure over calcium hydride and stored in a sealed flask in a glovebox. All other chemicals were commercially available and used as received unless otherwise stated.

### 2.2.2 Instruments and measurements

The NMR spectra were recorded either on a Bruker Advance 400 or on a Bruker 600 MHz Ascend 3 HD spectrometer. Chemical shifts (δ) are expressed as parts per million and coupling constants (J) in hertz. 1H NMR spectra were referenced using the residual solvent peak at δ 7.26 for $CDCl_3$, δ 5.32 for $CD_2Cl_2$ and δ 7.16 for $C_6D_6$. $^{13}C$ NMR spectra were referenced using the residual solvent peak at δ 77.22 for $CDCl_3$, δ 53.84 for $CD_2Cl_2$ and δ 128.06 for $C_6D_6$. $^{19}F$ NMR spectra were referenced to an external standard of neat $CFCl_3$.

MALDI mass spectra were acquired by using a Bruker solariX XR Fourier transform ion cyclotron resonance mass spectrometer (Bruker Daltonik GmbH, Bremen, Germany) equipped with a 7T refrigerated actively-shielded superconducting magnet (Bruker Biospin, Wissembourg, France). The samples were ionized in positive ion mode by using the ESI ion source (Bruker Daltonik GmbH,

Bremen, Germany). The mass range was set to m/z 150–3000. The mass spectra were calibrated externally by using a NaTFA solution in positive-ion mode. A linear calibration was applied. The molecular weights ($M_n$ and $M_w$) and the molecular mass distribution ($M_w/M_n$) of polymer samples were measured by gel permeation chromatography (GPC) at 30 °C, using THF as the solvent, an eluent flow rate of 1 mL min−1, and narrow polystyrene standards as the reference. The measurements were performed on a Waters 1525 binary system equipped with a Waters 2414 RI detector using four Styragel columns (range 1000–1 000 000 Å).
Elemental analyses were recorded on a Thermo Finningan Flash EA 1112 series C, H, N analyzer in the microanalytical laboratory of the Department.

### 2.2.3 Synthesis and characterization of ligands and complexes

The pyridylamino proligands $\mathbf{L_xH}$ (x=1-5) were synthesized following previously reported procedures.[19,21-23] Complexes **1-4** were cleanly obtained in yields ranging between 90-95%, following a typical synthetic approach, i. e. the reaction of $L_xH$ and $Zn[(NSiMe_3)_2]_2$ in 1:1 ratio (Scheme 2.2) in toluene, at 25 °C for complex **1** and at 80°C for complexes **2-4**. Complexes **1-4** were characterized by multinuclear NMR spectroscopy, confirming heteroleptic monomeric structures. Complex **5** was obtained following a similar procedure, but a lower reaction temperature (0 °C) was required, since a Schlenk-type equilibrium between the heteroleptic and the homoleptic bis(chelate) complex was observed by variable temperature NMR analysis (Figure 2.12) (elemental analyses for all the complexes are also reported).

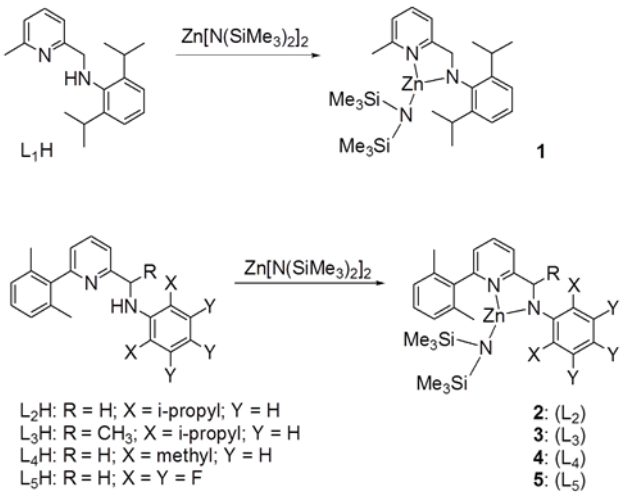


**Scheme 2.2.** Synthesis of the Zn(II) complexes **1-5**.

**6-(2,6-Dimethylphenyl)-2-pyridinecarboxaldehyde** (A), **1-[6-(2,6-dimethylphenyl)-2-pyridinyl]-ethanone** (B) and Ligand **$L_1H$** were prepared according to the literature[19,20] procedures. Ligands **$L_2H$-$L_5H$** were synthesized adapting literature procedures.[21-23]

**2,6-diisopropyl-N-((6-(2,6-dimethylphenyl)pyridin-2-yl)methyl)aniline ($L_2H$)**.

A solution of 6-(2,6-dimethylphenyl)pyridine-2-carbaldehyde (A) (2.11 g, 10.0 mmol), 2,6-diisopropylaniline (2.66 g, 15.0 mmol), and formic acid (4 drops) in MeOH (30 mL) was refluxed for 24 h and then the solution was cooled to room temperature. The solution was dried over $Na_2SO_4$; after filtration, the solvent was distilled off by rotary evaporation. The crude product was washed twice with cold methanol obtaining a yellow solid. Reduction of the imine function was carried out by using $NaBH_3CN$ in methanol, following a previously reported procedure,[3] yielding a white powder (yield: 2.90 g, 78%). $^1$H NMR ($CD_2Cl_2$, 300 MHz, 298 K): δ 1.19 (12H, d, J = 6.8 Hz, CH(C*H*$_3$)$_2$), 2.07 (6H, s, C*H*$_3$), 3.37 (2H, m, C*H*(CH$_3$)$_2$), 4.16 (1H, br, N*H*), 4.22 (2H, s, C*H*$_2$), 7.07-7.30 (8H, m, Ar*H*), 7.75 (1H, t, J = 7.7Hz, Ar*H*). $^{13}$C{$^1$H} NMR ($CD_2Cl_2$, 75 MHz, 298 K): δ 20.52, 24.20, 28.06,

52.53, 119.62, 121.50, 123.89, 127.56, 128.21, 136.30, 136.62, 141.33, 145.55, 159.63, 162.98.

**2,6-diisopropyl-N-(1-(6-(2,6-dimethylphenyl)pyridin-2-yl)ethyl)aniline ($L_3H$).** The imine ligand was obtained as above, reacting 1-[6-(2,6-dimethylphenyl)-2-pyridinyl]-ethanone (B) (3.13 g, 14.0 mmol) and 2,6-diisopropylaniline (3.72 g, 21.0 mmol). The subsequent reduction reaction with $NaBH_3CN$ gave amino ligand as white crystalline solid (yield: 4.04 g, 74%). $^1H$ NMR ($CD_2Cl_2$, 300 MHz, 298 K): δ 1.07 (6H, d, J = 6.8 Hz, CH(C*H*$_3$)$_2$), 1.17 (6H, d, J = 6.8 Hz, CH(C*H*$_3$)$_2$), 1.05 (3H, d, J = 6.7 Hz, C*H*$_3$), 2.07 (6H, br, C*H*$_3$), 3.14 (2H, sept, J = 6.8 Hz, C*H*(CH$_3$)$_2$), 3.94 (1H, br, N*H*), 4.23 (1H, q, J = 6.7 Hz, C*H*), 6.95 – 7.63 (8H, m, Ar*H*), 7.63 (1H, t, J = 7.7 Hz, Ar*H*). $^{13}C\{^1H\}$ NMR ($CD_2Cl_2$, 75 MHz, 298 K): δ 20.48, 21.93, 24.22, 28.04, 61.53, 119.81, 123.40, 123.77, 127.88, 128.10, 136.32, 136.92, 141.21, 142.55, 159.79, 163.48.

**2,6-dimethyl-N-((6-(2,6-dimethylphenyl)pyridin-2-yl)methyl)aniline ($L_4H$).** The imine ligand was obtained as above, reacting 6-(2,6-dimethylphenyl)pyridine-2-carbaldehyde (A) (1.60 g, 8.0 mmol) and 2,6-dimethylaniline (1.45 g, 12.0 mmol). The subsequent reduction reaction with $NaBH_3CN$ gave amino ligand as white powder (yield: 1.77 g, 70%). $^1H$ NMR ($CDCl_3$, 400 MHz, 298 K): δ 2.06 (6H, s, C*H*$_3$), 2.28 (6H, s, C*H*$_3$), 4.36 (2H, s, C*H*$_2$), 6.80 (1H, t, J = 8.0 Hz, Ar*H*), 6.81 (2H, m, Ar*H*), 6.97 (2H, m, Ar*H*), 7.10-7.20 (3H, m, Ar*H*), 7.68 (1H, t, J = 8.0 Hz, Ar*H*). $^{13}C\{^1H\}$ NMR ($CDCl_3$, 100 MHz, 298 K): δ 18.86, 20.53, 53.95, 122.19, 122.30,129.01, 129.50, 136.54, 136.89, 146.32, 149.56, 156.78, 163.48.

**2,3,4,5,6-pentafluoro-N-((6-(2,6-dimethylphenyl)pyridin-2-yl)methyl)aniline ($L_5H$).** To a stirred solution of 2,3,4,5,6-pentafluoroaniline (2.20 g; 12 mmol) and 6-(2,6-dimethylphenyl)pyridine-2-carbaldehyde (A) (1.60 g, 8 mmol) in anhydrous toluene (30 mL) under nitrogen was added *p*-toluenesulfonic acid (7.2 mg). The resulting mixture was stirred at reflux temperature for 18 h. Removal of solvent under *vacuum* gave a pale yellow powder. The subsequent reduction reaction with

$NaBH_3CN$ gave amino ligand as white crystalline solid (yield :1.80g, 60%). $^1$H-NMR ($CDCl_3$, 400 MHz, 298 K): δ 2.02 (6H, s, C*H*$_3$), 4.63 (2H, d, J = 4.1 Hz, C*H*$_2$), 5.00 (1H, br, N*H*) 7.11-7.23 (5H, m, Ar*H*), 7.6874 (1H, t, J = 8.0 Hz, Ar*H*). $^1$H {$^{19}$F} NMR (376.65 MHz, $CDCl_3$, 298 K) δ -171.95, -165.01, -159.41. $^{13}$C{$^1$H} NMR ($CDCl_3$, 100 MHz, 298 K): δ.20.27, 51.00, 119.95, 123.65, 127.85, 128.18, 135.90, 137.16, 140.19, 157.12, 159.90.

**($L_1$)ZnN($SiMe_3$)$_2$ (1).** In an Mbraun glovebox, a solution of the proligand $L_1H$ (0.600 g, 2.12 mmol) in toluene (2.5 mL) was added dropwise into a solution of $Zn[N(SiMe_3)_2]_2$ (0.820 g, 2.12 mmol) in toluene (2.5 mL) The resulting mixture was stirred at room temperature for 2 hours. The solvent was removed *in vacuo* and the solid residue was washed using dry hexane to obtain a white powder (yield: 0.980 g, 91%). $^1$H NMR ($C_6D_6$, 600 MHz, 298 K) (Figure 2.1) : δ 0.26 (18H, s, Si*Me*$_3$), 1.35 (6H, d, J = 7.0 Hz, CH(C*H*$_3$)$_2$), 1.41 (6H, d, J = 7.0 Hz, CH(C*H*$_3$)$_2$), 2.59 (3H, s, C*H*$_3$), 3.80 (2H, sept, J = 7.0 Hz, C*H*(CH$_3$)$_2$), 4.54 (2H, s, C*H*$_2$), 6.33 (1H, d, J = 7.8 Hz, *H*$_{pyridine}$) 6.36 (1H, d, J = 7.8 Hz, *H*$_{pyridine}$), 6.77 (1H, t, J = 7.8 Hz, *H*$_{pyridine}$), 7.20 – 7.27 (3H, m, Ar*H*). $^{13}$C{$^1$H} NMR ($C_6D_6$, 150 MHz, 298 K) (Figure 2.2): δ 5.93, 24.14, 26.16, 26.28, 28.29, 61.27, 120.43, 122.82, 124.35, 124.59, 138.39, 147.46, 150.39, 157.41, 163.85. Elemental Analysis: Calcd for $C_{25}H_{43}N_3Si_2Zn$: C 59.20%; H 8.55%; N 8.28%. Found: C 59.87%; H 8.72%; N 7.98%.

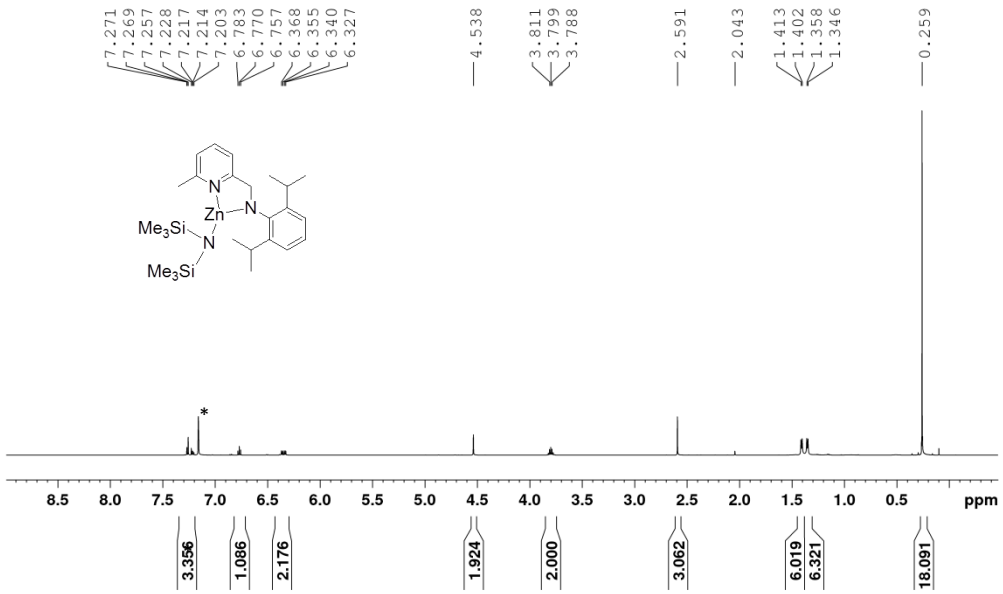


**Figure 2.1.** $^{1}$H-NMR ($C_6D_6$, 600 MHz, 298 K) of complex **1** (* stands for residual solvent resonance).

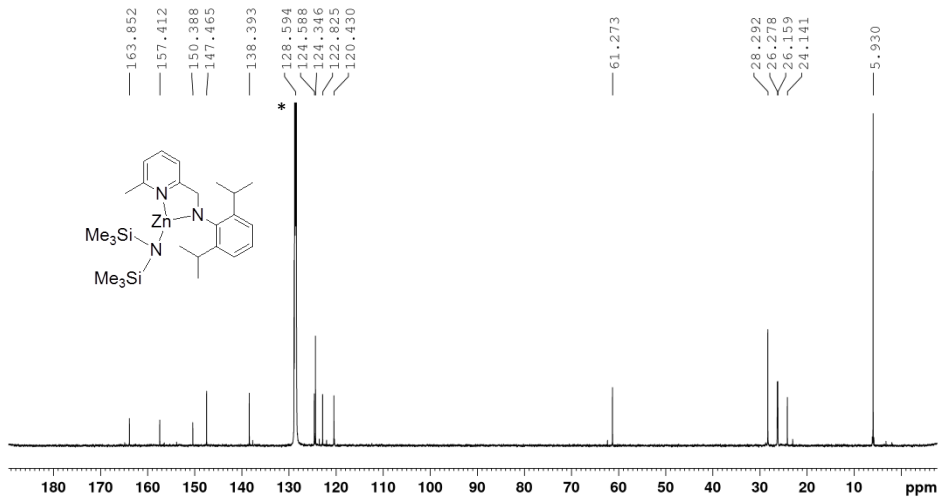


**Figure 2.2** $^{13}$C-NMR ($C_6D_6$, 150 MHz, 298 K) of complex **1** (* stands for residual solvent resonance).

**($L_2$)ZnN($SiMe_3$)$_2$ (2).** In an Mbraun glovebox, a solution of the proligand $L_2H$ (0.300 g, 0.81 mmol) in toluene (2.5 mL) was added into a solution of $Zn[N(SiMe_3)_2]_2$ (0.311 g, 0.81 mmol) in toluene ( 2.5 mL). The resulting mixture was stirred at 80°C for 24 hours. The solvent was removed *in vacuo* and the solid residue was washed using dry hexane to obtain a white powder (yield:0.455 g, 94%).$^1$H NMR (Figure 2.3) ($C_6D_6$, 600 MHz, 298 K): δ 0.07 (18H, s, Si*Me*$_3$), 1.36 (6H, d, J = 7.2 Hz, CH(C*H*$_3$)$_2$), 1.44 (6H, d, J = 7.2 Hz, CH(C*H*$_3$)$_2$), 2.01 (6H, s, C*H*$_3$), 3.80 (2H, sept, J = 7.2 Hz, C*H*(CH$_3$)$_2$), 4.68 (2H, s, C*H*$_2$), 6.42 (1H, d, J = 7.8 Hz, *H*$_{pyridine}$) 6.45 (1H, d, J = 7.8 Hz, *H*$_{pyridine}$), 6.84 (1H, t, J = 7.8 Hz, *H*$_{pyridine}$), 7.00 (2H, d, J = 7.8 Hz, Ar*H*), 7.14 (1H, t, J = 7.8 Hz, Ar*H*), 7.21 – 7.28 (3H, m, Ar*H*). $^{13}$C{$^1$H} NMR ($C_6D_6$, 150 MHz, 298 K) (Figure 2.4): δ 5.37, 21.06, 25.20, 26.01, 27.97, 60.98, 121.14, 123.77, 123.87, 124.29, 128.88, 129.58, 135.84, 137.68, 138.47, 146.83, 150.24, 158.12, 164.28. Elemental Analysis: Calcd for $C_{32}H_{49}N_3Si_2Zn$: C 64.35%; H 8.27%; N 7.03%. Found: C 64.41%; H 8.03%; N 7.46%.

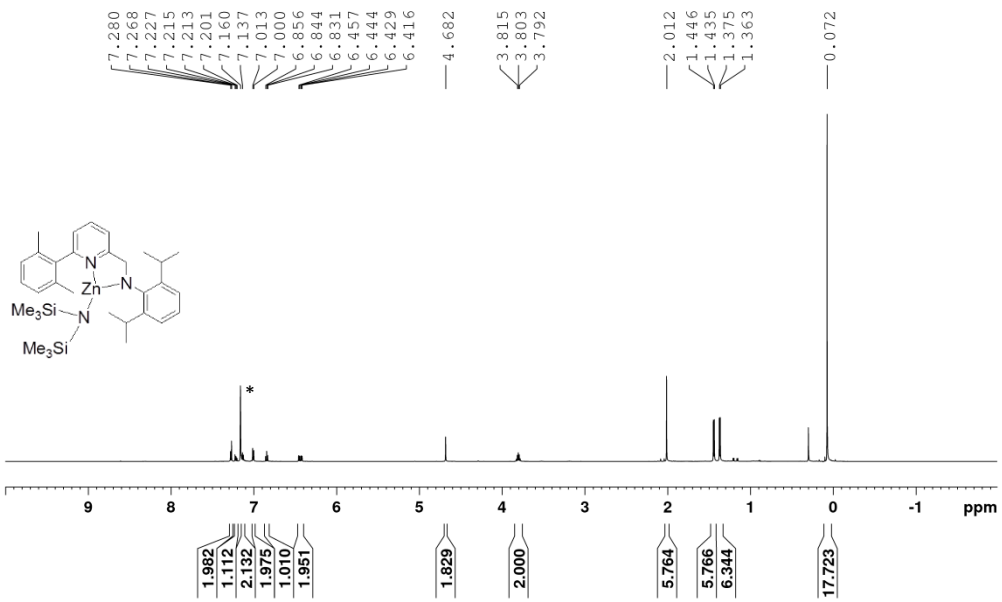


**Figure 2.3.** $^1$H-NMR ($C_6D_6$, 600 MHz, 298 K) of complex **2** (* stands for residual solvent resonance).

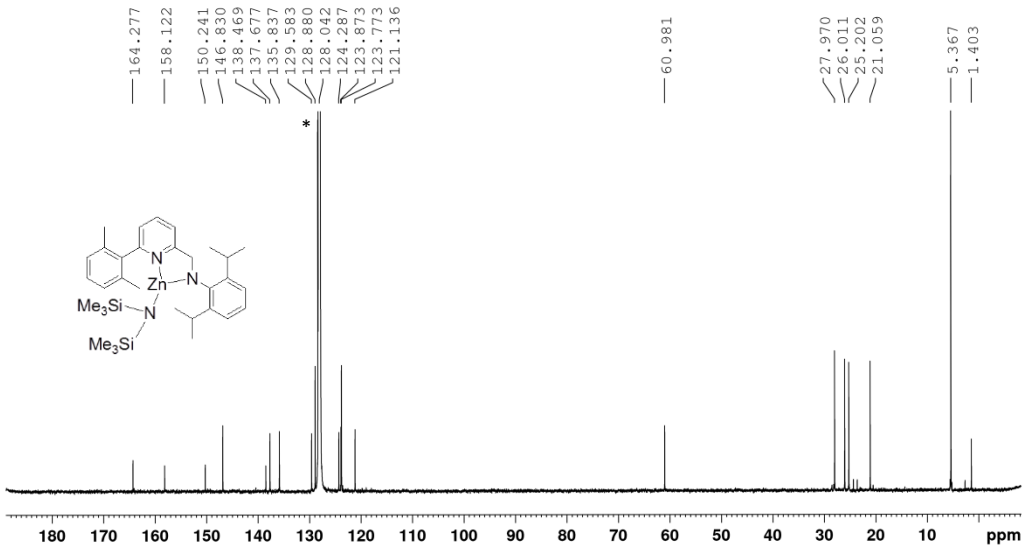


**Figure 2.4.** $^{13}$C-NMR ($C_6D_6$, 150 MHz, 298 K) of complex **2** (* stands for residual solvent resonance).

**($L_3$)ZnN($SiMe_3$)$_2$ (3).** The reaction was performed as above, reacting proligand $L_3H$ (0.500 g, 1.30 mmol) and Zn[N($SiMe_3$)$_2$]$_2$ (0.500 g, 1.30 mmol) in 5 mL of toluene and obtaining a yellow powder (yield: 0.750 g, 95%).$^1$H NMR ($CD_2Cl_2$, 600 MHz, 298 K) (Figure 2.5): δ -0.27 (18H, s, Si*Me*$_3$), 1.00 (3H, d, J = 6.6 Hz, CH(C*H*$_3$)$_2$), 1.21 (6H, d, J = 6.6 Hz, CH(C*H*$_3$)$_2$), 1.22 (3H, d, J = 6.6 Hz, CH(C*H*$_3$)$_2$), 1.33 (3H, d, J = 6.8 Hz, C*H*$_3$), 2.06 (3H, s, C*H*$_3$), 2.17 (3H, s, C*H*$_3$), 3.00 (1H, sept, J = 6.6 Hz, C*H*(CH$_3$)$_2$), 4.02 (1H, sept, J = 6.6 Hz, C*H*(CH$_3$)$_2$), 4.52 (1H, q, J = 6.8 Hz, C*H*), 6.97 (1H, t, J = 7.8 Hz, Ar*H*), 7.02 (1H, d, J = 7.8 Hz, Ar*H*), 7.07 (1H, d, J = 7.8 Hz, Ar*H*), 7.13 (1H, d, J = 7.2 Hz, Ar*H*), 7.18 (1H, d, J = 7.2 Hz, Ar*H*), 7.22 (1H, d, J = 7.8 Hz, *H*$_{pyridine}$), 7.28 (1H, t, J = 7.2 Hz, Ar*H*), 7.45 (1H, d, J = 7.8 Hz, *H*$_{pyridine}$), 7.93 (1H, t, J = 7.8 Hz, *H*$_{pyridine}$). $^{13}$C{$^1$H} NMR ($CD_2Cl_2$, 150 MHz, 298 K) (Figure 2.6): δ 5.34, 21.40, 24.88, 25.66, 26.86, 27.38, 27.47, 28.22, 65.26, 123.46, 124.38, 125.36, 129.16, 129.21, 129.69, 136.10, 136.65, 139.20, 139.30, 147.52, 150.60, 158.94, 169.31. Elemental Analysis: Calcd for $C_{33}H_{51}N_3Si_2Zn$: C 64.83%; H 8.41%; N 6.87%. Found: C 65.32%; H 8.24%; N 7.01%.

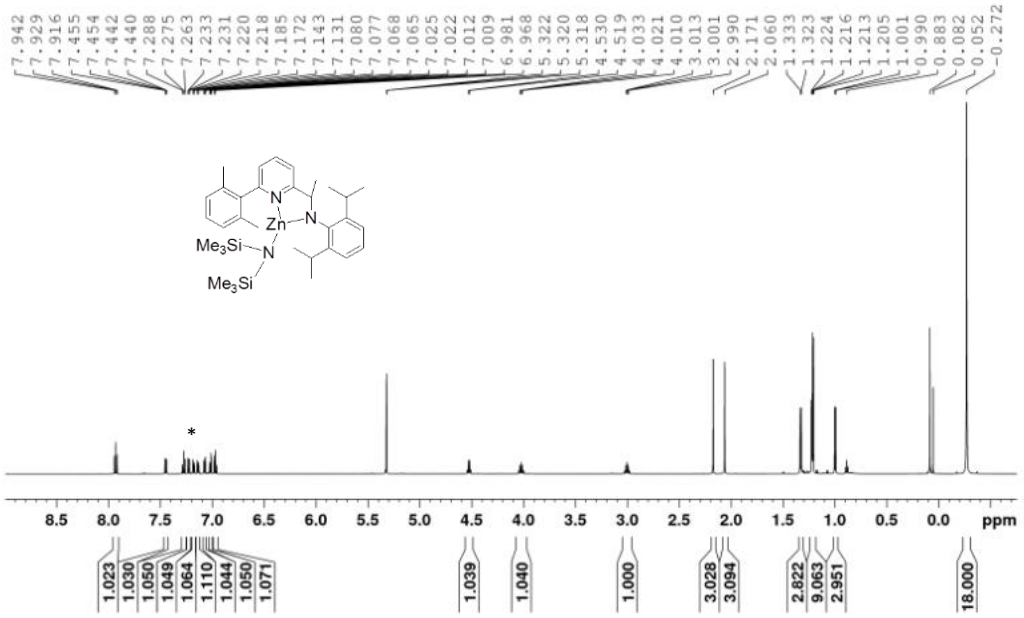


**Figure 2.5.** $^{1}$H-NMR ($CD_2Cl_2$, 600 MHz, 298 K) of complex **3** (* stands for residual solvent resonance).

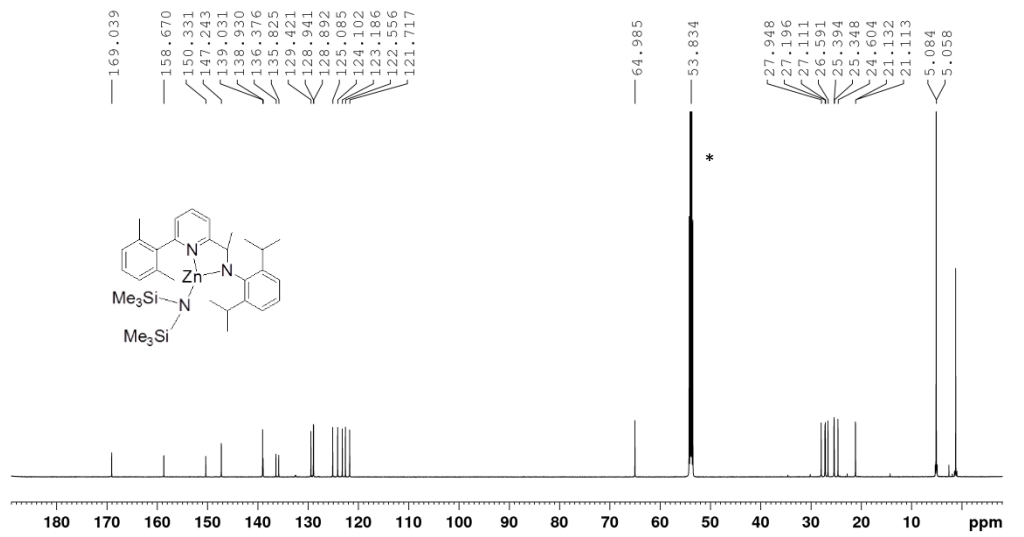


**Figure 2.6.** $^{13}$C-NMR ($CD_2Cl_2$, 150 MHz, 298 K) of complex **3** (* stands for residual solvent resonance).

**($L_4$)ZnN($SiMe_3$)$_2$ (4).** The reaction was performed as above, reacting proligand $L_4H$ (0.300 g, 0.95 mmol) and $Zn[N(SiMe_3)_2]_2$ (0.366 g, 0.95 mmol) in 5 mL of toluene and obtaining a deep yellow powder (yield: 0.495, 96%). $^1$H NMR ($C_6D_6$, 600 MHz, 298 K) (Figure 2.7) : δ 0.06 (18H, s, Si*Me*$_3$), 1.99 (6H, s, C*H*$_3$), 2.51 (6H, s, C*H*$_3$), 4.53 (2H, s, C*H*$_2$), 6.44 (1H, d, J = 7.2 Hz, Ar*H*), 6.47 (1H, d, J = 7.2 Hz, Ar*H*), 6.87 (1H, t, J = 7.2 Hz, Ar*H*), 7.99 – 7.03 (3H, m, Ar*H*), 7.14 (1H, t, J = 7.2 Hz, Ar*H*), 7.24 (2H, d, J = 7.2 Hz, Ar*H*). $^{13}$C{$^1$H} NMR ($C_6D_6$, 150 MHz, 298 K) (Figure 2.8) : δ 5.25, 19.56, 21.04, 56.91, 121.39, 122.47, 124.06, 128.80, 128.88, 129.67, 135.41, 135.87, 137.56, 138.41, 152.81, 158.06, 164.90. Elemental Analysis: Calcd for $C_{28}H_{41}N_3Si_2Zn$: C 62.14%; H 7.64%; N 7.76%. Found: C 63.33%; H 7.02%; N 7.85%.

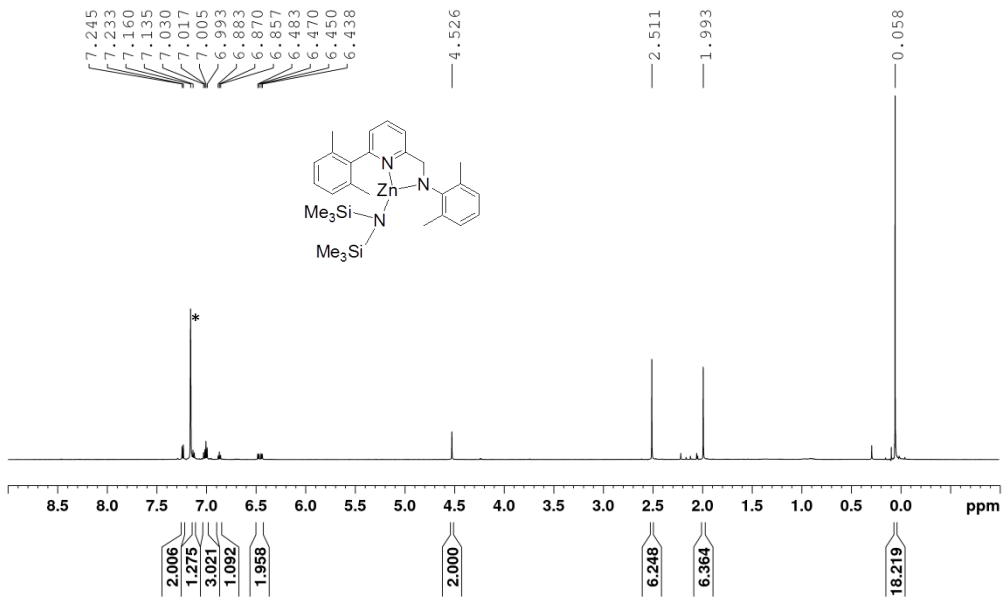


**Figure 2.7.** $^1$H-NMR ($C_6D_6$, 600 MHz, 298 K) of complex **4** (* stands for residual solvent resonance).

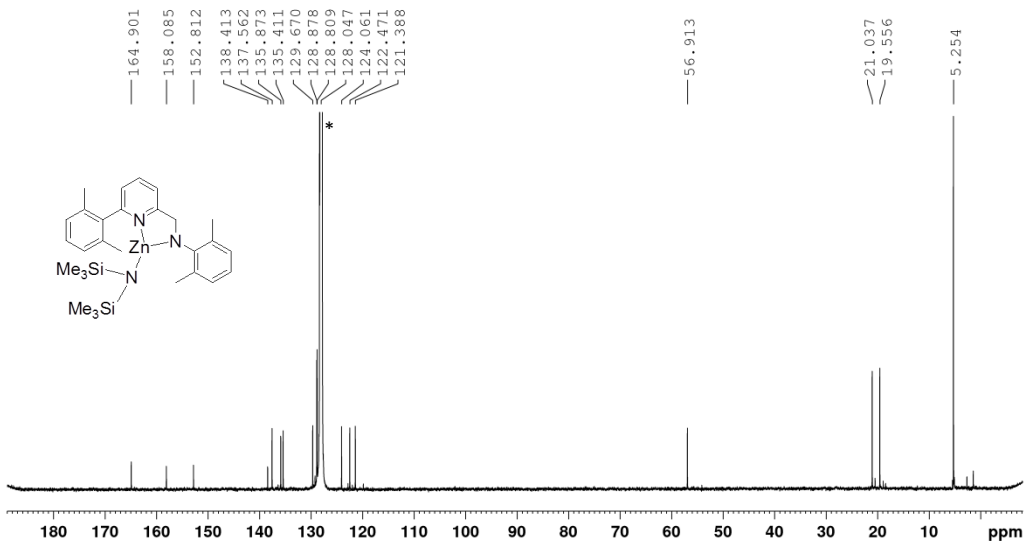


**Figure 2.8.** $^{13}$C-NMR ($C_6D_6$, 150 MHz, 298 K) of complex **4** (* stands for residual solvent resonance).

**($L_5$)ZnN($SiMe_3$)$_2$ (5).** A solution of the proligand $L_5H$ (0.200 g, 0.52 mmol) in toluene (5 mL) was added dropwise into a solution of $Zn[N(SiMe_3)_2]_2$ (0.204 g, 0.52 mmol) in toluene (5 mL) at 0°C for 10 minutes. The resulting mixture was stirred at 0°C for 30 minutes, then the solvent was removed *in vacuo* for several hours obtaining an orange powder (yield: 0.280, 90%). $^1$H NMR ($C_6D_6$, 300 MHz, 298 K) (Figure 2.9): δ 0.12 (18H, s, Si*Me*$_3$), 1.87 (6H, s, C*H*$_3$), 4.56 (2H, s, C*H*$_2$), 6.29 (2H, d, J = 7.0 Hz, *H*$_{pyridine}$), 6.86 (1H, t, J = 7.0 Hz, *H*$_{pyridine}$), 6.95 (2H, d, J = 7.8 Hz, Ar*H*), 7.15 (1H, t, J = 7.8 Hz, Ar*H*). $^{13}$C{$^1$H} NMR ($C_6D_6$, 150 MHz, 298 K) (Figure 2.10): δ 3.16, 17.47, 17.76, 51.07, 51.74, 119.35, 121.42, 125.10, 127.32, 130.34, 131.86, 135.77, 136.10, 136.31, 156.13, 161.03. Elemental Analysis: Calcd for $C_{26}H_{32}F_5N_3Si_2Zn$: C 51.78%; H 5.35%; N 6.97%. Found: C 51.33%; H 5.02%; N 7.05%. MS (MALDI-ToF) m/z (ion): 818.150 for $C_{40}H_{28}F_{10}N_4Zn$ [$(L_5)_2Zn^+$] (Figure 2.11).

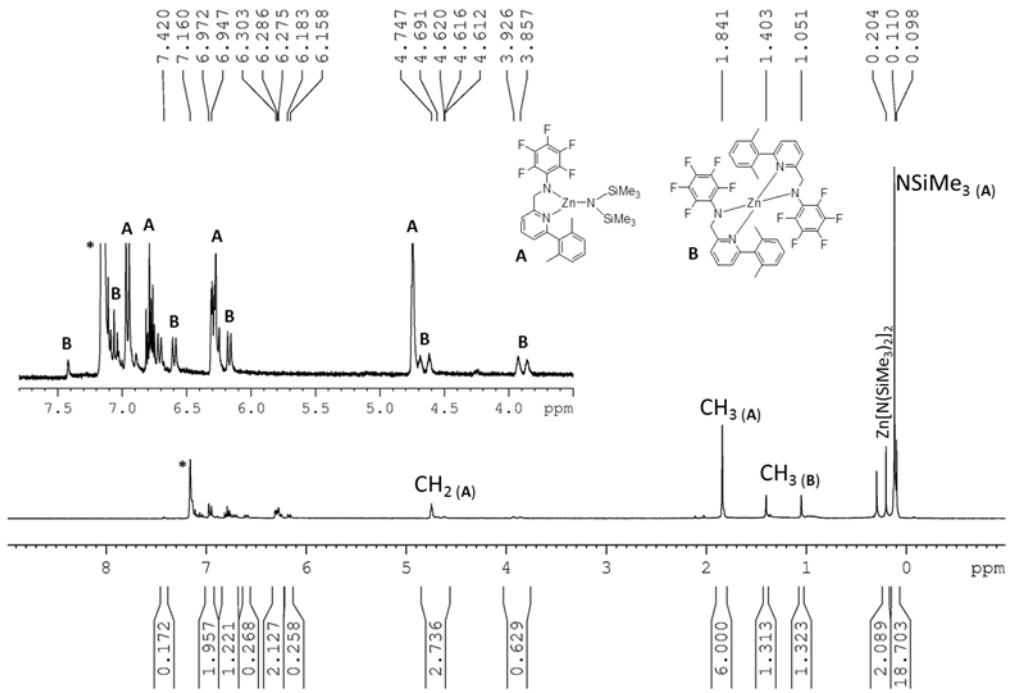


**Figure 2.9.** $^{1}$H-NMR ($C_6D_6$, 600 MHz, 298 K) of complex **5**: the heteroleptic (A) and the homoleptic bis(chelate) (B) species (* stands for residual solvent resonance).

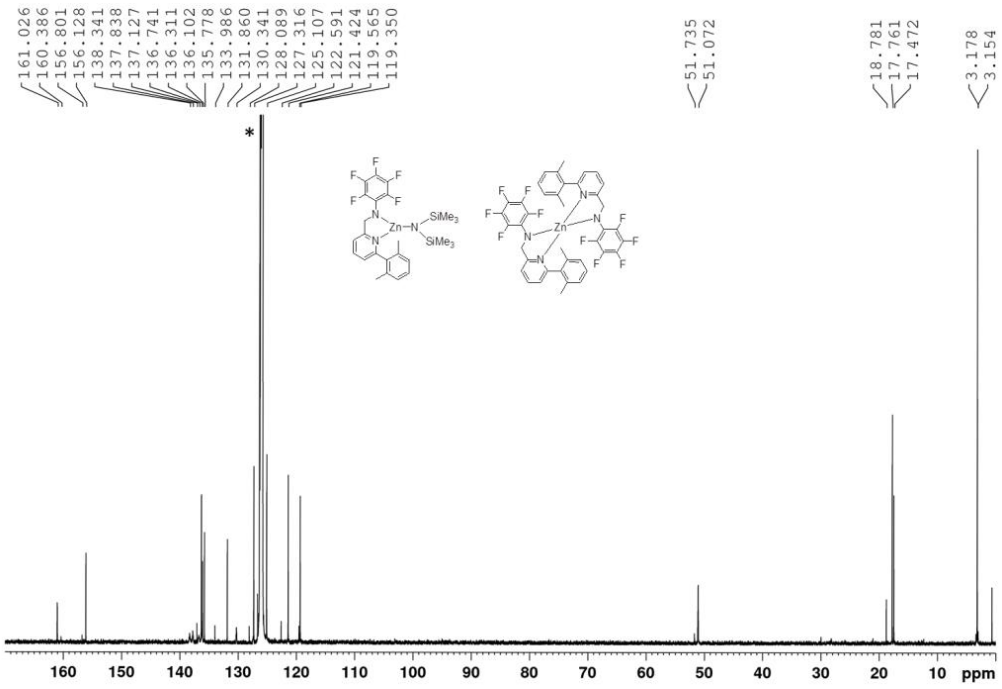


**Figure 2.10.** $^{13}$C-NMR ($C_6D_6$, 150 MHz, 298 K) of complex **5**: the heteroleptic (A) and the homoleptic bis(chelate) (B) species (* stands for residual solvent resonance).

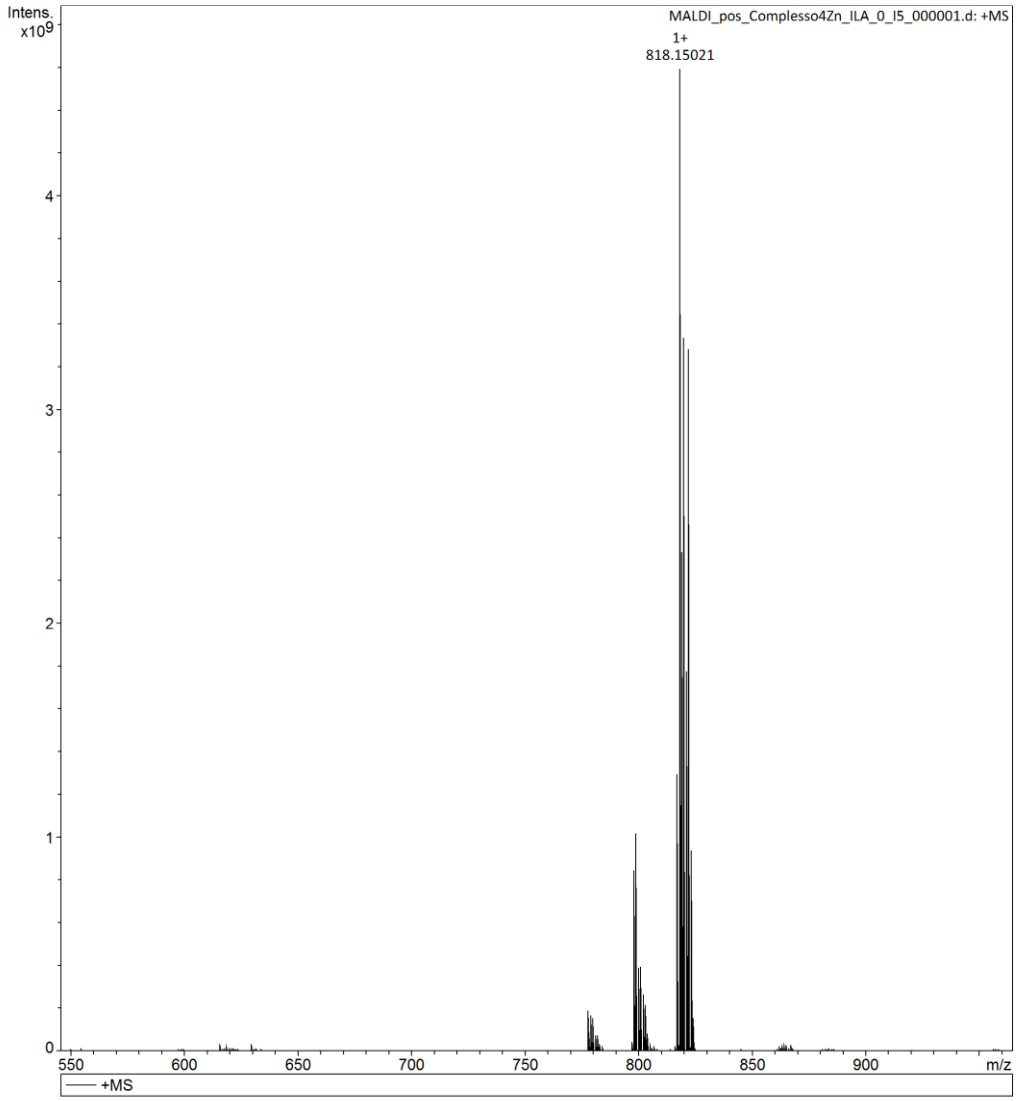


**Figure 2.11.** MALDI-ToF mass spectrum of **5**, peak at 818.15 m/z belongs to the molecular ion of $C_{40}H_{28}F_{10}N_4Zn$ $[(L_5)_2Zn^+]$..

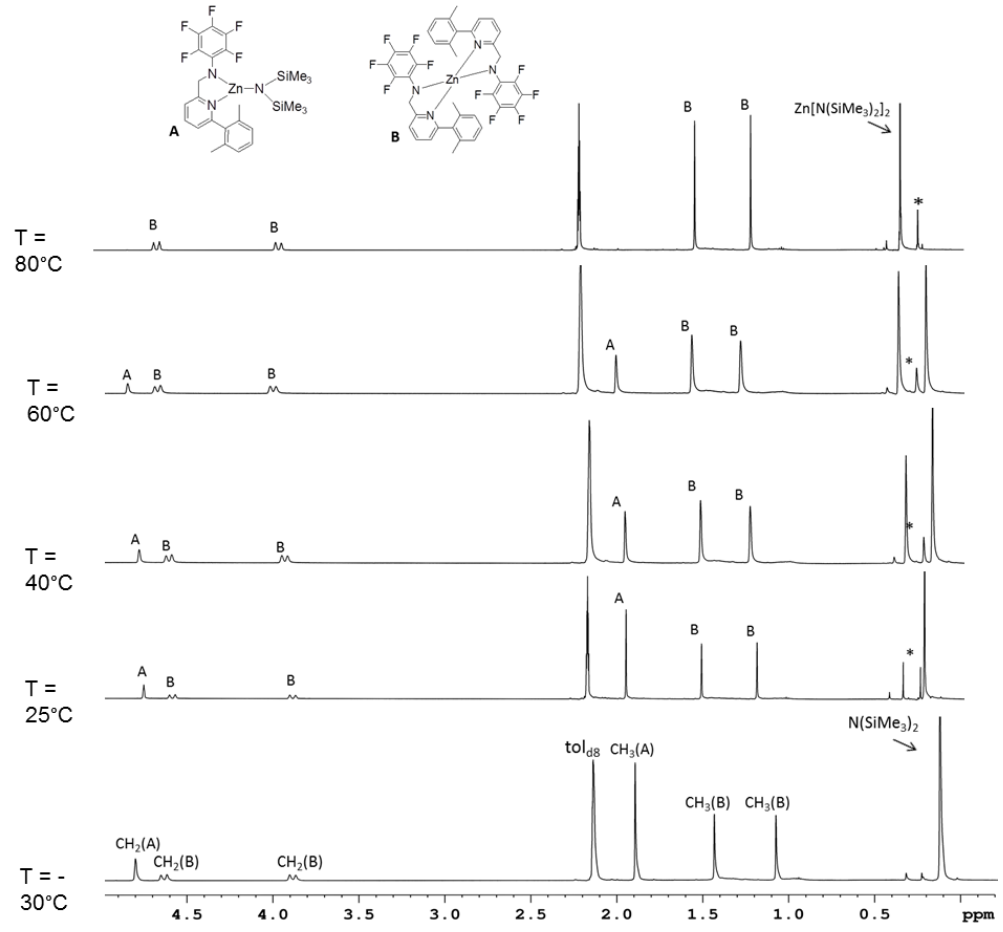


**Figure 2.12.** An aliphatic section of $^{1}$H-NMR ($C_7D_8$, 298 K, 600 MHz) spectra of complex **5** evolving towards the homoleptic species versus temperature (* stands for silicon grease resonance).

## 2.2.4 General procedure for cyclohexene oxide/carbon dioxide copolymerizations

In a glove-box, the zinc complex (50 μmol) was dissolved 4 mL of CHO (40 mmol) and transfered into the autoclave. The autoclave was pressurized at the desired pressure of $CO_2$, whilst the reaction mixture was stirred for 10 minutes at room

temperature, in order to facilitate $CO_2$ dissolution. The mixture was thermostated at the required temperature under stirring. After the prescribed time, the autoclave was vented after cooling in an ice bath and opened in air. A small sample of the crude material was removed for NMR analysis and then the reaction was quenched with 5 mL of methanol. The resulting mixture was dissolved in $CH_2Cl_2$, and the polymer was purified upon precipitation in cold hexane, filtered and dried under vacuum to a constant weight. Reactions using 1 bar of $CO_2$ were performed in a Schlenk flask connected to a manifold line (vacuum/$CO_2$) and heated using an oil bath. In experiments monitored by $^1$H NMR spectroscopy at 1 bar of $CO_2$, in a glove-box, a defined toluene solution of the zinc complex **1** (1 mL) and 3 mL of CHO were transfered into an oven-dried Schlenk flask. The reaction mixture was degassed and subsequently saturated with $CO_2$. A magnetic stirrer bar was used for mixing. The aliquots were removed at regular time intervals, by opening the Schlenk flask under a countercurrent of $CO_2$ in order to avoid increased contamination by air or water. The reaction order in catalyst concentration was studied over the range [**4**] = 6, 12, and 18 mM, with $[CHO]_0$ of 7.5 M in toluene (1mL), at 80 C and 1 bar $CO_2$.

### 2.2.5 MALDI-ToF MS spectra

Mass spectra of selected polymer samples were acquired using a Bruker solariX XR Fourier transform ion cyclotron resonance mass spectrometer equipped with a 7 T refrigerated actively-shielded superconducting magnet. The samples were ionized in positive ion mode using the MALDI ion source. The mass range was set to *m/z* 150 – 9000. The laser power was 15% and 15 laser shots were used for each scan. The mass spectra were calibrated externally using a mix of peptide clusters in MALDI ionization positive ion mode. A linear calibration was applied. The samples were dissolved in THF (1 mg/mL). Trans-2-[3-(4-tert-Butylphenyl)-2-methyl 2-propenylidene]malononitrile (DCTB) was used as the matrix with potassium trifluoroacetate (KTFA) as cationizing agent. The matrix was dissolved in THF at a

concentration of 10 mg/mL and ~ 2 mg of KTFA was added to the solution. The matrix and polymer solutions were mixed together in a 4:1 ratio and this mixture was spotted on the MALDI plate and left to dry. After evaporation of the solvent, the MALDI target was introduced into the spectrometer.

### 2.2.6 Diffusion NMR experiments

Complex **1** (15 mg, 30 μmol) and tetrakis(trimethylsilyl)silane (TMSS, 9 mg, 30 μmol) were dissolved in 0.7 mL of toluene-$d_8$ in an NMR J-Young tube. A DOSY experiment was performed on a Bruker Avance-600 spectrometer equipped with 5 mm PABBO BB|19F-1H\D Z-GRD Z114607/0109. The standard Bruker pulse program, ledbpgp2s, employing a double stimulated echo sequence and LED, bipolar gradient pulses for diffusion, and two spoil gradients were utilized. Diffusion times were 100 ms, eddy current delay was 5 ms, gradient recovery delays was 0.8 ms and gradient pulse was 1400 ms. Individual rows of the quasi-2D diffusion databases were phased and baseline corrected. Subsequently, **1** (11 mg , 20 μmol) was dissolved in toluene-$d_8$ (0.7 mL), placed into a J-Young NMR tube and thermostated at -20°C. $CO_2$ was bubbled into the cold solution and the tube was placed in an oil bath at 80°C for 5 minutes. Then the solution was analyzed *via* $^1$H-NMR. $^1$H NMR ($C_7D_8$, 600 MHz, 298 K): δ -0.103 (9H, s, O=C=NSi*Me*$_3$), 0.21 (9H, s, OSi*Me*$_3$),0.91(6H, d, J = 7.2 Hz, CH(C*H*$_3$)$_2$), 1.15 (6H, d, J = 7.2 Hz, CH(C*H*$_3$)$_2$), 2.23 (3H, s, C*H*$_3$), 3.07 (2H, sept, J = 7.2 Hz, C*H*(CH$_3$)$_2$), 4.86 (2H, s, C*H*$_2$),6.52 (1H, br, Ar*H*), 6.95 – 7.07 (4H, m, Ar*H*), 7.51 (1H, br, Ar*H*). Then, TMSS (6 mg, 20 μmol) was added and a DOSY experiment was carried out as above.

### 2.2.7 Computational details

All the DFT static calculations have been performed with the Gaussian09 set of programs,[24] using the B3LYP functional of Becke and Perdew.[25,26] The electronic configuration has been described with three different layers of basis set: SDD basis and pseudopotential at the metal center Zn,[27] 6-311G(d,p) at Si[28] and SVP with the standard split-valence basis set with a polarization function of Ahlrichs and co-workers for H, C, N, O and F.[29] Stationary points were characterized using vibrational analysis, and this analysis has been also used to calculate zero-point energies and thermal (enthalpy and entropy) corrections (298.15 K, 1 bar). We obtained improved electronic energies from single-point energy calculations using a 6-311G(d,p) basis set on all the atoms excluded Zn (SDD basis set and pseudopotential), a solvation contribution (PCM model,[30] toluene) and the dispersion corrections[31](EmpiricalDispersion=GD3BJ in the Gaussian09 E.01 package). These energies added to the SVP-level thermal corrections are named *G*.

## 2.3 Results and discussion

### 2.3.1 Alternating copolymerization of cyclohexene oxide and carbon dioxide

$L_xZnN(SiMe_3)_2$ complexes **1-5** were tested as catalysts for the ROCOP of cyclohexene oxide (CHO) and carbon dioxide. Initially, complex **1**, bearing a methyl substituent in the *ortho* position of the pyridine moiety and a 2,6-diisopropylphenyl substituent at the amido N, was tested under a variety of reaction conditions. Representative copolymerization runs are reported in Table 2.1 and discussed in the following. Some runs were carried out using 0.05 mmol of **1,** 4 mL CHO (monomer/catalyst mole ratio = 800) without solvent, for 17 h at 80 °C and increasing $CO_2$ pressures (see Table 2.1). Notably, the catalyst promoted the

copolymerization even at 1 atm of $CO_2$ pressure, and the polymerization rate increased at increasing $CO_2$ pressure[8] (cf. runs 1-3). The catalyst seems stable over extended reaction times, resulting in 70% CHO conversion in 62 h (cf. runs 3-5). High selectivities were observed in all runs, with carbonate linkages ranging between 86-98% (see Table 2.1). Reducing the temperature to 50 °C resulted in a lower productivity (see run 6). Since the polymerization tests were carried out charging in a glove box the autoclave with the zinc complexes in neat CHO and then pressurizing the reactor with $CO_2$ (see the paragraph 2.2.4), and since the fraction of ether linkages seems higher for shorter runs (cf. runs 3, 4 and 5), we suspected that some CHO homopolymerization can preferentially occur at the beginning of the reaction. As a matter of fact, run 7, carried out with CHO only, indicated that **1** is able to homopolymerize CHO in the absence of $CO_2$, suggesting that homo- and co-polymerization reactions can occur at the same time, albeit at different rates. As suggested by a reviewer, increasing the $CO_2$ pressure up to 40 atm resulted in a higher selectivity in carbonate linkage (99% vs. 96% at 25 atm and otherwise identical conditions, cf. runs 16 and 3). Moreover, carrying the copolymerization using 2 mL of toluene solvent and 2 mL of CHO resulted in carbonate selectivitity >99% even at 25 atm $CO_2$ pressure, although at the expense of TOF, as expected if the copolymerization rate depends on CHO concentration (cf. run 8 vs. run 3). Addition of 1 equiv of bis-(triphenylphosphorylidene)ammonium chloride (PPNCl, a typical cocatalyst used for mononuclear catalysts) resulted in switching the chemoselectivity of the reaction towards the prevailing formation of *cis*-cyclohexenecarbonate and in a reduction of the catalytic activity (see run 9). A similar behavior was observed, e. g., for a bimetallic iron(III) catalyst and explained suggesting that PPNCl promotes exchange reactions between the initiating metal carbonate species and chloride ions, thus favoring the ring closure reaction and the formation of *cis*-cyclohexenecarbonate through a double-inversion of CHO stereochemistry.[32] As originally addressed by Coates for BDI catalysts,[33] even subtle modifications of the coordination environment can result in dramatic changes of

catalytic activity. In this preliminary exploration of the title class of complexes, we devised some ligand variations aimed at addressing the importance of both steric and electronic substituent effects. Thus, catalyst **2**, bearing a much more sterically encumbered 2,6-dimethylphenyl substituent in the *ortho* pyridine position, was tested under similar conditions at 80 °C and 8 atm $CO_2$ pressure, also affording polycyclohexene carbonate with good selectivity (85% carbonate linkages), although at a lower rate with respect to **1** (cf. runs 2 and 10). A higher productivity was achieved under higher $CO_2$ pressure (cf. runs 10 and 11) as well as at higher temperature (run 12). Introduction of a methyl substituent on the carbon bridging the pyridine and the aniline moieties in catalyst **3** resulted in further reduction of the productivity, while maintaining a good selectivity (cf. run 13 vs. run 10). Subsequently, we tested catalyst **4**, maintaining the bulky *ortho* 2,6-dimethylphenyl substituent at the pyridine moiety like in **2** (and **3**), but carrying a less hindered 2,6-dimethylphenyl substituent also at the N-amido atom. Catalyst **4** tested at 80 °C and under 25 atm $CO_2$ pressure resulted significantly more active than **2** under identical conditions (cf. run 14 vs. run 11). Finally, catalyst **5**, featuring the same structure of **2-4** at the pyridine moiety and a strong electron-withdrawing (and less hindered) pentafluorophenyl substituent at the N-amido atom, showed the best performances in terms of TON, TOF and monomer conversion when tested under identical conditions (see run 15). GPC analysis of the polymer samples indicated that the molecular weights are low or moderate ($M_n$ of polycarbonates range between 2 and 11 kDa) and that the molecular weight distributions are very broad. This finding is not uncommon in the copolymerization of epoxides and $CO_2$ and it has been ascribed either to multi-site initiators[4] or to the formation in situ of diols and/or to the presence of protic impurities[10]. A polymer sample (produced in run 14 of Table 2.1) was repeateadly dissolved in methylene chloride and reprecipitated in methanol, resulting in two fractions: GPC analysis of the methanol soluble fraction (~ 30%) showed that it consists of a low MW polymer with $M_n$ = 3.3 kDa and $M_w/M_n$ = 1.2, while GPC analysis of the methanol insoluble fraction (~ 70%) indicated that it

consists of a higher MW polymer with $M_n$ = 34 kDa and $M_w/M_n$ = 3.6 (see Figure 2.16). A MALDI-ToF mass spectrum of the same sample in the m/z range 3000 – 7000 (Figure 2.17) showed the presence of linear poly(cyclohexenecarbonate) chains having either one hydroxyl and one -$OSiMe_3$ end groups or α,ω-dihydroxyl-end groups (*v. infra* for further discussion). The isolated polymer samples were analyzed by $^{13}C$ NMR: interestingly, inspection of the carbonyl region of the spectra (see e.g. Figure 2.13) indicated a prevailing content of m-centered tetrads with respect to r-centered tetrads,[33] with $P_m$ ranging between 0.60 and 0.67. The origin of the slight isotactic enrichment observed is possibly due to a chain-end mechanism, since non-chiral catalyst were used.

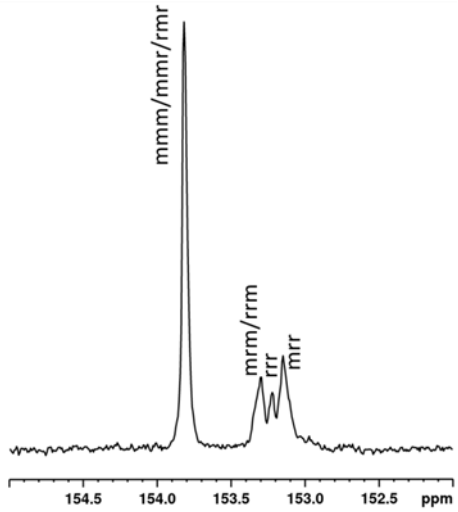


**Figure 2.13.** Carbonyl region of the $^{13}C$ NMR (150 MHz, $CDCl_3$) spectrum of a polycarbonate sample obtained in run 14 of Table 2.1.

**Table 2.1.** Copolymerization of cyclohexene oxide and $CO_2$ using pyridylamido Zn(II) catalysts **1-5**.

| Run | cat | p $CO_2$ (atm) | T (°C) | t (h) | conv (%)[b] | TON[c] | TOF ($h^{-1}$)[d] | carbonate linkages[e] (%) | $M_n$[f] (kDa) | $M_w/M_n$[f] |
|---|---|---|---|---|---|---|---|---|---|---|
| 1 | **1** | 1 | 80 | 17 | 8 | 64 | 4 | 88 | 4.0 | 12 |
| 2 | **1** | 8 | 80 | 17 | 30 | 240 | 14 | 87 | 5.8 | 18 |
| 3 | **1** | 25 | 80 | 17 | 40 | 320 | 19 | 96 | 5.5 | 22 |
| 4 | **1** | 25 | 80 | 4 | 16 | 128 | 32 | 86 | 7.3 | 19 |
| 5 | **1** | 25 | 80 | 62 | 70 | 560 | 9 | 98 | 6.5 | 14 |
| 6 | **1** | 25 | 50 | 17 | 15 | 136 | 8 | 90 | 10 | 14 |
| 7 | **1** | - | 80 | 4 | 9 | 72 | 18 | [g] | 24 | 1.7 |
| 8[h] | **1** | 25 | 80 | 17 | 25 | 100 | 6 | >99 | 13 | 6.7 |
| 9[i] | **1** | 25 | 80 | 17 | 7 | 56 | 3 | [j] | - | - |
| 10 | **2** | 8 | 80 | 17 | 18 | 144 | 8 | 85 | 1.8 | 11 |
| 11 | **2** | 25 | 80 | 17 | 30 | 240 | 14 | 98 | 7.5 | 7.4 |
| 12 | **2** | 25 | 100 | 17 | 40 | 320 | 19 | 98 | 9.4 | 6.3 |
| 13 | **3** | 8 | 80 | 17 | 13 | 106 | 6 | 87 | 3.4 | 19 |
| 14 | **4** | 25 | 80 | 17 | 49 | 392 | 23 | 95 | 8.1 | 8.6 |
| 15 | **5** | 25 | 80 | 17 | 58 | 464 | 27 | 98 | 11 | 8.7 |
| 16 | **1** | 40 | 80 | 17 | 42 | 336 | 20 | 99 | - | - |

[a] Excepting where differently specified, the runs were performed in neat CHO (4.0 ml) using 5.0 x $10^{-5}$ mol of Zn complex ( [CHO] / [Zn] ratio = 800 : 1). **[b]** CHO conversion determined by $^1$H NMR analysis of the polymerization mixture. [c] TON = mol of CHO consumed/mol of Zn catalyst. [d] TOF = TON/h. [e] Determined by integration of the methine resonances in the $^1$H NMR spectrum of the isolated polymer. [f] Determined by gel-permeation chromatography in THF at 30 °C versus polystyrene standards. [g] The product was poly(cyclohexene oxide). [h] Like in [a] but CHO = 2.0 ml; toluene = 2.0 ml. [i] Like in [a] but 1 equiv of PPNCl was added. [j] Main product was *cis*-cyclohexenecarbonate.

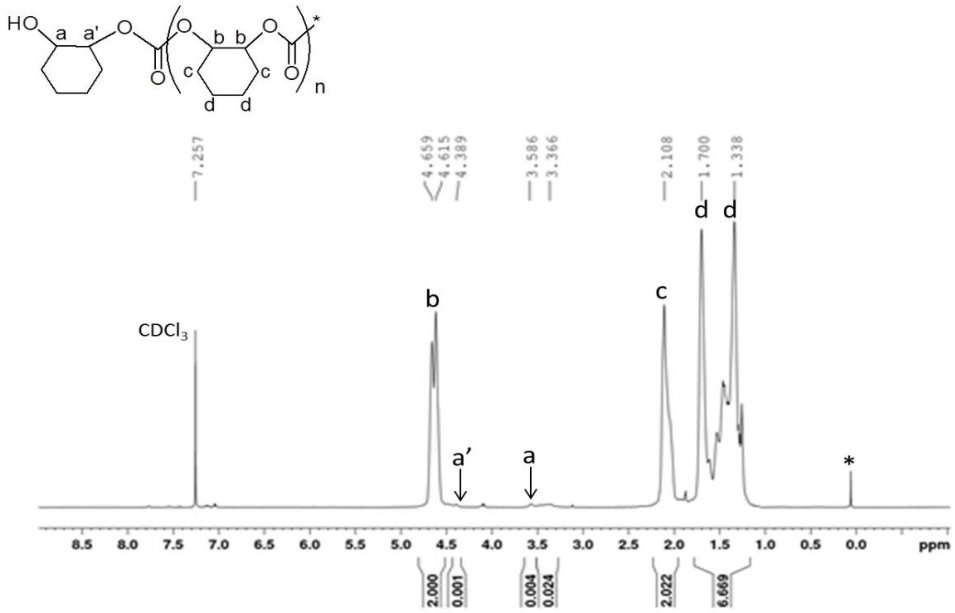


**Figure 2.14.** $^{1}$H-NMR ($CDCl_3$, 600 MHz, 298 K) of polycarbonate obtained in run 14 of Table 2.1 (* stands for silicon grease).

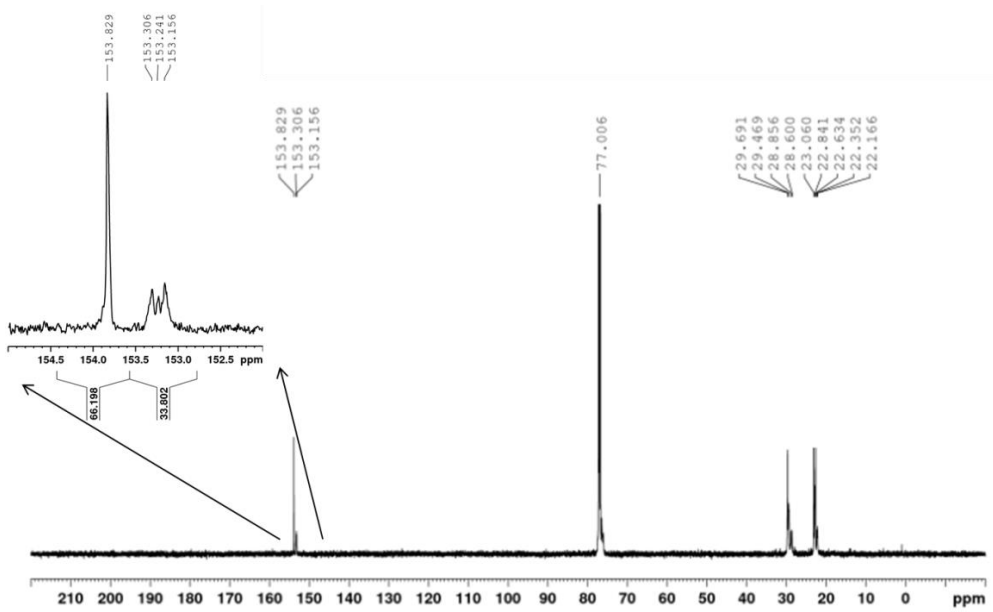


**Figure 2.15.** $^{13}$C-NMR ($CDCl_3$, 150 MHz, 298 K) of polycarbonate obtained in run 14 of Table 2.1.

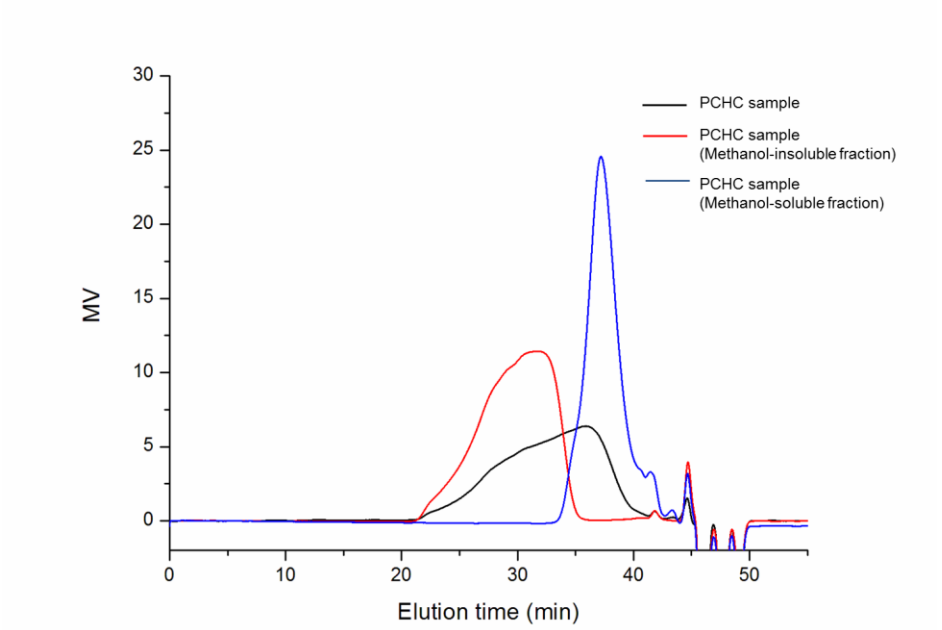


| Sample | Elution time (min) | Mn (kDa) | Mw/Mn |
|---|---|---|---|
| PCHC (run 14, Table 1) | 35 | 8,1 | 8,6 |
| MeOH-insoluble fraction | 31 | 34,0 | 3,6 |
| MeOH-soluble fraction | 37 | 3,3 | 1,2 |

**Figure 2.16.** GPC profiles for the PCHC sample of run 14 of Table 2.1 (black curve) with corresponding methanol-insoluble fraction (red curve) and methanol-soluble fraction (blue curve).

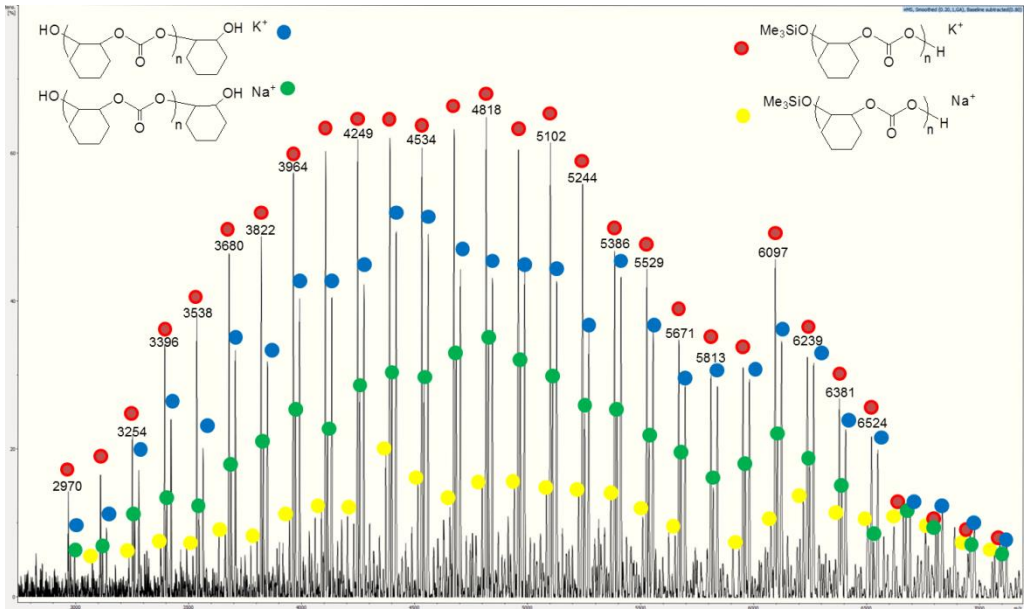


**Figure 2.17.** MALDI-TOF mass spectrum of PCHC sample (run 14, Table 2.1) in the m/z range: 3000 – 7000.

## 2.3.2 Mechanism of the copolymerization and DFT calculations

Seminal and elegant studies by Coates showed that the active species involved in (BDI)Zn catalysts for the alternating copolymerization of epoxides and carbon dioxide are dimeric $[(BDI)Zn(\mu\text{-}OR)]_2$ species which are converted to the corresponding dimeric $[(BDI)Zn(\mu\text{-}O_2COR)]_2$ species upon $CO_2$ insertion.[7] A cooperative bimetallic mechanism was suggested on the basis of kinetic studies and investigation of the elementary steps using model complexes. A key element for high catalytic activity was shown to be related to the dimer association equilibrium constant, with monomeric species and tightly bound dimers being poorly reactive or unreactive, while loosely bound fluxional dimers are highly reactive.[7] As mentioned in the introduction, the peculiarity of (BDI)Zn[6] and other dinuclear catalysts [8-12] is the fact that they do not require any cocatalyst. We wondered if dimeric

$[(L_x)Zn(\mu\text{-}OR)]_2$ and $[(L_x)Zn(\mu\text{-}O_2COR)]_2$ active species can be involved in our systems, too, also considering some similarities between the structures and the catalytic performance of the pyridylamido Zn catalysts reported here and those of the (BDI)Zn catalysts. We noticed that also in the case of $(BDI)ZnN(SiMe_3)_2$ complexes the active species were shown to be $[(BDI)Zn(\mu\text{-}OSiMe_3)]_2$ dimers, deriving from $CO_2$ insertion and subsequent elimination of trimethylsilyl isocyanate.[7] Thus, we monitored by $^1H$ NMR the reaction of complex **1** and a few equivalents of $CO_2$ in an NMR tube in toluene-$d_8$: after 5 min at 80°C, the resonances of complex **1** disappeared, while the resonance of $Me_3SiN{=}C{=}O$ appeared at $\delta$ = -0,10 ppm together with new resonances attributable to a $[L_1Zn(\text{-}OSiMe_3)]$[34] species (see Figure 2.18). Comparative diffusion NMR experiments performed on complex **1** and on the newly formed $[L_1Zn(\text{-}OSiMe_3)]$ species provided an estimation of their molecular masses, confirming the monomeric structure of **1** and suggesting a dimeric structure for the new species, i. e. $[(L_1)Zn(\mu\text{-}OSiMe_3)]_2$. Self-diffusion coefficients (D) of complex **1** and of the product of its reaction with $CO_2$ were calculated using the diffusion coefficient of TMSS as internal reference standard. A simple estimate of the molecular masses in solution (M) was obtained using Graham's law of diffusion: $D = K(T/M)^{1/2}$. At constant temperature and assuming that K is the same for all species in solution, the relative diffusion rate of a species A and that of the reference standard TMSS is $D_A/D_{TMSS} = (M_{TMSS}/M_A)^{1/2}$. The calculated M for complex **1** was 577 and that for the product of its reaction with $CO_2$ was 938, in reasonable agreement with the expected molecular weights (507.2 for **1** and 872.0 for $[(L_1)Zn(\mu\text{-}OSiMe_3)]_2$).

However, as noted by a reviewer, the possible formation of dimeric species in the reaction mixture does not prove their involvement in the catalytic cycle. To get some information on the initiating groups of the active species, a low molecular weight polymer sample prepared with catalyst **1** at a lower temperature (50 °C) and low CHO conversion was analyzed by MALDI-ToF high resolution MS, clearly showing the presence of two major distributions (see Figure 2.19) separated by 142.06 m.u. ,

which is the mass of the polymer repeating unit: both series correspond to linear polymer chains with a hydroxyl end group, but in the former one the other end group is an -$OSiMe_3$, while in the latter it is a -$N(SiMe_3)_2$.

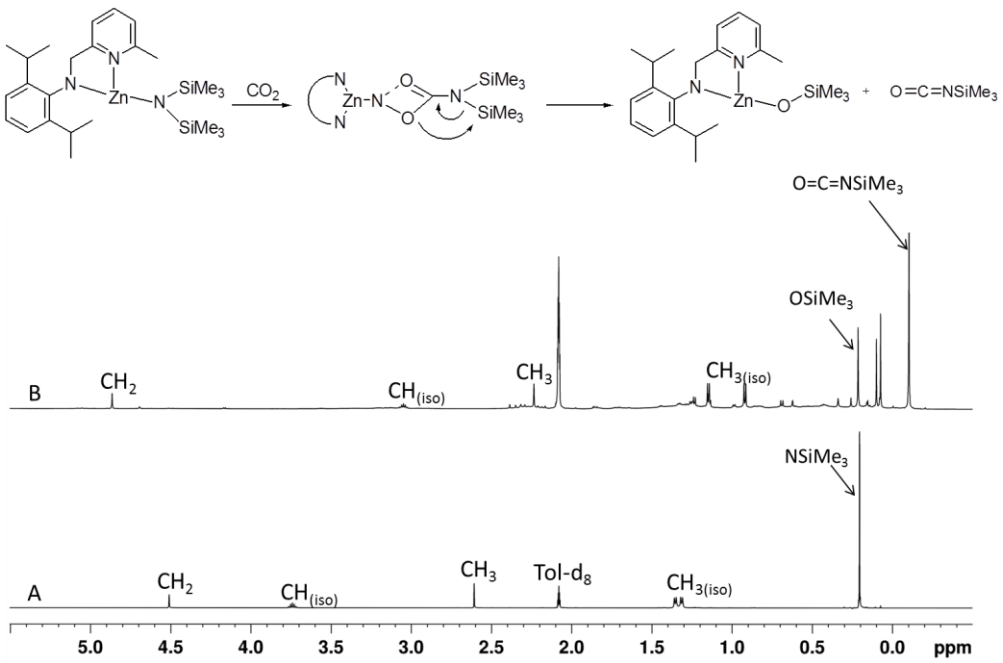


**Figure 2.18.** Aliphatic regions of the $^1$H-NMR (Tol-$d_8$, 600 MHz, 298 K) of complex **1** (A) and of the products of the reaction of **1** and $CO_2$ (B).

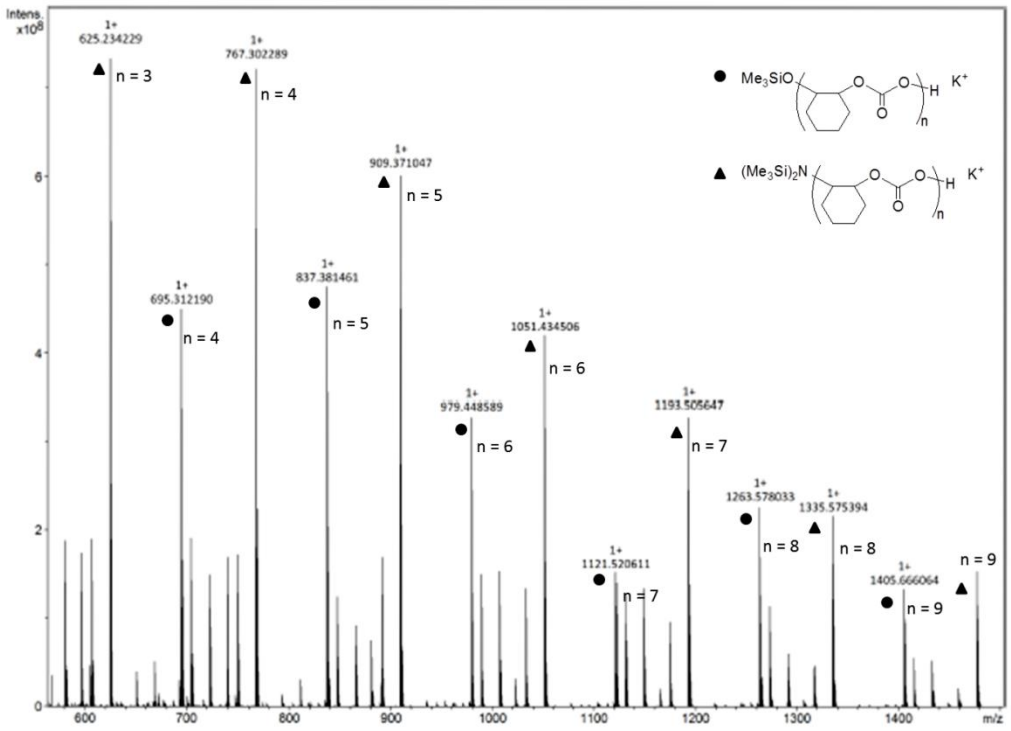


**Figure 2.19.** MALDI-TOF mass spectrum (doped with $K^+$) of a low molecular weight PCHO sample prepared using **1** as catalyst at 50 °C and 25 atm $CO_2$ pressure. $CO_2$ = 8 atm, T = 353 K. Circle labelled series calculated for $[(C_7H_{10}O_3)_n + C_3H_9OSi - 2H + K]^+$; Triangle labelled series calculated for $[(C_7H_{10}O_3)_n + C_6H_18NSi_2 - 2H + K]^+$.

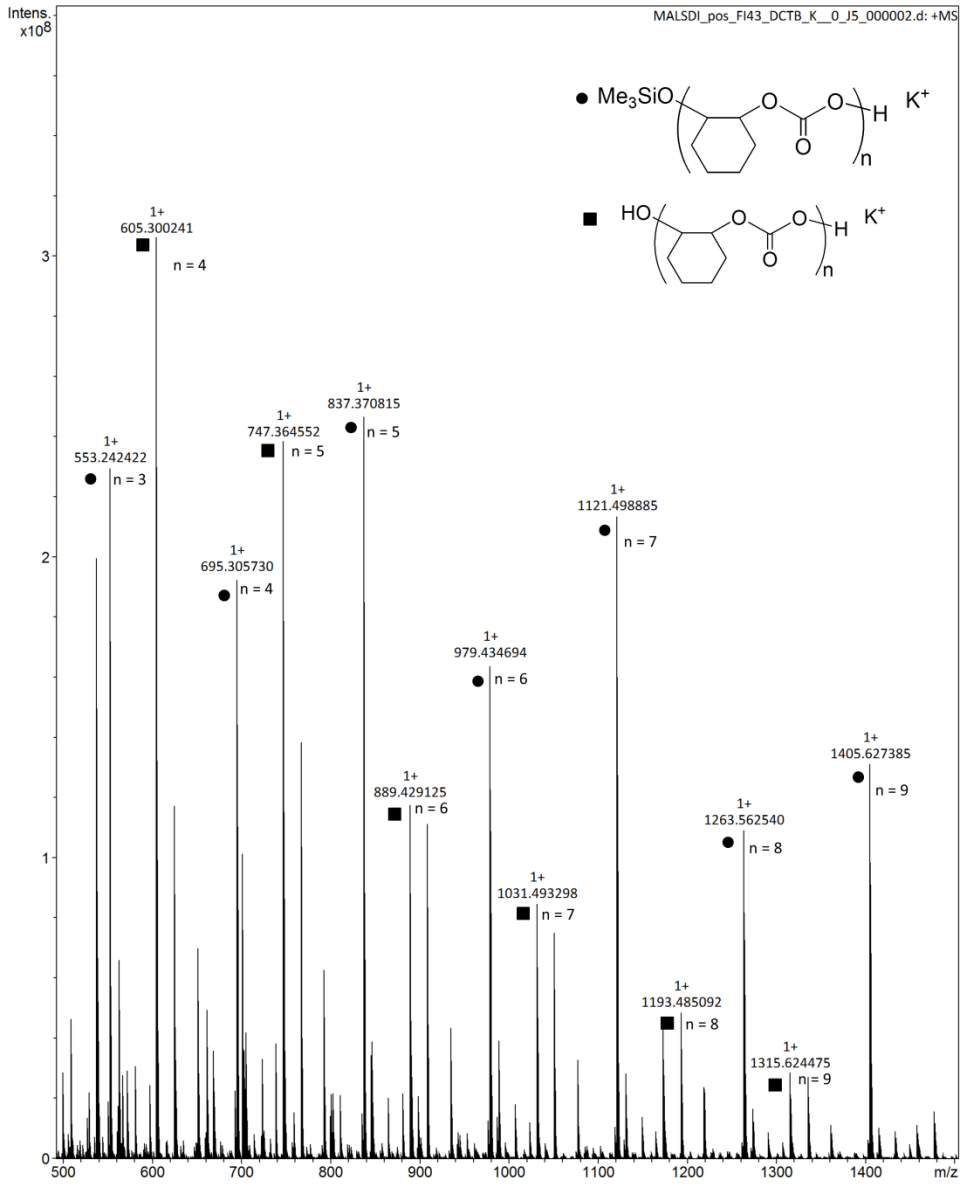


**Figure 2.20.** MALDI-TOF mass spectrum (doped with $K^+$) of a low molecular weight PCHO sample prepared using **1** as catalyst after 2 h aging under 8 atm of $CO_2$ at 80 °C before adding CHO. Circle labelled series calculated for $[(C_7H_{10}O_3)_n + C_3H_9OSi - 2H + K]^+$; Square labelled series calculated for $[(C_7H_{10}O_3)_n + OH - 2H + K]^+$.

This finding suggests that initiation occurs either after $CO_2$ insertion into Zn-$N(SiMe_3)_2$ bonds and subsequent formation of Zn-$OSiMe_3$ by trimethylsilyl isocyanate elimination (as observed for (BDI)Zn catalysts), or via insertion of CHO into the Zn-$N(SiMe_3)_2$ bond, at least when trimethylsilyl isocyanate elimination is slow, i. e. at lower temperatures. In fact, when a toluene solution of **1** was aged 2 h under 8 atm of $CO_2$ at 80 °C before adding CHO, the MS spectrum of the obtained polymer indicated the formation only of oligomers having a hydroxyl and an -$OSiMe_3$ end groups or α,ω-dihydroxyl-terminated chains (see Figure 2.20), the latter probably originated by adventitious traces of water and/or the *in situ* formation of cyclohexane-1,2-diol.[10] We also note that, while both monomeric $(L_x)Zn(OSiMe_3)$ and dimeric $[(L_x)Zn(\mu\text{-}OSiMe_3)]_2$ are plausible initiating species for the -$OSiMe_3$ end-capped macromolecules, the -$N(SiMe_3)_2$ end-capped ones can be reasonably produced only by monomeric $(L_x)Zn\text{-}N(SiMe_3)_2$ initiating species, $[(L_x)Zn(\mu\text{-}N(SiMe_3)_2]_2$ dimers being unlikely for steric reasons. These results as well as the broad MW distributions and the fractionation experiment described above, showing the presence of two polymer fractions having $M_n$ differing by one order of magnitude, suggest that different initiating species are involved in our pyridylamido Zn(II) catalysts. Unfortunately, several attempts to isolate model compounds such as $[(L_x)Zn(\mu\text{-}OR)]_2$ by alcholysis of either $(L_x)Zn(NSiMe_3)]_2$ or $(L_x)ZnEt$ resulted invariably in complex degradation *via* ligand dissociation. Similarly, attempts to obtain $[(L_x)Zn(\mu,\kappa^2\text{-}OAc)]_2$ species *via* either the reaction of $L_x$ and $Zn(OAc)_2$ or the reaction of $(L_x)ZnEt$ and AcOH met with failure. Following the suggestion of a reviewer, to assess the order of reactions on catalyst concentration we performed some copolymerization runs in glass flasks at atmospheric pressure using variable concentrations of Zn complex **4** ([**4**] = 6, 12, or 18 mM) (Figure 2.21), while maintaining all other conditions identical ($[CHO]_0$ = 7.5 M in 1 mL toluene, T = 80 °C) and we analyzed aliquots of the reaction mixtures taken at different intervals by $^1H$ NMR. Calculation of the dependence of initial rate of polymerization on the concentration of **4** resulted in an order in [Zn] = 2.5, compatible with the

involvement of dimeric active species. For (BDI)Zn catalysts, Coates reported a detailed kinetic study, measuring reaction orders for all the components of the copolymerization ([CHO], [$CO_2$], [Zn]) using in situ IR monitoring. He found orders in [Zn] ranging from 1 to 1.8 and suggested a bimetallic mechanism involving a bimetallic transition state starting from both monomeric and dimeric ground states.[7]

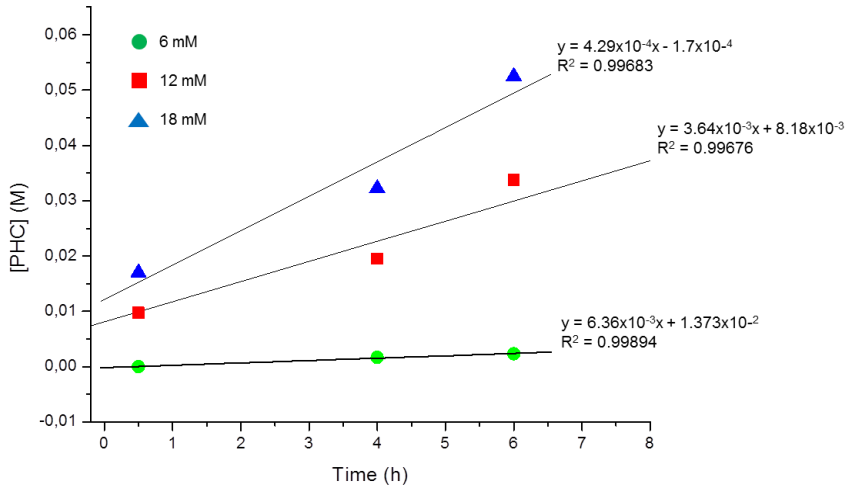


**Figure 2.21.** Plots to determine the initial rates depending on [**4**], using $^1$H NMR analysis of aliquots taken at defined intervals. The dotted lines indicate the linear fits, which are represented by their corresponding line equations. All experiments were conducted at 80 °C and 1 bar $CO_2$, with $[CHO]_0$ = 7.5 M in toluene.

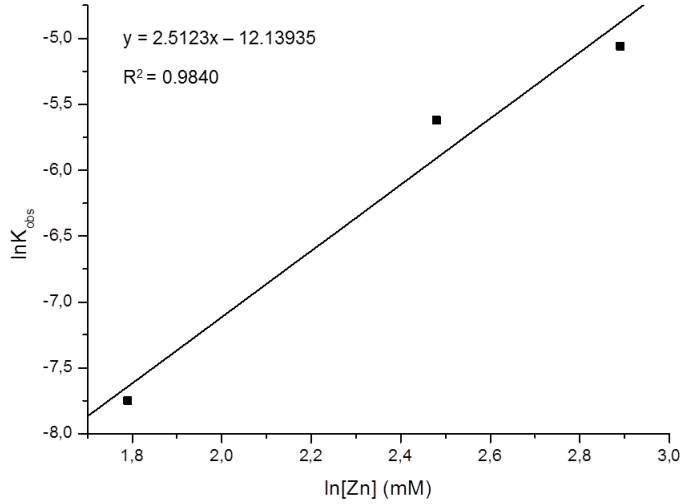


**Figure 2.22.** Plots showing the linear fit of the initial rate of polymerization vs the concentration of [**4]**, as determined by aliquot sampling and subsequent analysis using $^1$H NMR spectroscopy. Copolymerization conditions: $[CHO]_0$ = 7.5 M, in toluene at 80°C and 1 bar of $CO_2$.

DFT calculations were performed to estimate the free energy equilibria between monomeric $[(L_x)Zn(\text{-}OSiMe_3)]$ and dimeric $[(L_x)Zn(\mu\text{-}OSiMe_3)]_2$ species in solution. The comparison was extended also to $(BDI)Zn(\text{-}OSiMe_3)$ complexes where the active species were shown to be $[(BDI)Zn(\mu\text{-}OSiMe_3)]_2$ dimers, deriving from $CO_2$ insertion and subsequent elimination of trimethylsilyl isocyanate.[7] The geometries of dimeric complexes deriving from **1**, **2**, **3**, **4** and **5** are all referred to the most stable trans configuration ($C_2$ symmetry).

**Table 2.2.** Free energies comparison between dimeric and monomeric species $\Delta G_{dim} = (G_{dim} - 2G_{mon})$ for selected (BDI) Zn(II) systems[7] and the $[(L_x)Zn(\text{-}OSiMe_3)]$ (with x = 1-5) species. Negative $\Delta G_{dim}$ means that dimeric species are favored with respect to the monomeric ones.

| $[(L)Zn(\text{-}OSiMe_3)]$ | $\Delta G_{dim}$ (kcal/mol) |
|---|---|
| L=BDI with R =Et | -25.9 |
| L=BDI with R =Me | -22.6 |
| $L_1$ | -22.2 |
| $L_2$ | -9.2 |
| $L_3$ | -1.0 (3.8)[b)] |
| $L_4$ | -21.5 |
| $L_5$ | -20.5 |

[b)] Value calculated for the *R,S* isomer.

The results, reported in Table 2.2, show that $[(L_1)Zn(\text{-}OSiMe_3)]$, $[(L_4)Zn(\text{-}OSiMe_3)]$ and $[(L_5)Zn(\text{-}OSiMe_3)]$, deriving from the most active complexes **1**, **4**, **5**, present higher $\Delta G_{dim}$ values with respect to $[(L_2)Zn(\text{-}OSiMe_3)]$ and $[(L_3)Zn(\text{-}OSiMe_3)]$, deriving from the less active complexes **2** and **3**. Furthermore, the $\Delta G_{dim}$ values found for the former complexes are similar to those calculated for the BDI Zn(II) complexes. These findings suggest that the *in situ* formation of dimeric $[(L_x)Zn(\mu\text{-}OR)]_2$ and $[(L_x)Zn(\mu\text{-}O_2COR)]_2$ complexes, analogous to those involved in (BDI) Zn(II) systems, is energetically favoured in our pyridylamido Zn(II) catalysts as well. DFT optimized geometries of dimeric complexes **1** and **3** are reported in Figure 2.23 where the role of repulsive interactions played by 2,6-dimethylphenyl substituents (see dotted circle of Figure 2.23-B) and R = $CH_3$ in lowering the $\Delta G_{dim}$ value of system **3** with respect to **1** is evidenced by the increasing of $N_1$-Zn bond (in yellow in Figure 2.23).

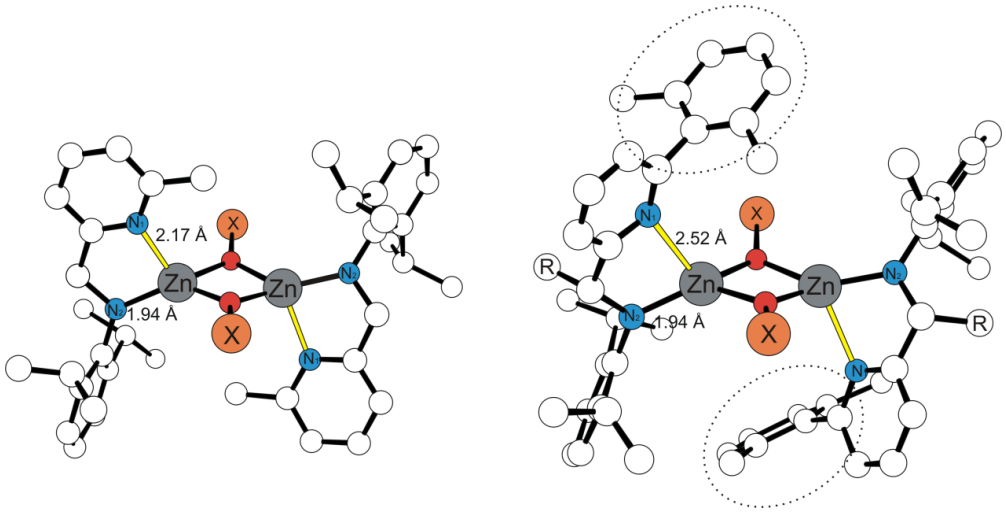


**Figure 2.23.** DFT optimized geometries for $[(L_1)Zn(\mu\text{-}O_2SiMe_3)]_2$ (A) and $[(L_3)Zn(\mu\text{-}O_2SiMe_3)]_2$ (B). Hydrogen atoms omitted for clarity and X = $SiMe_3$.

Figure 2.24 summarizes the proposed reaction mechanism according to the above reported experimental and theoretical evidence. $CO_2$ insertion into $(L_x)Zn\text{-}N(SiMe_3)_2$ followed by trimethylsilyl isocyanate elimination generates either monomeric $(L_x)Zn(\text{-}OSiMe_3)$ or dimeric $[(L_x)Zn(\mu\text{-}OSiMe_3)]_2$ active species. In the initiation step (I in Figure 2.24) CHO inserts into Zn–$OSiMe_3$ bond, via TS-I. Then the reaction proceeds via $CO_2$ insertion (TS-A in Figure 2.24) followed by CHO insertion (TS-B). The alternate iteration of reactions A and B leads to the formation of the polycarbonate.

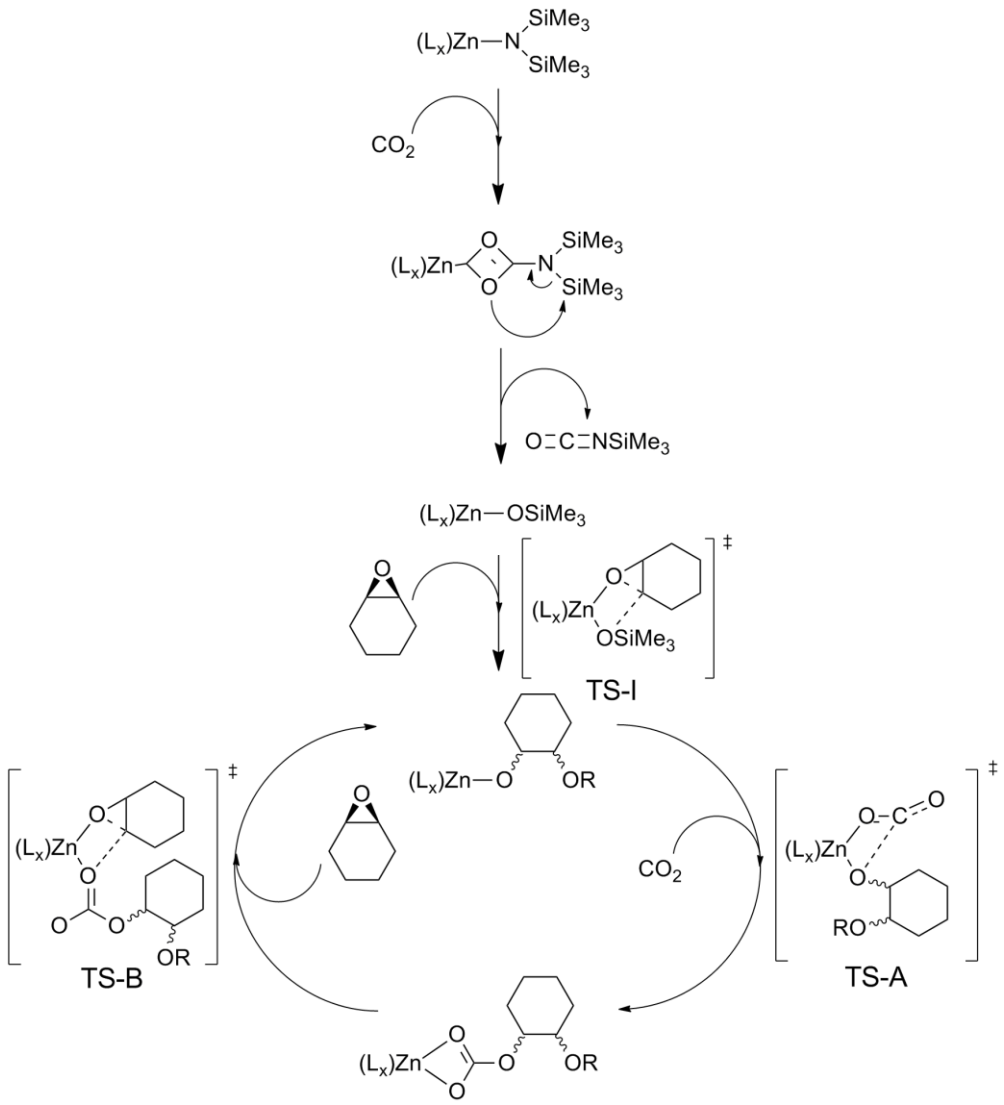


**Figure 2.24.** Reaction pathway for the $CO_2$/CHO copolymerization catalyzed by $(L_x)Zn$-$N(SiMe_3)_2$ complexes **1-5**.

We report further details concerning the activation energies for the ring opening of the epoxide, supposed to be the rate-determining step,[9] of both monomeric and dimeric active species (see Figures 2.25 and 2.26), as well as a comparison with the dimeric species obtained for (BDI) Zn(II) analogous complexes (see Figure 2.27).

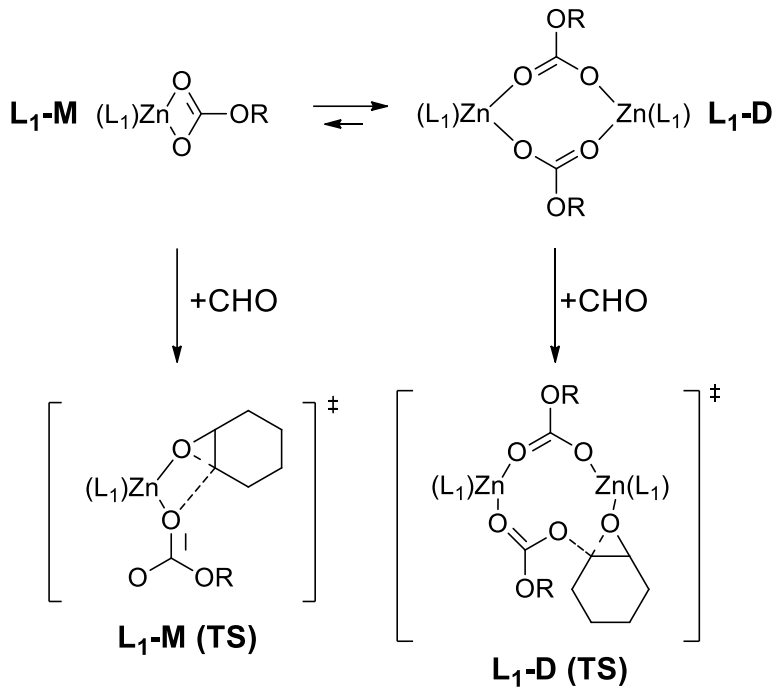


**Figure 2.25.** The equilibrium between the monomeric $(L_1)Zn(\eta^2\text{-}O_2COR)$ ($L_1$-M) and dimeric $[(L_1)Zn(\mu,\eta^2\text{-}O_2COR)]_2$ ($L_1$-D) and the respective transition states of the nucleophilic attack at the ring-opened epoxide.

The $L_1$-D propagating species is more stable by -17.6 kcal/mol with respect to the $L_1$-M, thus confirming an involvement of the dimeric specie even during the polymerization. Furthermore, the $\Delta G$ calculated for $L_1$-D (TS) (20.3 kcal/mol) are similar to the data reported by Kissling et al. (see Scheme 4 in ref. 9) of 21.6 kcal/mol for dinuclear Zinc complexes. This value, anyway, is comparable with the activation energy of $L_1$-M (TS) (20.7 kcal/mol), therefore the involvement of the monomeric specie cannot be excluded at all. The most reasonable hypothesis is that both the mechanisms (monomeric and dimeric) take place at the same time, thus most active specis are in the media during the polymerization. These data are in agreement also with the very broad molecular mass dispersion.

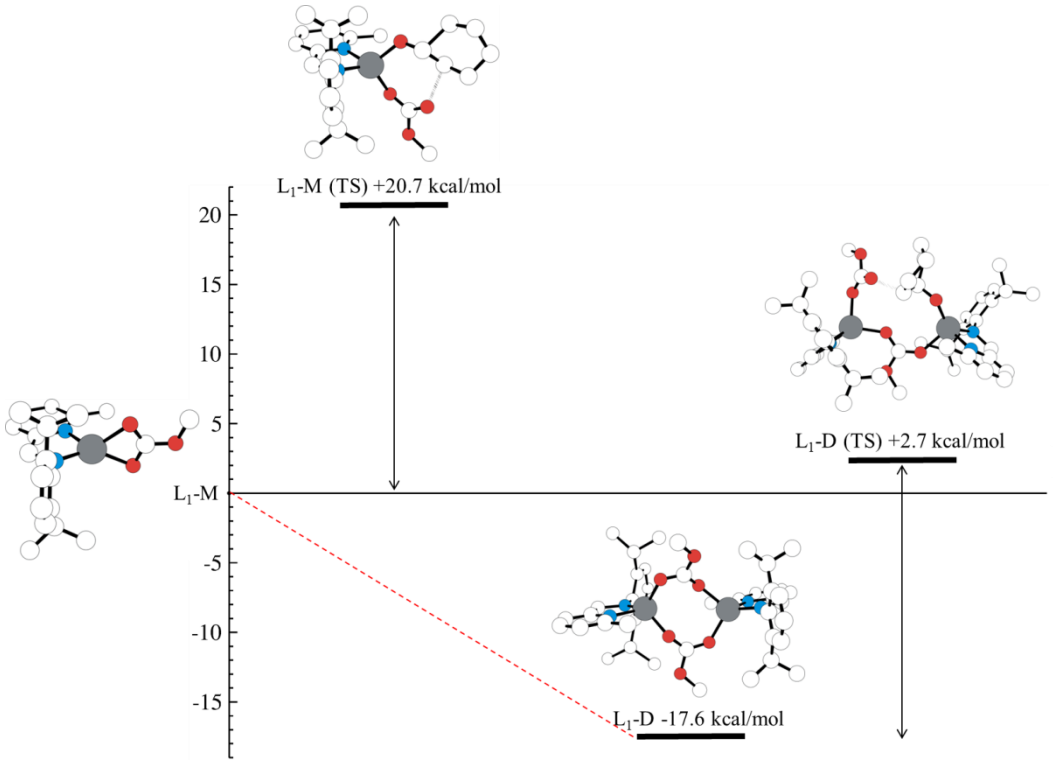


**Figure 2.26.** DFT calculated energy and optimized geometries for $L_1$-M, $L_1$-M (TS), $L_1$-D and $L_1$-D (TS). Hydrogens atom omitted for clarity.

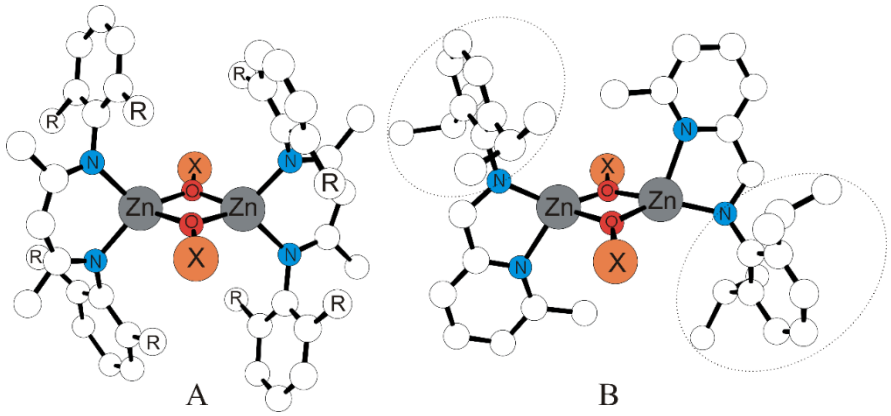


**Figure 2.27.** DFT optimized geometries for $[(BDI)Zn(\mu\text{-}OSiMe_3)]_2$ dimers with R = Et (A) and $[(L_1)Zn(\mu\text{-}O_2SiMe_3)]_2$ (B). Hydrogens atoms omitted for clarity and X = $SiMe_3$.

## 2.4 Conclusions

Several new pyridylamido Zn(II) complexes were synthesized and succesfully tested as "single component" catalysts for the alternating copolymerization of carbon dioxide and cyclohexene oxide also under rather mild conditions. A preliminary screening of some substituent variation in the coordination environment of the Zn catalyst addressed the potential tuning flexibility of steric and electronic features of this class of complexes. Both experimental and theoretical evidence suggested the involvement in the catalytic cycle of different initiating species, including dimeric $[(L_x)Zn(\mu\text{-}OR)]_2$ and $[(L_x)Zn(\mu\text{-}O_2COR)]_2$ complexes similar to those involved in benchmark (BDI) Zn(II) systems. Future work will be aimed at optimizing the catalyst structure to increase the copolymerization performance also using High Throughput Screening techniques and computational models.

## References


1. Schneiderman, D. K.; Hillmyer, M. A. 50th Anniversary Perspective: There Is a Great Future in Sustainable Polymers. *Macromolecules* **2017**, *50*, 3733-3749.
2. Zhang, X.; Fevre, M.; Jones, O. J.; Waymouth, R. M. Catalysis as an Enabling Science for Sustainable Polymers. *Chem. Rev*. **2018**, *118*, 839-885.
3. Artz, J.; Mueller, T. E.; Thenert, K.; Kleinekorte, J.; Meys, R.; Sternberg, A.; Bardow, A.; Leitner, W. Sustainable Conversion of Carbon Dioxide: An Integrated Review of Catalysis and Life Cycle Assessment. *Chem. Rev*. **2018**, *118*, 434-504.
4. Darensburg, D. J. Making Plastics from Carbon Dioxide: Salen Metal Complexes as Catalysts for the Production of Polycarbonates from Epoxides and $CO_2$. *Chem. Rev*. **2007**, *107*, 2388-2410.
5. Cheng, M.; Lobkovsky, E. B.; Coates, G. W. Catalytic Reactions Involving C1 Feedstocks: New High-Activity Zn(II)-Based Catalysts for the Alternating

Copolymerization of Carbon Dioxide and Epoxides. *J. Am. Chem. Soc*. **1998**, *120*, 11018-11019.

6. Coates, G. W.; Moore, D. R. Discrete Metal-Based Catalysts for the Copolymerization of $CO_2$ and Epoxides: Discovery, Reactivity, Optimization, and Mechanism. *Angew. Chem. Int. Ed.* **2004**, *43*, 6618-6639.
7. Moore D. R.; Cheng M., Lobkovsky E. B.; Coates G. W. Mechanism of the Alternating Copolymerization of Epoxides and $CO_2$ Using β-Diiminate Zinc Catalysts: Evidence for a Bimetallic Epoxide Enchainment. *J. Am. Chem. Soc.* **2003**, *125*, 11911-11924.
8. Lehenmeier, M. W.; Kissling, S., Altenbuchner, P. T.; Bruckmeier, C.; Deglmann, P.; Brym, A.-K.; Rieger B. Flexibly Tethered Dinuclear Zinc Complexes: A Solution to the Entropy Problem in $CO_2$/Epoxide Copolymerization Catalysis? *Angew. Chem. Int. Ed.* **2013**, *52*, 9821-9826.
9. Kissling, S.; Lehenmeier, M. W.; Altenbuchner, P. T., Kronast, A.; Reiter, M.; Deglmann, P.; Seemann, U. B.; Rieger, B. Dinuclear Zinc Catalysts with Unprecedented Activities for the Copolymerization of Cyclohexene Oxide and $CO_2$. *Chem. Comm*. **2015**, *51*, 4579-4582.
10. Jutz, F.; Buchard, A.; Kember, M. R.; Fredrickson, S. B.; Williams, C. K. Mechanistic Investigation and Reaction Kinetics of the Low-Pressure Copolymerization of Cyclohexene Oxide and Carbon Dioxide Catalyzed by a Dizinc Complex. *J. Am. Chem. Soc*. **2011**, *133*, 17395–17405.
11. Kember, M. R.; Knight, P. D.; Reung, P. T. R.; Williams, C. K. Highly Active Dizinc Catalyst for the Copolymerization of Carbon Dioxide and Cyclohexene Oxide at One Atmosphere Pressure. *Angew. Chem. Int. Ed*. **2009**, 48, 931.
12. Trott, G.; Saini, P. K.; Williams, C. K. Catalysts for $CO_2$/Epoxide Ring-Opening Copolymerization. *Phil. Trans. R. Soc. A* **2016**, 374:20150085.
13. Zuccaccia, C.; Busico, V.; Cipullo, R.; Talarico, G.; Froese, R. D. J.; Paul C. Vosejpka, P. C., Hustad, P. D.; Macchioni, A. On the First Insertion of α-Olefins

in Hafnium Pyridyl-Amido Polymerization Catalysts. *Organometallics* **2009**, *28*, 5445–5458.

14. Sun, W. H.; Song, S.; Li, B.; Redshaw, C.; Hao, X.; Li, Y.-S.; Wang, F. Ethylene Polymerization by 2-Iminopyridylnickel Halide Complexes: Synthesis, Characterization and Catalytic Influence of the Benzhydryl Group. *Dalton Trans.*, **2012**, *41*, 11999–12010.
15. Annunziata, L.; Pappalardo, D.; Tedesco, C.; Pellecchia, C. Isotactic-Specific Polymerization of Propene by a $C_s$-Symmetric Zirconium(IV) Complex Bearing a Dianionic Tridentate [$^-$NNN$^-$] Amidomethylpyrrolidepyridine Ligand. *Macromolecules* **2009**, *42*, 5572– 5578.
16. Li, G.; Lamberti, M.; D'Amora, S.; Pellecchia, C. C1-symmetric Pentacoordinate Anilidopyridylpyrrolide Zirconium(IV) Complexes as Highly Isospecific Olefin Polymerization Catalysts. *Macromolecules* **2010**, *43*, 8887–8891.
17. Li, G., Zuccaccia; C., Tedesco; C., D'Auria; I., Macchioni, A.; Pellecchia, C. NMR Spectroscopy and X-ray Characterisation of Cationic N-Heteroaryl-Pyridylamido Zr(IV) complexes: A Further Level of Complexity for the Elusive Active Species of Pyridylamido Olefin Polymerization Catalysts. *Chem. Eur. J.* **2014**, *20*, 232-244.
18. D'Auria, I.; Milione, S.; Caruso, T.; Balducci, G.; Pellecchia, C. Synthesis of Hyperbranched Low Molecular Weight Polyethylene Oils by an Iminopyridine Nickel(II) Catalyst. *Polym. Chem.* **2017**, *8*, 6443–6454.
19. Annunziata, L.; Pragliola, S.; Pappalardo, D.; Tedesco, C.; Pellecchia, C. New (Anilidomethyl)pyridine Titanium(IV) and Zirconium(IV) Catalyst Precursors for the Highly Chemo- and Stereoselective cis-1,4-Polymerization of 1,3-Butadiene. *Macromolecules* **2011**, *44*, 1934–1941.
20. D'Auria, I.; Tedesco, C.; Mazzeo, M.; Pellecchia, C. New Homoleptic bis(Pyrrolylpyridiylimino) Mg(II) and Zn(II) Complexes as Catalysts for the

Ring Opening Polymerization of Cyclic Esters via an "Activated Monomer" Mechanism. *Dalton Trans*. **2017**, *46*, 12217-12225.

21. Arai, T.; Suzuki, K. Design and Synthesis of Chiral Imidazolidine-Pyridine Ligands. *Synlett* **2009**, *19*, 3167–3170
22. Domski, G. J.; Lobkovsky, E. B.; Coates, G. W. Polymerization of α-Olefins with Pyridylamidohafnium Catalysts: Living Behavior and Unexpected Isoselectivity from a $C_s$-Symmetric Catalyst Precursor. *Macromolecules* **2007**, *40*, 3510-3513.
23. Lamberti, M.; Gliubizzi, R.; Mazzeo, M.; Tedesco, C; Pellecchia, C. Bis(phenoxyimine)zirconium and -titanium Catalysts Affording Prevailingly Syndiotactic Polypropylenes via Opposite Modes of Monomer Insertion. *Macromolecules* **2004**, *37*, 276-282.
24. Gaussian 09, Revision E.01, Frisch, M.J.; Trucks, G.W.; Schlegel, H.B.; Scuseria, G.E.; Robb, M.A.; Cheeseman, J.R.; Montgomery, Jr., J.A.; Vreven, T.; Kudin, K.N.; Burant, J.C.; Millam, J.M.; Iyengar, S.S.; Tomasi, J.; Barone, V.; Mennucci, B.; Cossi, M.; Scalmani, G.; Rega, N.; Petersson, G.A.; Nakatsuji, H.; Hada,M.; Ehara, M.; Toyota, K.; Fukuda, R.; Hasegawa, J.; Ishida, M.; Nakajima, T.; Honda, Y.; Kitao, O.; Nakai, H.; Klene, M.; Li, X.; Knox, J.E.; Hratchian, H.P.; Cross, J. B.; Bakken, V.; Adamo, C.; Jaramillo, J.; Gomperts, R.;Stratmann, R.E.; Yazyev, O.; Austin, A.J.; Cammi, R.; Pomelli, C.; Ochterski, J.W.; Ayala, P.Y.; Morokuma,K.; Voth, G.A.; Salvador, P.; Dannenberg, J.J.; Zakrzewski, V.G.; Dapprich, S.; Daniels, A.D.; Strain, M.C.;Farkas, O.; Malick, D.K.; Rabuck, A.D.; Raghavachari, K.; Foresman, J.B.; Ortiz, J.V.; Cui, Q.; Baboul, A.G.;Clifford, S.; Cioslowski, J.; Stefanov, B.B.; Liu, G.; Liashenko, A.; Piskorz, P.; Komaromi, I.; Martin, R.L.; Fox,D.J.; Keith, T.; Al-Laham, M.A.; Peng, C.Y.; Nanayakkara, A.; Challacombe, M.; Gill, P.M.W.; Johnson, B.;Chen, W.; Wong, M.W.; Gonzalez, C.; and Pople, J.A. Gaussian, Inc., Wallingford CT, **2004**.

25. Becke, A. Density-Functional Exchange-Energy Approximation With Correct Asymptotic Behavior. *Phys. Rev. A* **1988**, *38*, 3098-3100.
26. Perdew, J. P. Density-Functional Approximation for the Correlation Energy of the Inhomogeneous Electron Gas. *Phys. Rev. B* **1986**, *33*, 8822-8824; (b) Perdew, J. P. Erratum: Density-Functional Approximation for the Correlation Energy of the Inhomogeneous Electron Gas. *Phys. Rev. B* **1986**, *34*, 7406-7406.
27. Wadt, W. R.; Hay, P. J., Ab Initio Effective Core Potentials for Molecular Calculations. Potentials for Main Group Elements Sodium to Bismuth. *J. Chem. Phys.* **1985**, *82*, 284-298; (b) Hay, P. J.; Wadt, W. R., Ab Initio Effective Core Potentials for Molecular Calculations. Potentials for Potassium to Gold Including the Outermost Core Orbitals. *J. Chem. Phys.* **1985**, *82*, 299-310.
28. McLean, A. D.; Chandler, G. S. Contracted Gaussian Basis Sets for Molecular Calculations. I. Second Row Atoms, Z=11–18. *J. Chem. Phys.* **1980**, *72*, 5639-5648.
29. Schäfer, A.; Horn, H.; Ahlrichs, R. Fully Optimized Contracted Gaussian Basis Sets for Atoms Lithium to Krypton. *J. Chem. Phys.* **1992**, *97*, 2571-2577.
30. Barone, V.; Cossi, M. Quantum Calculation of Molecular Energies and Energy Gradients in Solution by a Conductor Solvent Model. *J. Phys. Chem. A* **1998,** *102*, 1995-2001.
31. Grimme, S.; Antony, J.; Ehrlich, S.; Krieg, H. A Consistent and Accurate Ab Initio Parametrization of Density Functional Dispersion Correction (DFT-D) For the 94 elements H-Pu. *J. Chem. Phys.* **2010**, *132*, 154104; (b) Grimme, S., Accurate Description of Van der Waals Complexes by Density Functional Theory Including Empirical Corrections. *J. Comput. Chem.* **2004,** *25*, 1463-1473.
32. Buchard, A.; Kember, M. R.; Sandeman, K. G.; Williams, C. K. A Bimetallic Iron(III) Catalyst for $CO_2$/Epoxide Coupling. *Chem. Comm.* **2011**, *47*, 212–214.
33. Moore, D. R.; Cheng, M.; Lobkovsky, E: B.; Coates, G. W. Electronic and Steric Effects on Catalysts for $CO_2$/Epoxide Polymerization: Subtle

Modifications Resulting in Superior Activities. *Angew. Chem. Int. Ed.* **2004**, *43*, 6618-6639.

34. Cheng, M.; Darling, N. A.; E. Lobkovsky, E. B.; Coates, G. W. Enantiomerically-Enriched Organic Reagents Via Polymer Synthesis: Enantioselective Copolymerization of Cycloalkene Oxides and $CO_2$ Using Homogeneous, zinc-based catalysts. *Chem. Commun.* **2000**, 2007–2008.
35. Sita L. R.; Babcock J. R.; Xi R. Facile Metathetical Exchange Between Carbon Dioxide and the Divalent Group 14 Bisamides $M[N(SiMe_3)_2]_2$ (M = Ge and Sn). *J. Am. Chem. Soc*. **1996**, *118*, 10912-10913.

The work presented in this chapter has been published as: D'Auria, I.; D'Alterio, M. C.; Talarico, G.; Pellecchia, C.; Alternating Copolymerization of $CO_2$ and Cyclohexene Oxide by New Pyridylamidozinc(II) Catalysts, *Macromolecules* **2018**, *51*, 23, 9871-9877 DOI: 10.1021/acs.macromol.8b01651

# Chapter 3

# Tailor-made block copolymers of L-, D-, *rac*-lactides and ε-caprolactone *via* one-pot sequential ring opening polymerization by pyridylamidozinc(II) catalysts


## Abstract

Three-coordinated Zn(II) complexes bearing sterically encumbered bidentate monoanionic [N,N$^-$] pyridylamido ligands efficiently catalyze the ring opening polymerization of lactide (LA) and ε-caprolactone (CL). Owing to the polymerization controlled nature and high rate, precise stereodiblock poly(LLA-*b*-DLA) with different block lengths can be easily produced by one-pot sequential monomer addition at room temperature in short reaction times. NMR, SEC and DSC analyses confirm the production of highly isotactic diblock copolymers which crystallize in the high melting stereocomplex phase. Stereo-triblock and tetrablock copolymers of L-LA, D-LA and *rac*-LA have been synthesized similarly. Finally, a diblock poly(CL-*b*-LA) has been easily obtained by sequential addition of ε-caprolactone and lactide under mild conditions.


## 3.1 Introduction

Aliphatic polyesters are among the most desirable targets of a sustainable polymer industry in a circular economy.[1] Indeed, there is a clear and urgent need for biodegradable polymeric materials for non-durable or disposable applications, as replacements of conventional commodity plastics, i. e. polyolefins and poly(ethylene terephthalate), whose 'fake degradation' is behind the problem of microplastic pollution in water.[2]

With a market of roughly 300 ktons/year which is growing steadily, poly(lactic acid) (PLA) is by far the most important polymer in this class from the application standpoint.[3,4] PLA is produced via ring opening polymerization (ROP) of lactide, the dimeric lactone of lactic acid, totally derived from annually renewable resources (e. g. starch obtained from corn or sugar beet). The only ROP catalyst used industrially to produce PLA is currently the rather simple Sn(II) 2-ethylhexanoate ($Sn(Oct)_2$).[3-5] This cheap and moderately active compound affords rather poor stereocontrol in polymerization and suffers from the occurrence of transesterification processes broadening the polymer dispersity. On the other hand, since the degradation of PLA yields lactic acid, which is easily metabolized in the human body, PLA has several sophisticated biomedical applications, such as resorbable medical implants that require long strength retention, and microspheres and microcapsules of low-molecular-weight for drug delivery systems.[5,6] Thus, the cytotoxicity of Sn residues in PLA is a serious matter of concern, and it is expected that, as soon as catalysts with a convenient cost/performance balance are identified, $Sn(Oct)_2$ will ultimately be abandoned. Although hundreds of catalysts for the ROP of lactide and lactones have been reported in the last two decades, catalysts combining non-toxicity, high activity and well controlled polymerization are rare.[3,4] Examples of catalysts based on biologically benign metals include heteroleptic complexes of Mg(II) and Zn(II) of the type LM-X, with L = β-diiminate,[7-11] trispyrazolylborate,[12] N-heterocyclic carbene[13,14] or phenolate-based[15-21] ligands, and X = alkyl, alkoxy, dialkylamido.

An appealing target for ROP catalysts is the ability to afford "tailor-made" aliphatic polyesters block copolymers.[22] E. g., since PLLA and PDLA co-crystallize as a stereocomplex phase showing improved properties with respect to the homochiral PLA's,[23] the production of stereo-diblock and stereo-multiblock PLA's by stereoselective catalysts has been extensively investigated.[24-27] Diblock copolymers of LA and ε-caprolactone (CL) have been also studied since they may combine the complementary features of the two homopolymers.[28-31] Moreover, ABA triblock copolymers, comprising e. g. two isotactic crystalline PLLA segments as the A-end

blocks and a soft, low $T_g$ amorphous polyester as the B-midblock, have been extensively studied as attractive degradable and sustainable alternatives to industrially relevant SBS thermoplastic elastomers.[22,32-36] The synthetic strategy for the production of such ABA block copolyesters usually involves the preparation of an αω-dihydroxy capped macroinitiator of the B-midblock followed by ROP of L-lactide (or D-lactide or *rac*-lactide).[22,23] PLLA−PDLA diblocks, PCL-PLA diblocks and ABA triblock copolyesters were also produced by sequential addition of the monomers using living catalysts, although very long reaction times (many hours or days) were required.[28-31,37,38] Only recently, Kol *et al.* reported extremely active Mg catalysts bearing monoanionic tetradentate pyridyldiaminophenolate ligands for the rapid production of stereoblock PLA's and diblock and multiblock PCL-PLA copolymers by one-pot sequential addition of the monomers.[39-41]

Following our studies concerning pyridylamido or pyridylimino metal complexes as catalysts for the polymerization of olefins,[42-46] and the ring opening polymerization of cyclic esters,[47-49] here we report heteroleptic Zn(II) pyridylamido complexes (see Scheme 3.1) functioning as very active catalysts for the ROP of L-, D- and *rac*-lactides and ε-caprolactone. The controlled nature and high rate of the polymerization allowed the synthesis of well-defined diblock copolymers PLLA-*b*-PDLA or PCL-*b*-PLLA, stereotriblock copolymers, such as PLLA-*b*-PDLA-*b*-PLLA, PLLA-*b*-PDLLA-*b*-PDLA, PCL-*b*-PLLA-*b*-PDLA, and stereotetrablock PLLA-*b*-PDLA-*b*-PLLA-*b*-PDLA, by one-pot sequential additions of the monomers under mild conditions and short reaction times.

## 3.2 Experimental section

### 3.2.1 General methods

All manipulations involving air and/or moisture-sensitive compounds were performed under a nitrogen atmosphere in a Braun Labmaster glovebox or using Schlenk techniques. Glassware used were dried in an oven at 120 °C overnight and

exposed to vacuum–nitrogen cycles. All solvents were dried as follows: toluene was refluxed over metallic sodium, dichloromethane was refluxed over $CaH_2$, benzene, hexane and tetrahydrofuran were refluxed over sodium-benzophenone; they were distilled under nitrogen before use. Deuterated solvents were purchased from Aldrich and stored in the glovebox over 3 Å molecular sieves before use. Lactide was purified by crystallization from dry toluene. ε-Caprolactone was dried with $CaH_2$ for 24 h at room temperature and then distilled under reduced pressure. All other chemicals were commercially available and used as received unless otherwise stated.

NMR spectra were recorded using either a Bruker Advance 300, or 400 or a Bruker 600 MHz Ascend 3 HD spectrometer. Chemical shifts (δ) are expressed as parts per million and coupling constants (J) in hertz. $^{1}H$ NMR spectra are referenced using the residual solvent peak at δ 7.26 for $CDCl_3$, δ 5.32 for $CD_2Cl_2$ and δ 7.16 for $C_6D_6$. $^{13}C$ NMR spectra are referenced using the residual solvent peak at δ 77.22 for $CDCl_3$, δ 53.84 for $CD_2Cl_2$ and δ 128.06 for $C_6D_6$.

MALDI-TOF-MS spectra of polymer samples were acquired using a Bruker solariX XR Fourier transform ion cyclotron resonance mass spectrometer equipped with a 7 T refrigerated actively-shielded superconducting magnet. The samples were ionized in positive ion mode using the MALDI ion source. The mass range was set to *m/z* 150 – 9000. The laser power was 15% and 15 laser shots were used for each scan. The mass spectra were calibrated externally using a mix of peptide clusters in MALDI ionization positive ion mode. A linear calibration was applied. The samples were dissolved in THF (1mg/mL). Trans-2-[3-(4-tert-Butylphenyl)-2-methyl 2-propenylidene]malononitrile (DCTB) was used as the matrix with potassium trifluoroacetate (KTFA) as cationizing agent. The matrix was dissolved in THF at a concentration of 10 mg/mL and ~ 2 mg of KTFA was added to the solution. The matrix and polymer solutions were mixed together in a 4:1 ratio and this mixture was spotted on the MALDI plate and left to dry. After evaporation of the solvent, the MALDI target was introduced into the spectrometer.

The molecular weights ($M_n$ and $M_w$) and the dispersities ($M_w/M_n$) of polymer samples were measured by size exclusion chromatography (SEC) at 30 °C, using THF as solvent, an eluent flow rate of 1 mL $min^{-1}$, and narrow polystyrene standards as reference. The measurements were performed on a Waters 1525 binary system equipped with a Waters 2414 RI detector using four Styragel columns (range 1 000−1000000 Å).

Differential scanning calorimetry (DSC) analysis was performed on a TA Q2000 (TA Instruments) according to the following program: Equilibrate at -40°C; Ramp 10.00 °C/min to 220 °C; Ramp 10.00 °C/min to -40.00 °C; Ramp 10.00 °C/min to 220 °C. The instrument was calibrated for temperature and enthalpy by a high purity indium (156.60 °C, 28.45 J $g^{-1}$) standard. DSC analyses were carried out on films obtained by casting from 1 wt. % dichloromethane solutions at room temperature.

### 3.2.2 Synthesis and characterization

$L^1H$-$L^4H$ and the zinc complexes $L^xZnN(SiMe_3)_2$ (x = 1-4) (Scheme 3.1) were synthesized as previously reported in Chapter 2.[44,50]

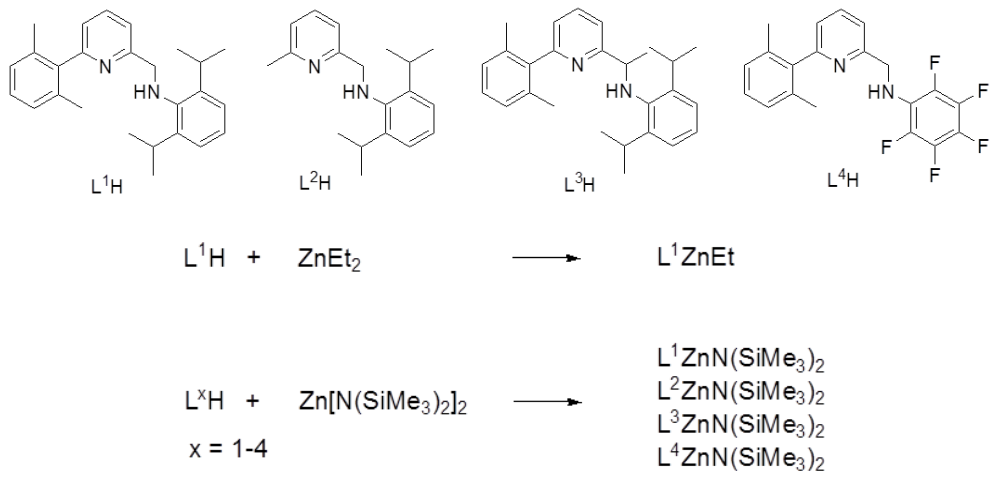


**Scheme 3.1.** Pyridylamino ligands used for the synthesis of the Zn(II) complexes.

**Synthesis of complex $L^1$ZnEt.** In an Mbraun glovebox, a solution of the proligand $L^1H$ (0.200 g, 0.54 mmol) in dichloromethane (2.5 mL) was added dropwise into a solution of $ZnEt_2$ (0.073 g, 0.59 mmol) in dichloromethane (2.5 mL). The resulting mixture was stirred at room temperature for 12 hours. The solvent was removed *in vacuo* and the solid residue was washed using dry hexane to obtain a white powder (yield: 0.213 g, 85%). $^1$H NMR ($CD_2Cl_2$, 600 MHz, 298 K) (Figure 3.1): δ -0.57 (2H, q, $^3$J = 8.4 Hz, Zn–*C*$H_2$CH$_3$), 0.63 (3H, t, $^3$J = 8.4 Hz, Zn–CH$_2$*C*$H_3$), 0.99 (6H, d, $^3$J = 7.0 Hz, CH(*C*$H_3$)$_2$), 1.15 (6H, d, $^3$J = 7.0 Hz, CH(*C*$H_3$)$_2$), 2.04 (6H, s, C*H*$_3$), 3.39 (2H, sept, $^3$J = 7.0 Hz, *C*H(CH$_3$)$_2$), 4.56 (2H, s, *C*$H_2$), 6.97 (1H, m, *H*$_{Ar}$) 7.03 (2H, d, $^3$J = 7.2 Hz, *H*$_{Ar}$), 7.14 (2H, d, $^3$J = 7.8 Hz, *H*$_{Ar}$), 7.23 – 7.28 (2H, m, *H*$_{Ar}$), 7.35 (1H, d, $^3$J = 7.8 Hz, H$_{Ar}$), 7.89 (1H, t, $^3$J = 7.8 Hz, H$_{Ar}$).

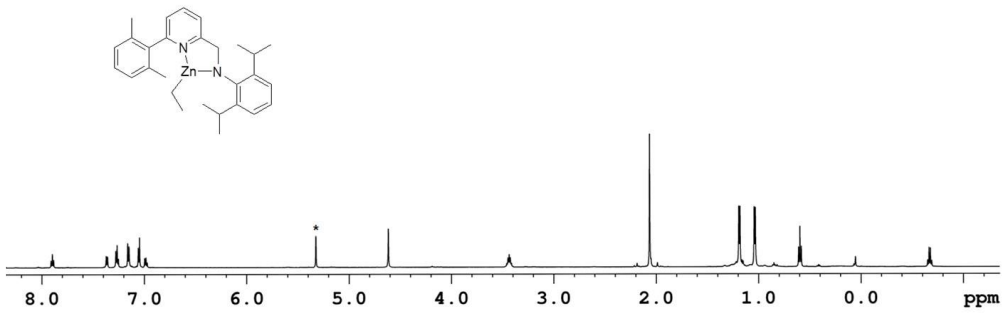


**Figure 3.1.** $^1$H-NMR ($CD_2Cl_2$, 600 MHz, 25°C) of complex **$L^1$ZnEt** (* stands for residual solvent resonances).

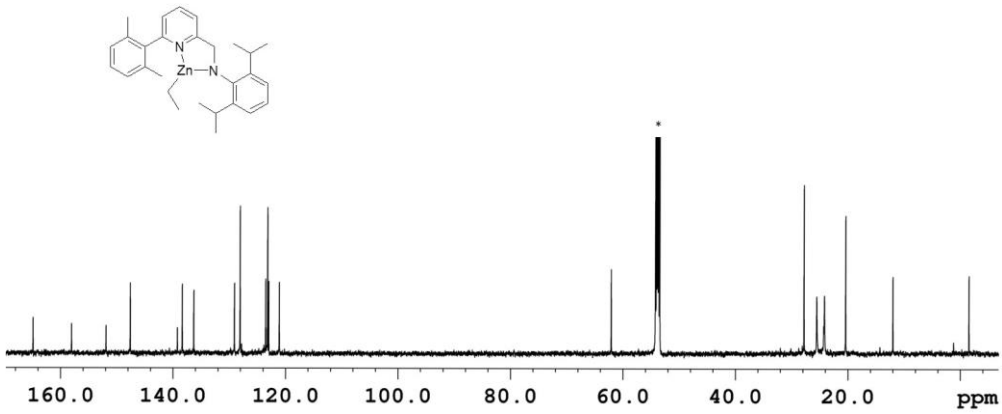


**Figure 3.2.** $^{13}$C-NMR ($CD_2Cl_2$, 150 MHz, 25°C) of complex **L$^1$ZnEt** (* stands for residual solvent resonances).

$^{13}C\{^1H\}$ NMR ($CD_2Cl_2$, 150 MHz, 298 K) (Figure 3.2): δ -1.55 (1C, Zn-*C*$H_2$$CH_3$), 11.97 (1C, Zn-$CH_2$*C*$H_3$), 20.39 (2C, *C*$H_3$), 24.17(2C, CH(*C*$H_3$)$_2$), 25.53 (2C, CH(*C*$H_3$)$_2$), 27.78 (2C, *C*H($CH_3$)$_2$), 62.06 (1C, *C*$H_2$), 121.09 (1C, *C*$H_{Ar}$), 122.97 (1C, *C*$H_{Ar}$), 123.19 (2C, *C*$H_{Ar}$), 123.53 (1C, *C*$H_{Ar}$), 128.06 (2C, *C*$H_{Ar}$), 129.07 (1C, *C*$H_{Ar}$), 136.31 (2C, *C*$_{Ar}$), 138.34 (1C, *C*$H_{Ar}$), 139.21 (1C, *C*$_{Ar}$), 147.59 (2C, *C*$_{Ar}$), 151.90 (1C, *C*$_{Ar}$), 158.03 (1C, *C*$_{Ar}$), 164.88 (1C, *C*$_{Ar}$).

**Homopolymerizations of lactide and ε-caprolactone.** In a typical polymerization run, a magnetically stirred reactor vessel was charged with a solution of monomer in the appropriate solvent, to which the alcohol was eventually added, and then 10 μmol of pyridylamidozinc complex. The alcohol used was either isopropanol (used in the runs performed at room temperature, also because the resonances of the resulting end groups are more clearly detected in the NMR spectra), or less volatile benzyl alcohol (used in the runs performed at higher temperature). The reaction mixture was stirred for the prescribed time at the desired temperature. After a specified time, an aliquot of the crude material was sampled and quenched in wet $CDCl_3$. The sample was subjected to monomer conversion determination, which was monitored by integration of monomer versus polymer in $^1$H-NMR spectrum. The

reaction was terminated by exposing to air and the volatiles were removed under vacuum. The crude product was dissolved in $CH_2Cl_2$ and precipitated in methanol. The obtained polymer was collected by filtration and further dried in a vacuum oven at 60°C for 16 h.

**General procedure for block copolymerizations.** In a glove box, to a $CH_2Cl_2$ solution of the first monomer were added *i*PrOH and $L^2ZnN(SiMe_3)_2$; the reaction mixture was magnetically stirred at room temperature, and the following monomer(s) were sequentially added, maintaining the necessary delay (20-30 min) between each addition. An aliquot of the crude product was sampled and quenched in wet $CDCl_3$ to determine the conversion of each monomer by $^1$H-NMR. The reaction was terminated by exposing to air and the work up of the reaction mixtures were carried out as described above.

**Random copolymerization of L-Lactide and ε-Caprolactone.** A magnetically stirred reactor vessel was charged with L-LA, ε-CL, benzyl alcohol and pyridylamidozinc complex. The reaction mixture was thermostated at 130°C and stirred for 10 minutes. Then the reaction mixture was cooled at room temperature, dissolved in $CH_2Cl_2$ and precipitated in methanol. The precipitated polymer was recovered as described above.

**Kinetic Experiments.** In a glovebox, a magnetically stirred reactor vessel was charged with a solution of L-LA in dichloromethane (3.5 mL, 0.6 M), a solution of *i*PrOH (0.5 mL, 0.02 M) and then a solution of $L^2ZnN(SiMe_3)_2$ (1 mL, 2mM) and then the reaction mixture was immediately stirred. After time intervals of 3 min each, small amounts of the polymerization mixture were transferred in different vials and taken out of the glovebox; each aliquot was withdrawn and quenched with wet $CDCl_3$; the residual amount was quenched by adding an excess of wet *n*-hexane. The fractions were analyzed by $^1$H NMR in $CDCl_3$ to determine the monomer conversion.

**X-ray crystallography.** Yellow prismatic single crystals of compounds $L^1ZnEt$ and $L^3Zn(SiMe_3)_2$ suitable for X-ray diffraction analysis were obtained by slowly

cooling supersaturated hexane solutions. A suitable crystal of $L^1ZnEt$ was selected and mounted on a cryoloop with paratone oil andmeasured at 100 K with a Rigaku AFC7S diffractometer equipped with a Mercury2 CCDdetector using graphite monochromated MoKα radiation (λ = 0.71069 Å). Data reduction was performed with the crystallographic package CrystalClear.1 Data were corrected for Lorentz, polarization and absorption.

A suitable crystal of $L^3Zn(SiMe_3)_2$ was inserted in a 0.4 mm Lindemann and measured at room temperature with a Bruker D8 QUEST diffractometer equipped with a PHOTON100 detector using CuKα radiation (λ= 1.54178 Å). Indexing was performed using APEX3.2 Data integration and reduction were performed using SAINT.2 Absorption correction was performed by multi-scan method in SADABS. For both compounds the structures were solved by Direct Methods using SIR20143 and refined by means of full matrix least-squares based on F2 using the program SHELXL. For both compounds non-hydrogen atoms were refined anisotropically, hydrogen atoms were positioned geometrically and included in structure factors calculations, but not refined. Crystal data and refinement details are reported in Table 3.1. Crystal structures were drawn using OLEX2.5 (Figures 3.3-3.4).

In $L^1ZnEt$ the Zn atom deviates by -0.068(18) Å from the triangle mean plane defined by $N_1$, $N_2$ and $C_{27}$ atoms. In $L^3ZnN(SiMe_3)_2$ the Zn atom deviates by 0.065(14) Å from the triangle mean plane defined by N1, N2 and N3 atoms. Both pyridylamido ligands display an almost perfect planar geometry within a rmsd of 0.0009 Å and 0.043 Å, respectively for $L^1ZnEt$ and $L^3ZnN(SiMe_3)_2$. In both compounds the alkyl substituted aromatic moieties are perpendicular to the bidentate ligand plane. In detail, the isopropyl substituted aromatic moieties are tilted by 86.8(4)° and 79.19(12)°, respectively, while the methyl substituted aromatic moieties are tilted by 74.6(4)° and 62.81(0.12)°, respectively. In both compounds amido nitrogen atoms N1 feature the shortest distances with the zinc atom, 1.867(8) Å and 1.857(2) Å, respectively, while pyridine nitrogen atoms N2 the longest distances with the zinc atom, 2.078(8) Å and 2.146 Å (see Table 3.2).

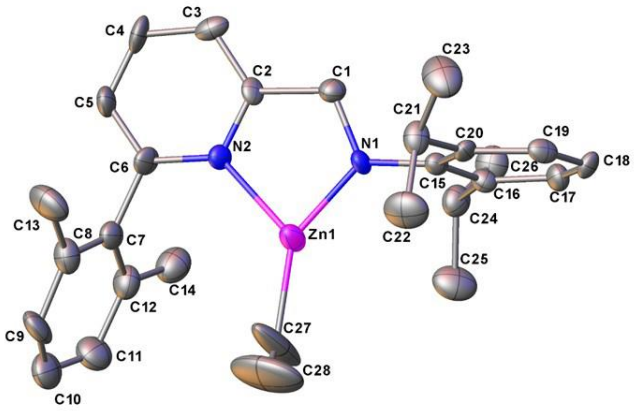


**Figure 3.3.** Ortep drawing of $L^1ZnEt$. Hydrogen atoms have been omitted for clarity. Ellipsoids are drawn at 15% probability level.

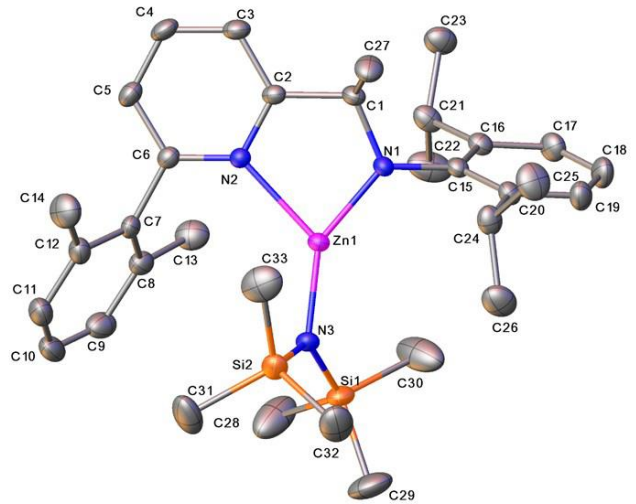


**Figure 3.4.** Ortep drawing of $L^3ZnN(SiMe_3)_2$. Hydrogen atoms have been omitted for clarity. Ellipsoids are drawn at 20% probability level.

**Table 3.1.** Crystallographic data and refinement details for compounds $L^1ZnEt$ and $L^3Zn(SiMe_3)_2$.

| | **$L^1ZnEt$** | **$L^3Zn(SiMe_3)_2$** |
|---|---|---|
| **T (K)** | 100 | 296 |
| **Crystal size (mm x mm x mm)** | 0.44 x 0.32 x 0.27 | 0.55 x 0.36 x 0.26 |
| **Formula** | $C_{28}H_{36}N_2Zn$ | $C_{33}H_{51}N_3Si_2Zn$ |
| **Formula weight** | 465.96 | 611.33 |
| **System** | triclinic | monoclinic |
| **Space group** | $P\bar{1}$ | $P2_1/c$ |
| ***a* (Å)** | 8.671(4) | 13.188(4) |
| ***b* (Å)** | 8.736(3) | 10.266(4) |
| ***c* (Å)** | 19.457(10) | 26.260(16) |
| ***α* (°)** | 78.79(3) | 90 |
| ***β* (°)** | 84.49(4) | 93.00(3) |
| ***γ* (°)** | 67.01(3) | 90 |
| ***V* (Å$^3$)** | 1330.6(11) | 3550(3) |
| ***Z*** | 2 | 4 |
| ***D*$_x$ (g cm$^{-3}$)** | 1.163 | 1.144 |
| **λ (Å)** | 0.71073 | 1.54178 |
| ***μ* (mm$^{-1}$)** | 0.938 | 1.774 |
| ***F*$_{000}$** | 496 | 1312 |
| ***R*1 (I > 2σI)** | 0.1157 (1535) | 0.0361 (3604) |
| **wR2 (all data)** | 0.4084 (6042) | 0.0989 (4073) |
| **N. of param.** | 286 | 365 |
| **GooF** | 0.994 | 1.035 |
| ***ρ*$_{min}$, *ρ*$_{max}$ (eÅ$^{-3}$)** | -0.425, 0.400 | -0.361, 0.276 |

**Table 3.2.** Selected bond distances (Å) and bond angles (°) for $L^1ZnEt$ and $L^3ZnN(SiMe_3)_2$.

| | $L^1ZnEt$ | | $L^3Zn(SiMe_3)_2$ |
|---|---|---|---|
| Zn1—N1 | 1.867(8) | Zn1—N1 | 1.857(2) |
| Zn1—N2 | 2.078(8) | Zn1—N2 | 2.146(2) |
| Zn1— C27 | 1.99(2) | Zn1—N3 | 1.873(2) |
| N1—Zn1— N2 | 83.7(4) | N1—Zn1—N2 | 83.46(9) |
| N1—Zn1— C27 | 146.4(9) | N1—Zn1—N3 | 145.20(10) |
| C27—Zn1— N2 | 129.5(8) | N3—Zn1—N2 | 130.93(9) |

## 3.3 Results and discussion

### 3.3.1 Ring opening polymerization of lactide

We initially tested $L^1ZnEt$, bearing a bulky 2,6-dimethylphenyl substituent in the *ortho*-pyridine moiety and a 2,6-diisopropylphenyl substituent at the amido N, in the ROP of *rac*-lactide under different conditions (see Table 3.3).

Reaction with 200 equiv of monomer in dichloromethane at 25 °C for 2 h did not afford any polymer (run 1); also, after addition of 1 equiv of isopropanol $L^1ZnEt$ was inactive under the same conditions (run 2). Only under more drastic conditions $L^1ZnEt$ was able to promote the polymerization, converting almost quantitatively 200 equiv of *rac*-LA at 80 °C in toluene in 2 h (run 3), and 500 equiv of *rac*-LA in the melt without solvent at 130 °C in 10 min (run 4). Monomer conversion was monitored by $^1$H-NMR in $C_7D_8$ at 80°C until ca. 90% monomer consumption. Plot of $\ln([L\text{-}LA]_0/[L\text{-}LA]_t)$ (Figure 3.5) versus time is linear, indicating that the polymerization process is first-order in monomer concentration and showing an induction time. The latter is reasonably related to the well-known slow reactivity of Zn-ethyl bond toward monomer insertion[7-11] and to the generation of more reactive species by in situ reaction with protic impurities.

The apparent kinetic constant is (1.87 ± 0.01) $10^{-4}$ $s^{-1}$ and it correlates well with the activity observed in polymerization run 3.

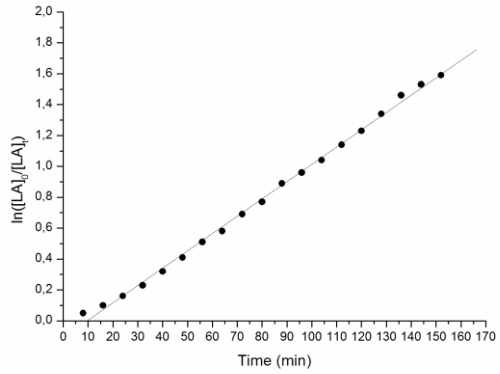


**Figure 3.5.** Pseudo-first-order kinetic plot for ROP of L-LA promoted by **$L^1$ZnEt**: [Zn] = 0.01 M; [L-LA]/[Zn] = 100; T = 80°C; toluene-$d_8$ as solvent.

Since, as just mentioned, the reactivity of Zn-alkyl bonds vs monomer insertion,[7-11] as well as alcoholysis[21] can be slow, we turned to test more reactive Zn-amido complexes. In fact, complex $L^1ZnN(SiMe_3)_2$, bearing the same ligand, gave 25% monomer conversion when tested under the same mild conditions of run 1, and total conversion in 11 min when 1 equiv of isopropanol was added (see runs 5 and 6, respectively). The increase of the polymerization rate after the addition of an alcohol is a feature frequently observed in the literature[8,18,] and it is ascribed to the faster initiation promoted by alkoxy groups with respect to amido moieties.

Complex $L^2ZnN(SiMe_3)_2$, maintaining the same bulky substituent at the amido N, but having a less bulky Me substituent at the pyridine moiety, gave 97% conversion of *rac*-LA in 10 min under the same conditions of run 6 (see run 7). Under these latter conditions, $L^3ZnN(SiMe_3)_2$, maintaining the same bulky substituents of $L^1ZnN(SiMe_3)_2$, but bearing a methyl substituent on the carbon bridging the amido and the pyridine moieties, was only slightly slower (see run 10). Finally, $L^4ZnN(SiMe_3)_2$, having a bulky 2,6-dimethylphenyl substituent at the *ortho*-pyridine

moiety and an electron withdrawing pentafluorophenyl substituent at the amido N, performed similarly to $L^2ZnN(SiMe_3)_2$ (see run 11).

A kinetic study for the polymerization of L-LA by $L^2ZnN(SiMe_3)_2$ and 1 equiv of *i*PrOH was performed by NMR analysis of aliquots of the reaction mixture taken over 3-min intervals. Plot of $\ln([L\text{-}LA]_0/[L\text{-}LA]_t)$ versus time shows a first-order dependence on the concentration of lactide, with an apparent propagation rate constant of $(2.92 \pm 0.01)\ 10^{-4}\ s^{-1}$ at 25 °C (see Figure 3.6).

In summary, the activities of the new Zn complexes in the ROP of *rac*-LA are poorly sensitive to the ligand structure variations, being in all cases in the range of the best performing Zn catalysts reported in the literature.[8,15,21]

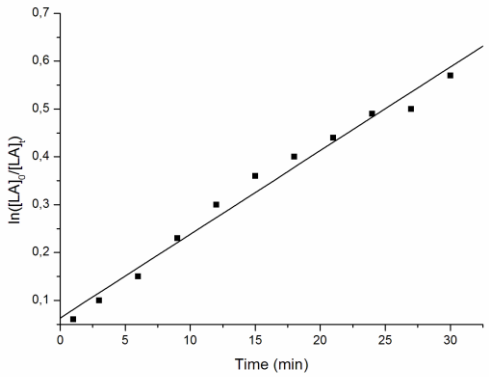


**Figure 3.6.** Pseudo-first-order kinetic plot for ROP of L-LA promoted by $L^2ZnN(SiMe_3)_2$: [Zn] =2 mM; [L-LA]/[Zn]/[*i*PrOH] = 200:1:1; T = 25°C; solvent $CH_2Cl_2$.

Polymerization of either L-LA or D-LA by $L^2ZnN(SiMe_3)_2$ resulted in similar performance to that obtained for *rac*-LA. (cf. runs 7-9). Homonuclear decoupled $^1H$ NMR spectra of the polymers obtained from *rac*-LA in runs 3 and 5-7 indicated that atactic PLA's were produced, while highly isotactic PLLA and PDLA were produced from enantiopure monomers (see runs 8 and 9), as expected if no racemization occurs in the reaction. Since there are literature reports of solvent effects on the stereoselectivity in the ROP of rac-LA,[51,52] we tested $L^2ZnN(SiMe_3)_2$ and $L^3ZnN(SiMe_3)_2$ in THF: while we observed a slower polymerization rate,

reasonably owing to the more coordinating solvent, we did not observe any effect on the polymer stereochemistry (see runs 12 and 13). We also tested $L^3ZnN(SiMe_3)_2$ in toluene: while at 25 °C the polymerization rate was slower than in methylene chloride (200 equiv of rac-LA were converted in 30 min, see run 14), possibly also owing to monomer poor solubility, at 50 °C $L^3ZnN(SiMe_3)_2$ converted 500 equivalents of L-LA in 20 min (run 15), while using 1000 equivalents resulted in 90% conversion in the same time (run 16). Some polymerization tests were also performed at 130 °C without solvent in melt monomer (runs 17-19): $L^2ZnN(SiMe_3)_2$ converted almost quantitatively 500 equivalents of L-LA in 10 min both without alcohol and in the presence of 1 equiv of benzyl alcohol, and 800 equivalents in 30 min without alcohol. SEC analysis of the polymer samples showed a good agreement between the measured and the theoretical molecular weights (see Table 3.3), indicating a well-controlled polymerization and narrow polydispersities for the runs performed in solution, especially when 1 equiv of alcohol was added: in fact, using a 200:1:1 monomer : Zn : alcohol ratio, $M_n$ of ca. 30 kDa were measured, as expected (see runs 6-11). In contrast, polymerizations in neat melt monomer at 130 °C appear to be less controlled: although $L^1ZnEt$ converted almost 500 equiv of LA without added alcohol yielding a $M_n$ of 54 kDa (close to the calculated one, see run 4), $L^2ZnN(SiMe_3)_2$ afforded significantly lower measured $M_n$'s than theoretical ones, both in the presence and in the absence of alcohol (see runs 17-19).

MALDI-ToF MS analysis of a low MW polymer sample prepared in methylene chloride at 25 °C in the presence of 1 equiv of *i*PrOH (Figure 3.7) showed a major population of linear oligomers of structure $H\text{-}[OCH(CH_3)CO]_n\text{-}OCH(CH_3)_2$ with peaks separated by 144 Da. On the contrary, MS analysis of a sample produced in the melt at 130 °C (run 18) showed that the low-molecular weight fraction (which is the only fraction that MALDI-ToF can measure) mainly consists of macrocyclic PLA: the formation of the latter has been ascribed[53] to backbiting intramolecular transesterification reactions, as confirmed by the presence of odd-membered oligomers, with peaks separated by 72 Da (see Figure 3.8).

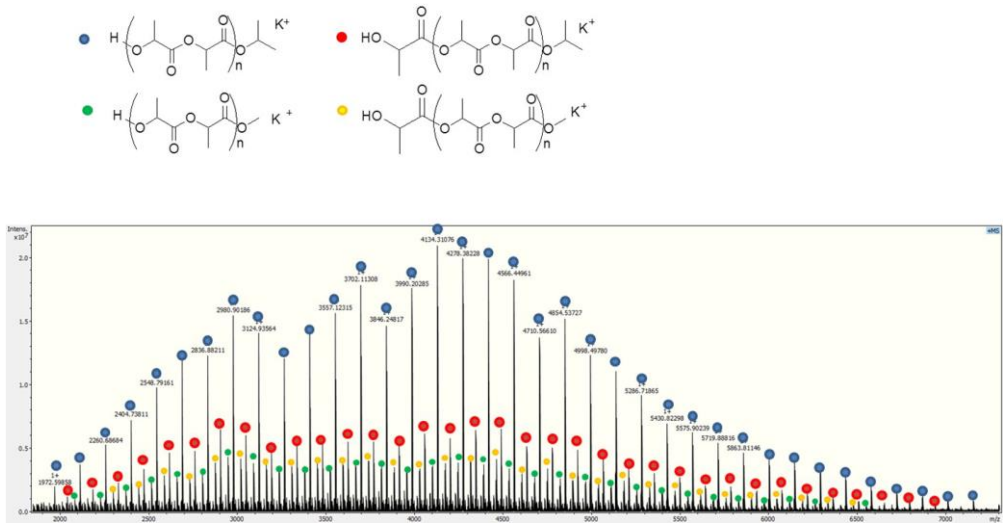

**Figure 3.7.** MALDI-TOF mass spectrum (doped with $K^+$) of a low molecular weight PLA sample prepared using $L^2ZnN(SiMe_3)_2$ / *i*PrOH 1:1, in dichloromethane at 25°C.

However, the $^1H$ NMR spectrum (Figure 3.9) of the same sample displays the resonance at $\delta$ 4.35 ppm for HOCHMe end groups: the molecular weight calculated from the ratio between the resonance of the methine protons and that of the mentioned end groups is close to the $M_n$ measured by SEC, suggesting that backbiting is only a minor reaction pathway leading to the formation of a little fraction of macrocyclic oligomers.

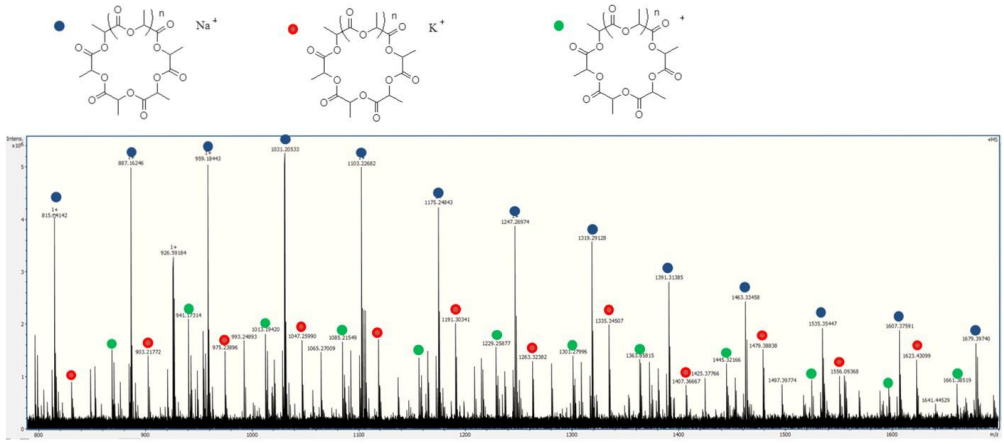

**Figure 3.8.** MALDI-TOF mass spectrum of low-molecular weight fraction of PLA sample (run 18, Table 3.3) in the m/z range: 750 – 1700. Blue circle labelled series calculated for $[(C_3H_4O_2)_n + (C_3H_4O_2)_5 + Na]^+$; red circle labelled series calculated for $[(C_3H_4O_2)_n + [(C_3H_4O_2)_5 + K]^+$ and green circle labelled series calculated for $[(C_3H_4O_2)_n + [(C_3H_4O_2)_5]^+$, with n between 6 and 18 units.

.

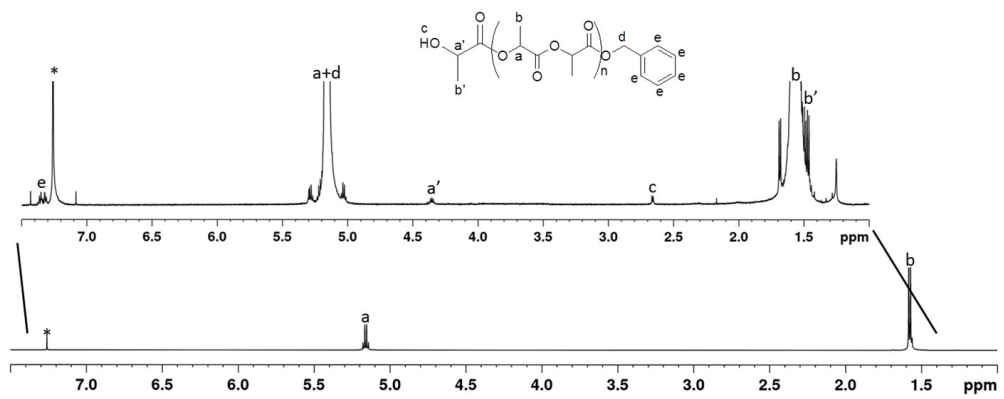


**Figure 3.9.** $^1$H-NMR ($CDCl_3$, 400 MHz, 298 K) of PLA sample obtained in run 18 of Table 3.3 (* stands for residual solvent resonances).

**Table 3.3.** Homopolymerizations of LA.[a]

| Run | Catalyst | monomer | $[ROH]_0/[Zn]_0$ | Solvent | T [°C] | time [min] | Conv[b] | $M_{n,GPC}$[c] [kDa] | $M_{n,theo}$[d] [kDa] | $M_w/M_n$[c] |
|---|---|---|---|---|---|---|---|---|---|---|
| 1 | $L^1ZnEt$ | *rac*-LA | 0 | $CH_2Cl_2$ | 25 | 120 | 0 | | | |
| 2 | $L^1ZnEt$ | *rac*-LA | 1 | $CH_2Cl_2$ | 25 | 120 | 0 | | | |
| 3 | $L^1ZnEt$ | *rac*-LA | 0 | toluene | 80 | 120 | 98 | 19.5 | 28.2 | 1.38 |
| 4[e] | $L^1ZnEt$ | L-LA | 0 | - | 130 | <10 | 92 | 54.1 | 66.3 | 1.31 |
| 5 | $L^1ZnN(SiMe_3)_2$ | *rac*-LA | 0 | $CH_2Cl_2$ | 25 | 120 | 25 | 26.4 | 7.2 | 1.50 |
| 6 | $L^1ZnN(SiMe_3)_2$ | *rac*-LA | 1 | $CH_2Cl_2$ | 25 | 11 | 99 | 27.0 | 28.8 | 1.32 |
| 7 | $L^2ZnN(SiMe_3)_2$ | *rac*-LA | 1 | $CH_2Cl_2$ | 25 | 10 | 97 | 28.2 | 28.0 | 1.25 |
| 8 | $L^2ZnN(SiMe_3)_2$ | D-LA | 1 | $CH_2Cl_2$ | 25 | 10 | 97 | 32.8 | 28.0 | 1.08 |
| 9 | $L^2ZnN(SiMe_3)_2$ | L-LA | 1 | $CH_2Cl_2$ | 25 | 10 | 97 | 35.4 | 28.0 | 1.21 |
| 10 | $L^3ZnN(SiMe_3)_2$ | *rac*-LA | 1 | $CH_2Cl_2$ | 25 | 10 | 94 | 30.2 | 27.1 | 1.21 |
| 11 | $L^4ZnN(SiMe_3)_2$ | L-LA | 1 | $CH_2Cl_2$ | 25 | 10 | 97 | 25.1 | 28.0 | 1.08 |
| 12 | $L^2ZnN(SiMe_3)_2$ | *rac*-LA | 1 | THF | 25 | 60 | 83 | 17.8 | 24.0 | 1.24 |
| 13 | $L^3ZnN(SiMe_3)_2$ | *rac*-LA | 1 | THF | 25 | 60 | 97 | 22.0 | 28.0 | 1.35 |
| 14 | $L^3ZnN(SiMe_3)_2$ | *rac*-LA | 1 | toluene | 25 | 30 | 99 | 19.8 | 28.5 | 1.46 |
| 15[e] | $L^3ZnN(SiMe_3)_2$ | L-LA | 1[g] | toluene | 50 | 20 | 99 | 45.0 | 71.3 | 1.30 |
| 16[f] | $L^3ZnN(SiMe_3)_2$ | L-LA | 1[g] | toluene | 50 | 20 | 90 | 22.3 | 129.7 | 1.29 |
| 17[e] | $L^2ZnN(SiMe_3)_2$ | L-LA | 0 | - | 130 | 10 | 99 | 28.9 | 71.3 | 1.37 |
| 18[e] | $L^2ZnN(SiMe_3)_2$ | L-LA | 1[g] | - | 130 | 10 | 96 | 32.1 | 69.1 | 1.34 |
| 19[h] | $L^2ZnN(SiMe_3)_2$ | L-LA | 0 | - | 130 | 30 | 99 | 43.8 | 114.1 | 1.39 |

[a]Excepting where differently specified, reactions were performed in 2 mL of solvent, $[Zn]_0$ = 5 mM, with $[LA]_0/[Zn]_0$ = 200; ROH = isopropanol. [b]Conversion of monomer as determined by $^1H$ NMR spectral data. [c]Experimental $M_n$ and $M_w/M_n$ values determined by SEC in THF against polystyrene standards, using the correction factor 0.58. [d] Calculated $M_n$ of PLA (in g $mol^{-1}$) = 144.14 × ([LA]/[Zn]) × conversion of LA. [e]$[LA]_0/[Zn]_0$ = 500. [f]$[LA]_0/[Zn]_0$ = 1000. [g]ROH = benzyl alcohol. [h]$[LA]_0/[Zn]_0$ = 800.

### 3.3.2 Ring opening polymerization of ε-caprolactone

Subsequently, the four $L^xZnN(SiMe_3)_2$ complexes (x = 1-4) were tested in the ROP of ε-caprolactone under the conditions (25 °C, [ε-CL]/[Zn]/[*i*PrOH] = 200/1/1, 10 min) which had allowed full conversion of LA. At variance with the results of LA polymerizations, the performances of the four catalysts were significantly different (see Table 3.4): while the complexes bearing the bulkier $L^1$ and $L^3$ ligands afford high monomer conversions, the complex bearing the less bulky $L^2$ was less active. For the latter complex, a polymerization run was performed in toluene at 100 °C with 400 equiv of CL, resulting in almost complete conversion in 7 min, addressing the effect of the reaction temperature (see run 22, Table 3.4).

Finally, the complex bearing the less bulky and electron-withdrawing $L^4$ was only marginally active under mild conditions and short reaction times. However, using a longer reaction time (60 min) 80% monomer conversion was achieved, pointing to a possible induction period. As a matter of fact, as previously reported,[50] $L^4ZnN(SiMe_3)_2$ is involved in a slow Schlenk-type equilibrium between the heteroleptic and the homoleptic bis(chelate) complexes: it is possible that the position of the equilibrium is affected by the coordination ability of the monomer.

**Table 3.4**. Homopolymerizations of ε-CL.[a]

| Run | Catalyst | Conv[b] [%] | $M_{n,GPC}$[c] [kDa] | $M_{n,theo}$[d] [kDa] | $M_w/M_n$[c] [kDa] |
|---|---|---|---|---|---|
| 20 | $L^1ZnN(SiMe_3)_2$ | 94 | 30.6 | 21.5 | 1.11 |
| 21 | $L^2ZnN(SiMe_3)_2$ | 35 | 11.4 | 8.0 | 1.13 |
| 22[e] | $L^2ZnN(SiMe_3)_2$ | 99 | 39.3 | 45.2 | 1.32 |
| 23 | $L^3ZnN(SiMe_3)_2$ | 81 | 28.2 | 18.5 | 1.16 |
| 24 | $L^4ZnN(SiMe_3)_2$ | 2 | - | - | - |
| 25 | $L^4ZnN(SiMe_3)_2$ | 83[f] | 17.5 | 19.0 | 1.03 |

[a]Polymerization runs were performed in $CH_2Cl_2$ [2 mL] at 25°C employing 10 μmmol of catalyst with [ε-CL]/[Zn]/[*i*PrOH] = 200/1/1, time 10 min. [b]Conversion of ε-CL as determined by $^1H$ NMR spectral data. [c]Experimental $M_n$ [in g $mol^{-1}$] and $M_w/M_n$ values determined by SEC in THF against polystyrene standards, using the correction factor 0.56.[d]Calculated $M_n$ of PCL (in g $mol^{-1}$) = 114.14 × ([CL]/[Zn]) × conversion of CL. [e]Polymerization run was performed in toluene at 100°C with [ε-CL]/[Zn]/[*i*PrOH]= 400/1/1, time 7 min.[f] Polymerization time 60 min.

### 3.3.3 Block copolymerization of L-LA, D-LA, *rac*-LA and CL by sequential monomer addition

In view of the controlled nature and high rate of the polymerization promoted by our new pyridylamido Zn(II) catalysts, we targeted the synthesis of stereoblock copolymers by sequential addition of L-LA, D-LA and *rac*-LA (see Scheme 3.2).

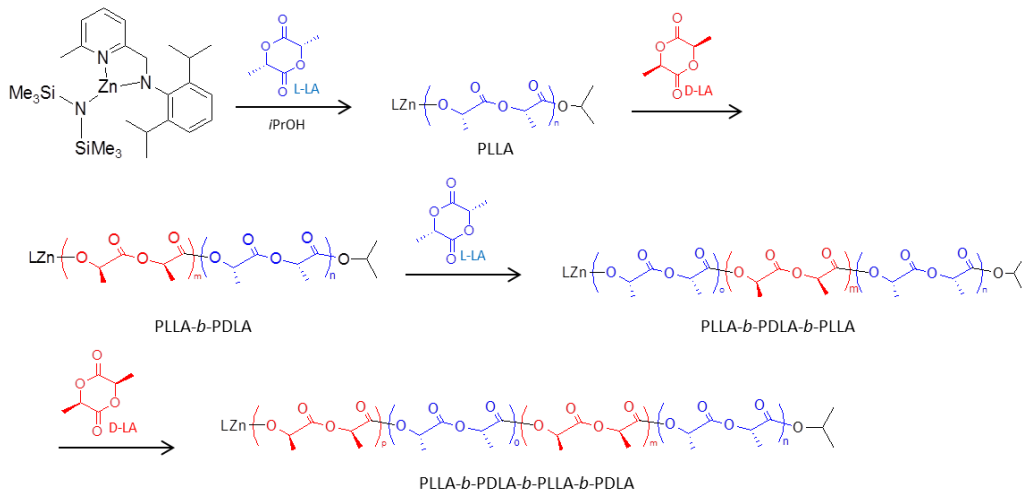


**Scheme 3.2.** One-pot synthesis of stereoblock PLA's.

Thus, a diblock copolymer was synthesized by allowing to react 10 μmol of $L^2ZnN(SiMe_3)_2$, 1 equiv of isopropanol and 100 equiv of L-LA at 25 °C in $CH_2Cl_2$ for 20 min, and then adding 100 equiv of D-LA continuing the polymerization for further 20 min (see Table 3.5, run 26). $^1H$ and $^{13}C$ NMR analysis confirmed the production of a highly isotactic copolymer, according to literature assignments[25,39] ($P_m$ > 98%, see Figures 3.10 and 3.11).

SEC analysis performed after the formation of each block confirmed the synthesis of a diblock copolymer (see Figure 3.12), although, some tailing effects suggest contamination by some low-MW minor fractions, possibly due to the presence of protic impurities in the reaction medium.

Finally, DSC analysis indicated that the stereodiblock copolymer crystallizes in the stereocomplex form, with a $T_m$ = 209 °C in the first heating, followed by recrystallization and a $T_m$ = 202 °C in the second heating run (see Figures 3.13 – 3.14).

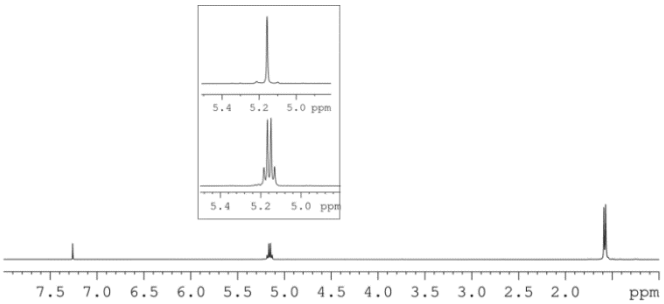


**Figure 3.10.** $^{1}$H-NMR and HD-NMR (square) ($CDCl_3$, 600MHz) of L100-*b*-D100 diblock PLA copolymer sample (run 26, Table 3.3).

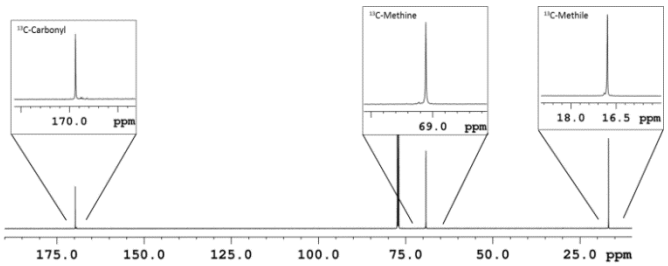


**Figure 3.11.** $^{13}$C-NMR ($CDCl_3$, 150MHz) of L100-*b*-D100 diblock PLA copolymer sample (run 26, Table 3.4).

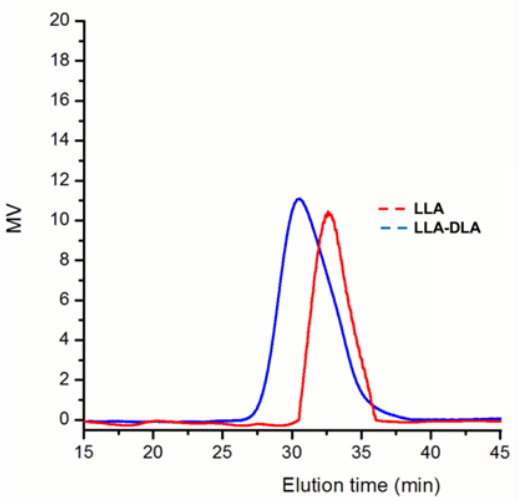


**Figure 3.12.** SEC profiles for diblock poly(LLA-*b*-DLA) in run 26 of Table 3.5

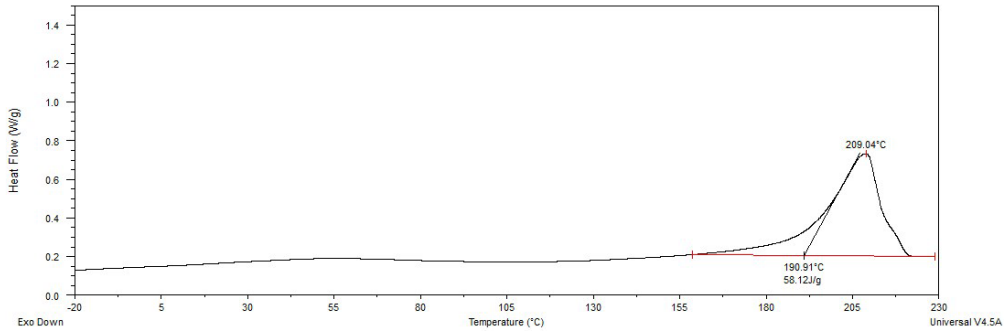


**Figure 3.13.** Thermogram of first DSC heating run of diblock copolymer LLA-*b*-DLA, 100-*b*-100, run 26, Table 3.5.

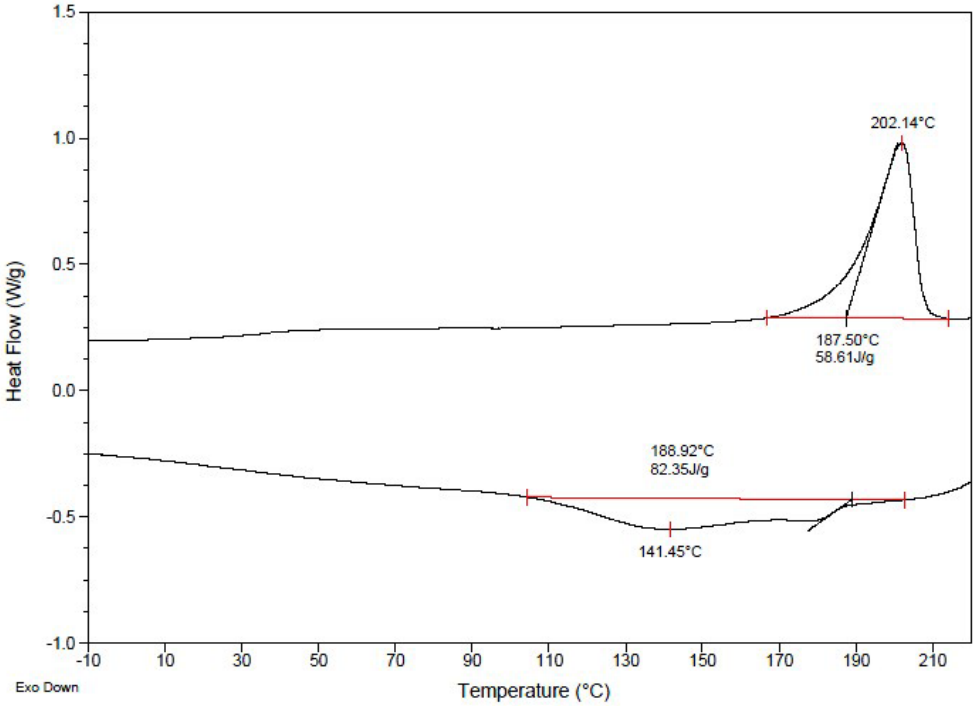


**Figure 3.14.** Thermograms of second DSC heating (up) and cooling (bottom) run of diblock copolymer LLA-*b*-DLA, 100-*b*-100, run 26, Table 3.5.

A diblock poly(LLA-*b*-DLA) having longer L-LA and D-LA sequences was synthesised similarly by sequential addition of 200 equivalents of the monomers over a 1 h total reactive time (Table 3.5, run 27).

A triblock poly(LLA-*b*-DLA-*b*-LLA) was prepared similarly (Table 3.5, run 28) by sequential additions of 100 equiv of the proper monomer in each step over 20 min-each intervals, in order to ensure full conversion. NMR analysis again showed a stereoregular blocks composition, SEC analysis confirmed the increase of MW over each monomer addition (see Figure 3.15).

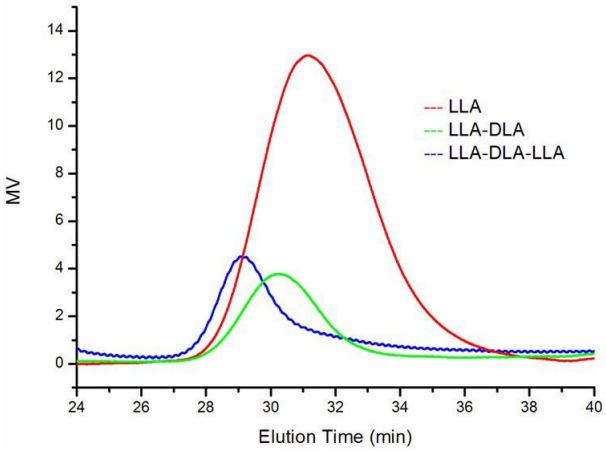


**Figure 3.15**. SEC profiles of triblock copolymer LLA-*b*-DLA-*b*-LLA, run 28, Table 3.5.

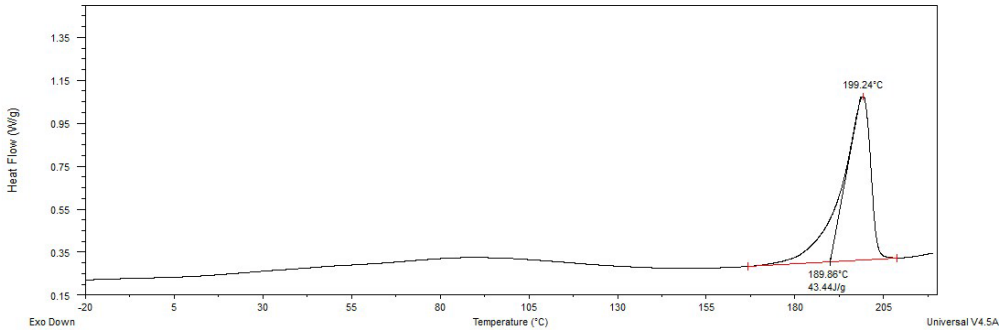


**Figure 3.16.** Thermogram of first DSC heating run of triblock copolymer LLA-*b*-DLA-*b*-LLA, run 28, Table 3.5.

and DSC analysis confirmed the production of a stereocomplex phase ($T_m$ = 199 °C, Figure 3.16). The lower melting temperature and melting enthalpy observed with respect to the diblock copolymer can be ascribed to the inequivalent amounts of the sequences of L-LA and D-LA, the latter being one half of the former.

A triblock poly(LLA-*b*-DLLA-*b*-DLA), containing two crystalline end blocks of isotactic PLA's with opposite chirality and an amorphous midblock of atactic PLA, was also prepared (Table 3.5, run 29) by a similar procedure.[38] A stereocomplex phase of the two crystalline end blocks was evidenced by DSC analysis ($T_m$ = 205°C, Figure 3.17).

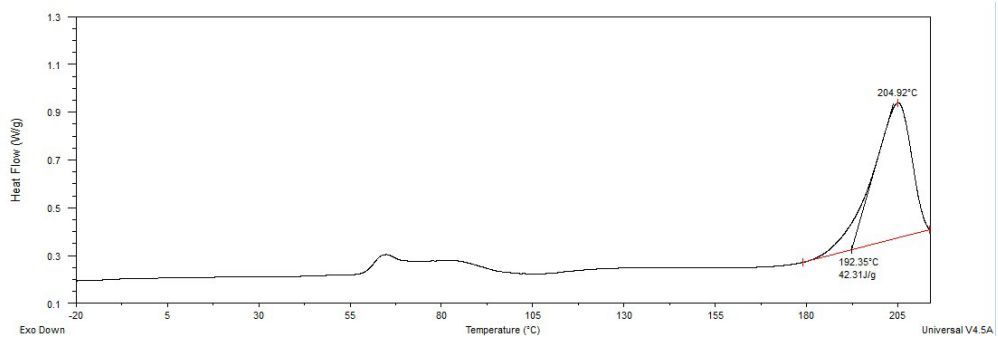


**Figure 3.17.** Thermogram of first DSC heating run of triblock copolymer LLA-*b*-DLLA-*b*-DLA, run 29, Table 3.5.

Interestingly, the melting temperature of this sample is higher than that of the previous one, probably because here there are equivalent amounts of the sequences of L-LA and D-LA, spanned by an amorphous block of *rac*-lactide (SEC profiles reported in Figure 3.18). NMR analysis confirms the presence of both the isotactic and the atactic blocks (see Figure 3.19). A stereotetrablock PLLA-*b*-PDLA-*b*-PLLA-*b*-PDLA was also prepared with the same procedure (Table 3.5, run 30): also in this case the stereocomplex phase was produced ($T_m$ = 191 °C, Figure 3.20). The lower melting temperature and melting enthalpy are ascribed to the fact that the stereoregular block integrity was only partially preserved, as indicated by NMR

analysis ($P_m$ = 0.9, Figure 3.21), owing to incomplete monomer conversion during the subsequent steps.

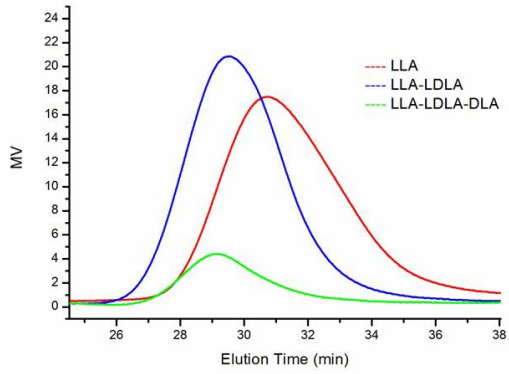


**Figure 3.18.** SEC profiles of triblock copolymer LLA-DLLA-DLA, 100-*b*-100-*b*-100 in run 29 of Table 3.5.

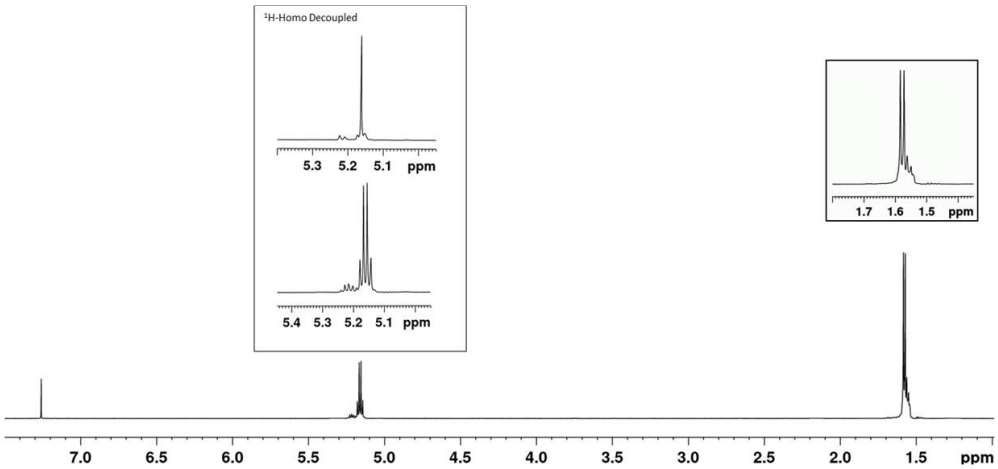


**Figure 3.19.** $^1$H-NMR and HD-NMR ($CDCl_3$, 600MHz) of LLA-DLLA-LLA, 100-*b*-100-*b*-100, triblock PLA copolymer sample (run 29, Table 3.5).

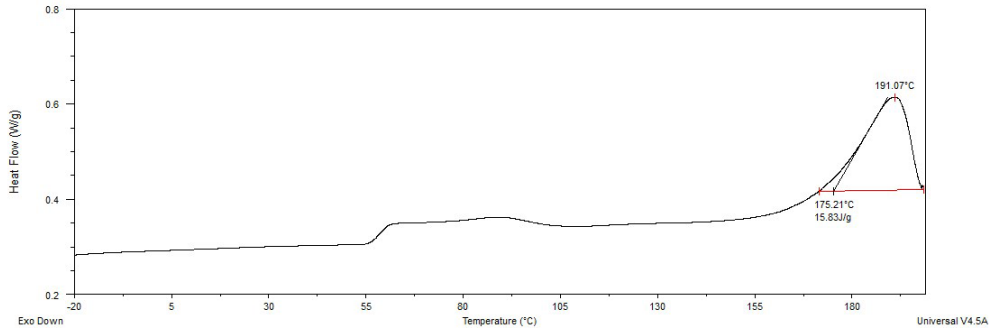


**Figure 3.20.** Thermogram of first DSC heating run of tetrablock copolymer LLA-*b*-DLA-*b*-LLA-*b*-DLA, run 30, Table 3.5.

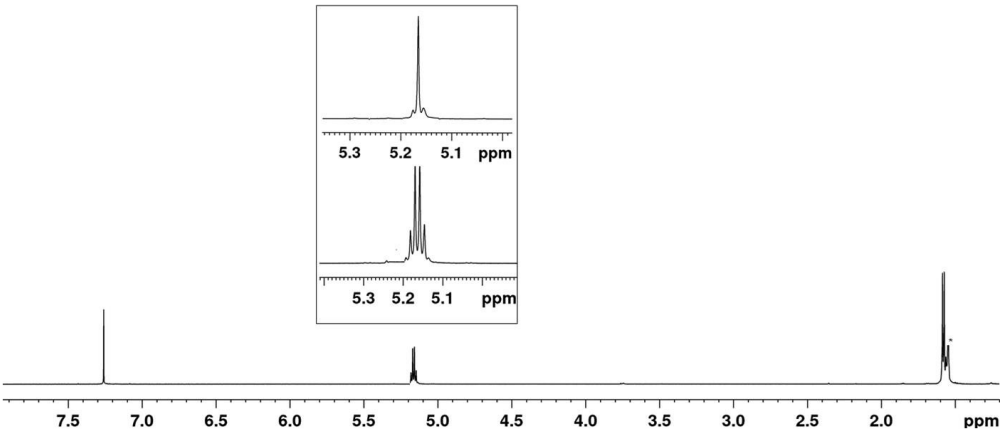


**Figure 3.21.** $^{1}$H-NMR and HD-NMR (square) ($CDCl_3$, 600MHz) of LLA-DLA-LLA-DLA, 100-*b*-100-*b*-100-*b*-100, tetrablock PLA copolymer sample (run 30, Table 3.5), (* stands for residual solvent resonances).

**Table 3.5.** Block copolymerizations of LLA, DLA, DLLA and ε-CL[a].

| Run | copolymer [theoretical block length) | Time[b] [min] | $M_n$[c] [kDa] | $M_w/M_n$[c] | $T_m$[d] [°C] | $\Delta H_m$[d] [$Jg^{-1}$] |
|---|---|---|---|---|---|---|
| 26 | PLLA-*b*-PDLA [100-*b*-100] | 40 | 18.8 | 1.20 | 209 | 58.1 |
| 27 | PLLA-*b*-PDLA [200-*b*-200] | 60 | 41.1 | 1.16 | 215 | 51.3 |
| 28 | PLLA-*b*-PDLA-*b*-PLLA [100-*b*-100-*b*-100] | 60 | 36.8 | 1.11 | 199 | 43.4 |
| 29 | PLLA-*b*-PDLLA-*b*-PDLA [100-*b*-100-*b*-100] | 60 | 34.4 | 1.20 | 205 | 42.3 |
| 30 | PLLA-*b*-PDLA-*b*-PLLA-*b*-PDLA [100-*b*-100-*b*-100-b-100] | 80 | 37.8 | 1.22 | 191 | 15.8 |
| 31 | PCL-*b*-PLLA [200-*b*-200] | 40 | 27.5 | 1.39 | $56_{[PCL]}$ $175_{[PLA]}$ | $19.6_{[PCL]}$ $33.3_{[PLA]}$ |

[a]Polymerizations performed in $CH_2Cl_2$ [2 mL] at 25°C employing 10 μmol of [$L^2ZnN(SiMe_3)_2$] and 1 equiv of *i*PrOH. Full conversion was confirmed by $^1H$ NMR. [b]20−30 min was maintained between each monomer addition, depending on the monomer amount and length of polymer chain. [c]Experimental $M_n$ [in g $mol^{-1}$] and Mw/Mn values determined by SEC in THF against polystyrene standards, using the correction factor 0.58 for lactide and 0.56 for caprolactone. [d]The $T_m$ and $\Delta H_m$ was the melting temperatures and enthalpies during the first heating under a heating rate of 10°C $min^{-1}$

Also block copolymerization of LA and CL was explored. Thus, a run was performed using $L^2ZnN(SiMe_3)_2$, 1 equiv of iPrOH and 200 equiv of CL at 25 °C: full conversion was achieved after 20 min and then 200 equiv of L-LA were added and the reaction was prolonged for additional 20 min, affording a diblock PCL-PLA copolymer (see run 31 of Table 3.5). NMR, DSC and SEC analyses confirmed the formation of the diblock PCL-PLA copolymer (see Figures 3.22 – 3.25).

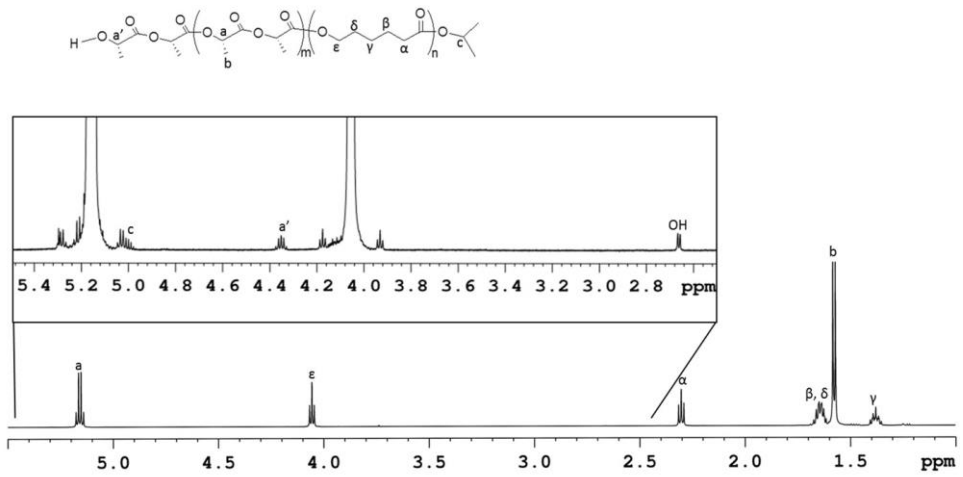


**Figure 3.22.** 1H-NMR ($CDCl_3$, 600MHz) of PCL-LLA, 200-*b*-200, diblock copolymer sample (run 31, Table 3.5).

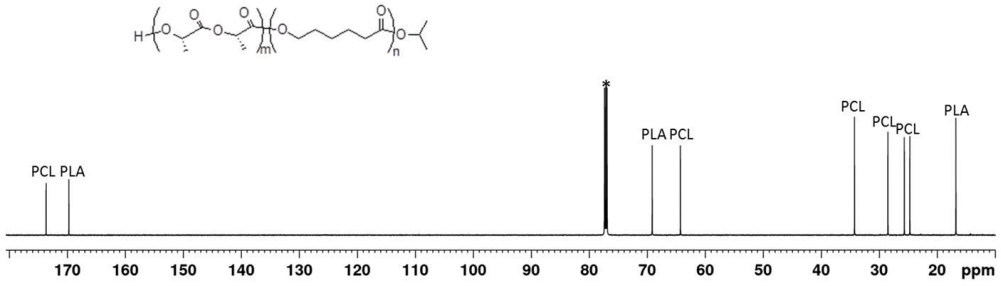


**Figure 3.23.** $^{13}C$-NMR ($CDCl_3$, 150MHz) of PCL-LLA, 200-*b*-200, diblock copolymer sample(run 31, Table 3.5).

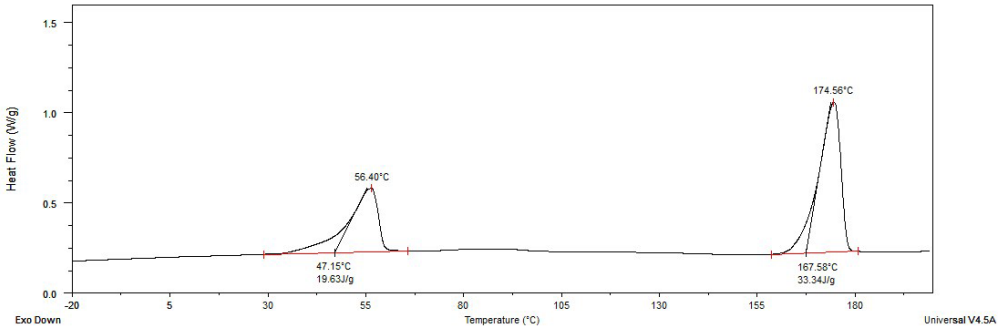


**Figure 3.24.** Thermogram of first DSC heating run of diblock copolymer CL-*b*-LLA, run 31, Table 3.5.

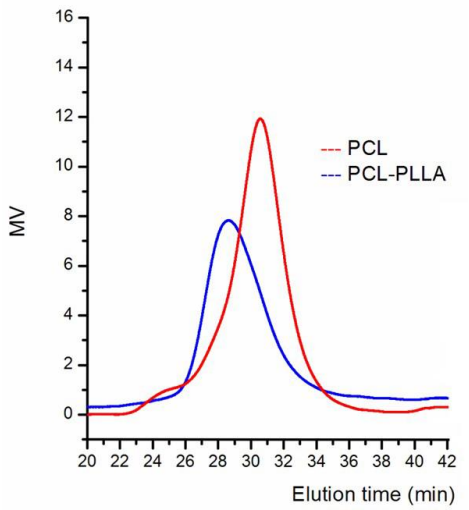


**Figure 3.25.** SEC profiles of diblock copolymerPCL-PLA copolymer in run 31 of Table 3.5.

We also explored the feasibility of the reversed sequence addition of the two monomers: however, after the conversion of 200 equiv of LA under the same reaction conditions, the added CL was not polymerized at all. Accordingly, a polymerization performed under similar conditions, but adding the two monomers at the beginning of the run resulted in the production of PLA homopolymer, with CL remaining unreacted. The importance of the order of monomer addition was addressed in an early work on the matter[28] and the difficulty to achieve polymerization of CL after LA was observed frequently [18,37-41] , although we[30] and Ma et al.[52] have reported catalysts able to produce diblock PLA-PCL copolymers *via* the "PLA first" route. No CL polymerization was observed in the presence of LA even in toluene at 50 °C, while a LA-CL copolymer was obtained at 130 °C in neat monomers: $^{1}H$ and $^{13}C$ NMR analysis of the latter sample indicated that a pseudorandom copolymer was produced owing to extensive transesterifications as indicated by the presence of single lactic acid monomer units ($^{13}C$ resonance of the carbonyl at $\delta$ = 171 ppm) (see Figures 3.26 – 3.27).

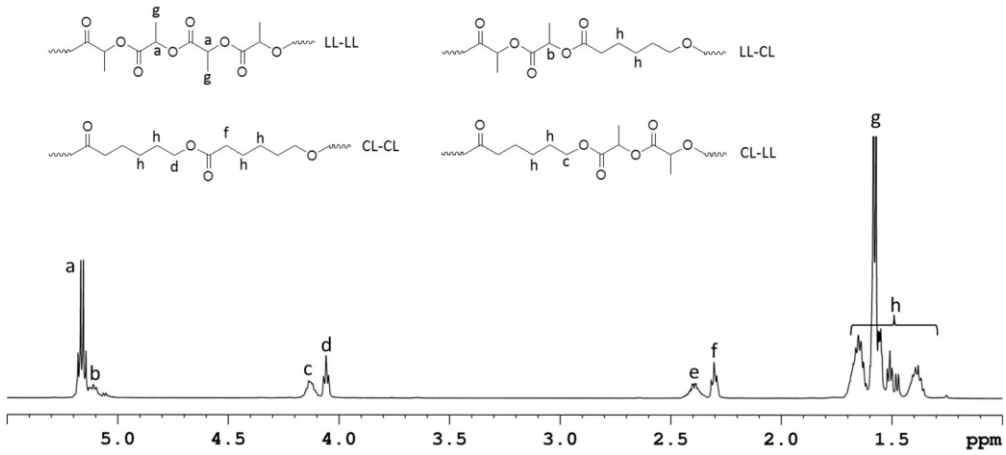


**Figure 3.26**. $^{1}$H-NMR ($CDCl_3$, 600MHz) of a random copolymer sample of CL and LLA.

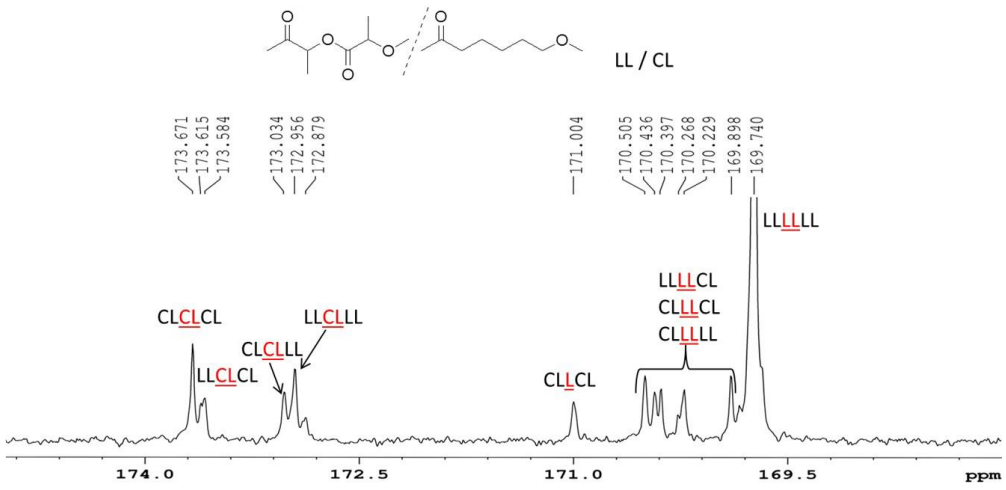


**Figure 3.27.** Carbonyl region of the $^{13}$C NMR (150 MHz, $CDCl_3$) spectrum of a random copolymer sample of CL and LLA.

## 3.4 Conclusions

We have introduced a family of three-coordinated Zn(II) complexes bearing chelating pyridylamido ligands with variable steric and electronic features: these complexes have been tested for the ROP of lactide and ε-caprolactone, resulting in

fast and controlled polymerizations. The latter performances allowed the synthesis of precise stereodiblock, stereotriblock and stereotetrablock copolymers of L-LA, D-LA and *rac*-LA by one-pot sequential addition of the monomers under mild conditions and in short reaction times. In the same way, diblock copolymers of ε-caprolactone and lactide were produced. The reported complexes are the first catalysts based non-toxic and environmentally benign Zn complexes able to produce efficiently "tailor-made" block copolymers by the one-pot sequential addition strategy.[37-41] Future work will be focused on the physical properties of new polymeric materials produced by this strategy, with a particular attention to the synthesis of ABA triblock copolymers behaving as biodegradable thermoplastic elastomers.[22,32-36]

## References


1. Schneiderman, D. K.; Hillmyer, M. A. 50th Anniversary Perspective: There Is a Great Future in Sustainable Polymers, *Macromolecules* **2017**, *50*, 3733-3749.
2. For a recent review of the matter, see, e. g.: Karbalaei, S.; Hanachi, P.; Walker, T. R.; Cole, M. Occurrence, Sources, Human Health Impacts and Mitigation of Microplastic Pollution. *Environ. Sci. Pollut. Res.* **2018**, *25*, 36046–36063.
3. Zhang, X.; Fevre, O.; Jones, J.; Waymouth, R. M. Catalysis as an Enabling Science for Sustainable Polymers. *Chem. Rev*. **2018**, *118*, 839-885.
4. Tschan, M. J. L.; Brulé, E.; Haquette, P.; Thomas, C. M. Synthesis of Biodegradable Polymers from Renewable Resources. *Polymer Chem.* **2012**, *3*, 836.
5. Saeidlou, M.; Huneault, A.; Li, H.; Park, C. B. Poly(lactic acid) Crystallization, *Progr. Polym. Sci.* **2012**, *37*, 1657-1677.
6. Castro-Aguirre, E.; Iniguez-Franco, F.; Samsudin, H.; Fang, X.; Auras, R. Poly(lactic acid)—Mass Production, Processing, Industrial Applications, and End of Life. *Adv. Drug Deliv. Rev.* **2016**, *107*, 333-366.

7. Cheng, M.; Attygalle, A. B.; Lobkovsky, E. B.; Coates, G. W. Single-Site Catalysts for Ring-Opening Polymerization: Synthesis of Heterotactic Poly(lactic acid) from *rac*-Lactide. *J. Am. Chem. Soc.* **1999**, *121*, 11583–11584.
8. Chamberlain, B. M.; Cheng, M.; Moore, D. R.; Ovitt, T. M.; Lobkovsky, E. B.; Coates, G. W. Polymerization of Lactide with Zinc and Magnesium β-Diiminate Complexes: Stereocontrol and Mechanism. *J. Am. Chem. Soc*. **2001**, *123*, 3229–3238.
9. Dove, A.; Gibson, V.; Marshall, E.; White, A.; Williams, D. Magnesium and Zinc Complexes of a Potentially Tridentate β-Diketiminate Ligand. *Dalton Trans*. **2004**, 570-578.
10. Ayala, N.; Chisholm, M. H.; Gallucci, J. C.; Krempner, C. Chemistry of BDI*M(2+) Complexes (M = Mg, Zn) and Their Role in Lactide Polymerization where BDI* is the Anion Derived from Methylenebis(C-$^{t}$Bu, N-2,6-Diisopropylphenyl)ImineBDI*H. *Dalton Trans*. **2009,** 9237.
11. Keram, M.; Ma, H. Ring-Opening Polymerization of Lactide, ε-Caprolactone and their Copolymerization Catalyzed by β-Diketiminate Zinc Complexes. *Appl. Organometal. Chem.* **2017**, *31*:e3893.
12. Chisholm, M. H.; Eilerts, N. W.; Huffman, J. C.; Iyer, S. S.; Pacold, M.; Phomphrai, K. Molecular Design of Single-Site Metal Alkoxide Catalyst Precursors for Ring-Opening Polymerization Reactions Leading to Polyoxygenates. 1. Polylactide Formation by Achiral and Chiral Magnesium and Zinc Alkoxides, ($\eta^3$-L)MOR, Where L = Trispyrazolyl- and Trisindazolylborate Ligands. *J. Am. Chem. Soc.* **2000**, *122*, 11845–11854.
13. Fliedel, C.; Mameri, S.; Dagorne, S.; Aviles, T. Controlled Ring-Opening Polymerization of Trimethylene Carbonate and Access to PTMC-PLA Block Copolymers Mediated by Well-Defined N-Heterocyclic Carbene Zinc Alkoxides. *Appl. Organomet. Chem.* **2014**, *28*, 504–511.
14. Fliedel, C.; Vila-Vicosa, D.; Calhorda, M. J.; Dagorne, S.; Aviles, T. Inside Back Cover: Dinuclear Zinc–N-Heterocyclic Carbene Complexes for Either the

Controlled Ring-Opening Polymerization of Lactide or the Controlled Degradation of Polylactide Under Mild Conditions. *Chem. Cat. Chem.* **2014**, *6*, 1357–1367.

15. Williams, C. K.; Breyfogle, L. E.; Choi, S. K.; Nam, W.; Young Jr., V. G.; Hillmyer, M. A.; Tolman, W. B. A Highly Active Zinc Catalyst for the Controlled Polymerization of Lactide. *J. Am. Chem. Soc.* **2003**, *125*, 11350–11359.
16. Poirier, V.; Roisnel, T.; Carpentier, J.-F.; Sarazin, Y. Versatile Catalytic Systems Based on Complexes of Zinc, Magnesium and Calcium Supported by a Bulky Bis(morpholinomethyl)phenoxy Ligand for the Large-Scale Immortal Ring-Opening Polymerisation of Cyclic Esters. *Dalton Trans.* **2009**, 9820–9827.
17. Wang, L.; Ma, H. Highly Active Magnesium Initiators for Ring-Opening Polymerization of *rac*-Lactide. *Macromolecules* **2010**, *43*, 6535–6537.
18. Pilone, A.; Lamberti, M.; Mazzeo, M.; Milione, S.; Pellecchia, C. Ring-opening Polymerization of Cyclic Esters by Phenoxy-Thioether Complexes Derived from Biocompatible Metal. *Dalton Trans.* **2013**, *42*, 13036–13047.
19. Fliedel, C.; Rosa, F. M.; Alves, A.; Martins, M.; Aviles, T.; Dagorne, S. P,O-Phosphinophenolate Zinc(II) Species: Synthesis, Structure and Use in the Ring-Opening Polymerization (ROP) of Lactide, ε-Caprolactone and Trimethylene Carbonate. *Dalton Trans.* **2015**, *44*, 12376–12387.
20. Pilone, A.; De Maio, N.; Press, K.; Venditto, V.; Pappalardo, D.; Mazzeo, M.; Pellecchia, C.; Kol, M.; Lamberti, M. Ring-Opening Homo- and co-Polymerization of Lactides and ε-Caprolactone by Salalen Aluminum Complexes. *Dalton Trans.* **2015**, *44*, 2157-2165.
21. Rosen, T.; Popowski, Y.; Goldberg, I.; Kol, M. Zinc Complexes of Sequential Tetradentate Monoanionic Ligands in the Isoselective Polymerization of rac-Lactide, *Chem. Eur. J.* **2016**, *22*, 11533-11536.
22. Hillmyer, M. A.; Tolman, W. B. Aliphatic Polyester Block Polymers: Renewable, Degradable, and Sustainable. *Acc. Chem. Res.* **2014**, *47*, 2390-2396.

23. Ikada, Y.; Jamshidi, K.; Tsuji, H.; Hyon, S. H. Stereocomplex Formation Between Enantiomeric Poly(lactides). *Macromolecules* **1987**, *20*, 904–906.
24. Spassky, N.; Wisniewski, M.; Pluta, C.; Le Borgne, A. Highly Stereoelective Polymerization of rac-(D,L)-Lactide with a Chiral Schiff's Base/Aluminium Alkoxide Initiator. *Macromol. Chem. Phys.* **1996**, *197*, 2627–2637.
25. Ovitt, T. M.; Coates, G. W. Stereochemistry of Lactide Polymerization with Chiral Catalysts: New Opportunities for Stereocontrol Using Polymer Exchange Mechanisms. *J. Am. Chem. Soc.* **2002**, *124*, 1316-1326.
26. Zhong, Z.; Dijkstra, P. J.; Feijen, J. Controlled and Stereoselective Polymerization of Lactide: Kinetics, Selectivity, and Microstructures. *J. Am. Chem. Soc.* **2003**, *125*, 11291–11298.
27. Nomura, N.; Ishii, R.; Yamamoto, Y.; Kondo, T. Stereoselective Ring-Opening Polymerization of a Racemic Lactide by Using Achiral Salen– and Homosalen–Aluminum Complexes. *Chem. Eur. J.* **2007**, *13*, 4433–4451.
28. Jacobs, P.; Dubois, R.; Jerome, P.; Teyssie, M. Macromolecular Engineering of Polylactones and Polylactides. 5. Synthesis and Characterization of Diblock Copolymers Based on Poly-ε-caprolactone and Poly(L,L or D,L)lactide by Aluminum Alkoxides. *Macromolecules* **1991**, *24*, 3027-3034.
29. Amgoune, C.; Thomas, M.; Roisnel, T.; Carpentier, J.-F. Ring-Opening Polymerization of Lactide with Group 3 Metal Complexes Supported by Dianionic Alkoxy-Amino-Bisphenolate Ligands: Combining High Activity, Productivity, and Selectivity. *Chem. Eur. J.* **2006**, *12*, 169–179.
30. Pappalardo, D.; Annunziata, L.; Pellecchia, C. Living Ring-Opening Homo- and Copolymerization of ε-Caprolactone and L-and D,L-Lactides by Dimethyl(salicylaldiminato)aluminum Compounds. *Macromolecules* **2009**, *42*, 6056-6062.
31. Ebrahimi, T.; Aluthge, D. C.; Patrick, B. O.; Hatzikiriakos, S. G.; Mehrkhodavandi, P. Air- and Moisture-Stable Indium Salan Catalysts for Living Multiblock PLA Formation in Air. *ACS Catal.* **2017**, *7*, 6413–6418.

32. Ryner, M.; Albertsson, A.-C. Resorbable and Highly Elastic Block Copolymers from 1,5-Dioxepan-2-one and l-Lactide with Controlled Tensile Properties and Hydrophilicity. *Biomacromolecules* **2002**, *3*, 601–608.
33. Zhang, Z.; Grijpma, D. W.; Feijen, J. Triblock Copolymers Based on 1,3-Trimethylene Carbonate and Lactide as Biodegradable Thermoplastic Elastomers. *Macromol. Chem. Phys.* **2004**, *205*, 867–875.
34. Lin, J. O.; Chen, W.; Shen, Z.; Ling, J. Homo- and Block Copolymerizations of ε-Decalactone with L-Lactide Catalyzed by Lanthanum Compounds. *Macromolecules* **2013**, *46*, 7769–7776.
35. Nakayama, Y.; Aihara, K.; Yamanishi, H.; Fukuoka, H.; Tanaka, R.; Cai, Z. T.; Shiono, T. Synthesis of Biodegradable Thermoplastic Elastomers from ε-Caprolactone and Lactide. *J. Polym. Sci. A: Polym. Chem.* **2015**, *53*, 489–495.
36. Schneiderman, K.; Hill, E. M.; Martello, M. T.; Hillmyer, M. A. Poly(lactide)-Block-poly(ε-caprolactone-co-ε-decalactone)-block-poly(lactide) Copolymer Elastomers. *Polym. Chem.* **2015**, *6*, 3641-3651.
37. Othman, N.; Xu, C.; Mehrkhodavandi, P.; Hatzikiriakos, S. G. Thermorheological and Mechanical Behavior of Polylactide and its Enantiomeric Diblock Copolymers and Blends. *Polymer* **2012**, *53*, 2442−2452.
38. Aluthge, C.; Xu, C.; Othman, N.; Noroozi, N.; Hatzikiriakos, S. G.; Mehrkhodavandi, P. PLA–PHB–PLA Triblock Copolymers: Synthesis by Sequential Addition and Investigation of Mechanical and Rheological Properties. *Macromolecules* **2013**, *46*, 3965–3974.
39. Rosen, T.; Goldberg, I.; Venditto, V.; Kol, M. Tailor-Made Stereoblock Copolymers of Poly(lactic acid) by a Truly Living Polymerization Catalyst. *J. Am. Chem. Soc.* **2016**, *138*, 12041-12044.
40. Rosen, T.; Goldberg, I.; Navarra, W.; Venditto, V.; Kol, M. Divergent [{ONNN}Mg–Cl] Complexes in Highly Active and Living Lactide Polymerization. *Chem. Sci.* **2017**, *8*, 5476–5481.

41. Rosen, T.; Goldberg, I.; Navarra, W.; Venditto, V.; Kol, M. Block–Stereoblock Copolymers of Poly(ε-Caprolactone) and Poly(lactic acid). *Angew. Chem.* **2018**, *130*, 7309-7313.
42. Annunziata, L.; Pappalardo, D.; Tedesco, C.; Pellecchia, C. Isotactic-Specific Polymerization of Propene by a $C_s$-Symmetric Zirconium(IV) Complex Bearing a Dianionic Tridentate [¯NNN¯] Amidomethylpyrrolidepyridine Ligand. *Macromolecules* **2009**, *42*, 5572– 5578.
43. Li, G.; Lamberti, M.; D'Amora, S.; Pellecchia, C. $C_1$-Symmetric Pentacoordinate Anilidopyridylpyrrolide Zirconium(IV) Complexes as Highly Isospecific Olefin Polymerization Catalysts. *Macromolecules* **2010**, *43*, 8887–8891.
44. Annunziata, L.; Pragliola, S.; Pappalardo, D.; Tedesco, C.; Pellecchia, C. New (Anilidomethyl)pyridine Titanium(IV) and Zirconium(IV) Catalyst Precursors for the Highly Chemo- and Stereoselective cis-1,4-Polymerization of 1,3-Butadiene. *Macromolecules* **2011**, *44*, 1934–1941.
45. Li, G.; Zuccaccia, C.; Tedesco, C.; D'Auria, I.; Macchioni, A.; Pellecchia, C. NMR Spectroscopy and X-Ray Characterisation of Cationic N-Heteroaryl-Pyridylamido $Zr^{IV}$ Complexes: A Further Level of Complexity for the Elusive Active Species of Pyridylamido Olefin Polymerisation Catalysts. *Chemistry Eur. J.*, **2014**, *20*, 232-244.
46. D'Auria, I.; Milione, S.; Caruso, T.; Balducci, G.; Pellecchia, C. Synthesis of Hyperbranched Low Molecular Weight Polyethylene Oils by an Iminopyridine Nickel(II) Catalyst. *Polym. Chem.*, **2017**, *8*, 6443–6454.
47. Li, G.; Lamberti, M.; Mazzeo, M.; Pappalardo, D.; Roviello, G.; Pellecchia, C. Anilidopyridyl-Pyrrolide and Anilidopyridyl-Indolide Group 3 Metal Complexes: Highly Active Initiators for the Ring-Opening Polymerization of *rac*-Lactide. *Organometallics* **2012**, *31*, 1180−1188.

48. Li, G.; Lamberti, M.; Pappalardo, D.; Pellecchia, C. Random Copolymerization of ε-Caprolactone and Lactides Promoted by Pyrrolylpyridylamido Aluminum Complexes. *Macromolecules* **2012**, 45, 8614−8620.
49. D'Auria, I.; Tedesco, C.; Mazzeo, M.; Pellecchia, C. New Homoleptic Bis(pyrrolylpyridiylimino) Mg(II) and Zn(II) Complexes as Catalysts for the Ring-Opening Polymerization of Cyclic Esters via an "Activated Monomer" Mechanism. *Dalton Trans.* **2017**, *46*, 12217-12225.
50. D'Auria, I.; D'Alterio, M. C.; Talarico, G.; Pellecchia, C. Alternating Copolymerization of $CO_2$ and Cyclohexene Oxide by New Pyridylamidozinc(II) Catalysts. *Macromolecules* **2018**, *51*, 9871−9877.
51. Crisholm, M.; Choojun, K.; Gallucci, J.; Wambua, P. Chemistry of Magnesium alkyls Supported by 1,5,9-trimesityldipyrromethene and 2-[(2,6-diisopropylphenyl)amino]-4-[(2,6-diisopropylphenyl)imino]pent-2-ene. A comparative study. *Chem. Sci.* **2012**, *3*, 3445-3457.
52. Keram, M.; Ma, H. Ring-Opening Polymerization of Lactide, ε-Caprolactone and their Copolymerization Catalyzed by β-diketiminate Zinc Complexes. *Appl. Organometal. Chem.* **2017**, *31*, e3893.
53. Bonnet, F.; Stoffelbach, F.; Fontained, G.; Bourbigot, S. Continuous Cyclo-Polymerisation of L-Lactide by Reactive Extrusion Using Atoxic Metal-Based Catalysts: Easy Access to Well-Defined Polylactide Macrocycles. *RSC Adv.* **2015**, *5*, 31303–31310.

The work presented in this chapter has been published as: D'Auria, I.; D'Alterio, M. C.; Tedesco, C.; Pellecchia, C. Tailor-made block copolymers of L-, D- and *rac*-lactides and ε-caprolactone via one-pot sequential ring opening polymerization by pyridylamidozinc(II) catalysts *RSC Adv.* **2019**, *9*, 32771–32779 DOI: 10.1039/c9ra07133d

# Chapter 4

# Base-controlled, product switch in the ruthenium-catalyzed protodecarbonylation of phthalimides: a mechanistic study


## Abstract

The whole reaction mechanism of the ruthenium-catalyzed protodecarbonylation of N-substituted phthalimides into secondary amides was unravelled by a combined experimental and theoretical study. The chemoselectivity of the reaction, which is catalyzed by *para*-cymene coordinated Ru(II) species all over the catalytic cycle, is exclusively controlled by the unique roles of the bases. Whereas in the presence of $K_2CO_3$ or KOH at high temperatures the same product (benzamide) is mainly formed, whereas at low temperatures KOH led to an unexpected side-product (phthalamic acid) and no reactivity was observed with $K_2CO_3$. The non-covalent interactions between the potassium cations and the different carbonyl groups in the molecules are key to provide a thermodynamically favourable pathway with energetically accessible transition states. The unexpected formation of $CO_2$ in the course of the reaction originates from the phthalimide substrate and the base $K_2CO_3$ in two different elementary steps, respectively.


## 4 .1 Introduction

In the context of homogeneous catalysis, ruthenium is a promising alternative to precious metals since it displays a large number of oxidation states (from +8 to -2) and coordination geometries comparable to most of the most expensive metals.[1] In addition, the reactivity of ruthenium complexes for fine chemical synthesis has been well-established during the last decades.[1] The most relevant breakthroughs in this context are (1) the asymmetric hydrogenation of ketones into chiral alcohols with

Ru-BINAP-diamine complexes by Noyori,[2] (2) the olefin metathesis reaction with $RuCl_2(PCy_3)_2(CHPh)$ as pre-catalyst by Grubbs,[3] and (3) the C-H bond functionalization of aryl moieties with $RuH_2(CO)(PPh_3)_3$ as pre-catalyst by Murai using ketones as directing groups.[4] Aiming at discovering new chemical reactivity at ruthenium, some us have recently reported a general and high functional group tolerant protodecarbonylation of *N*-substituted phthalimides into amides using $[RuCl_2(p\text{-cymene})]_2$ as pre-catalyst in the presence of $K_2CO_3$ and water at high temperatures (Scheme 4.1).[5] Herein, we show detailed control experiments together with theoretical calculations at the DFT level to identify the mechanism operating in this ruthenium-catalyzed reaction, in particular, regarding the five-membered ring-opening step.[6] Key for the success of the reaction is the manifold roles played by the base. In particular, the non-covalent interactions between potassium cations and carbonyl groups as well as an unexpected intramolecular nucleophilic attack prior to the release of $CO_2$ have been identified. An interesting switch of product selectivity is observed when using KOH instead of $K_2CO_3$ as the base. It is relevant to note that the formal opposite reaction, namely the CO-carbonylation of amides into phthalimides catalysed by ruthenium and rhodium has been reported by Chatani;[7] and Rovis, respectively.[8] Recently, Goossen, Hartwig and Zhao, Hong, Baidya, and Shi, independently, have also reported appealing ruthenium-catalyzed decarboxylative reactions with structurally-related benzoic acid derivatives,[9] apart from the homologous work with nickel[10] and palladium.[11]

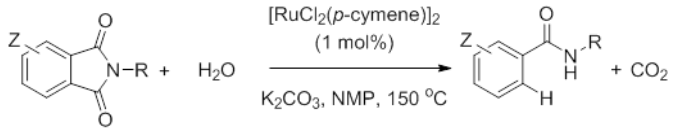


**Scheme 4.1.** Ruthenium-catalyzed protodecarbonylation of phthalimides whose mechanism is studied in this contribution. [NMP = *N*-methyl-2-pyrrolidone; R = alkyl, benzyl, aryl; Z = F, Cl, $NO_2$, Me; tolerant to -CN, -OMe, $-CF_3$, -Br, -I, -C(O)Me, $-CO_2Et$, pyridine, quinoline, thiophene].

## 4.2 Experimental

### 4.2.1 General methods

All reagents were obtained from commercial sources and used as supplied. All reactions were carried out in flame-dried glassware under argon atmosphere unless otherwise noted. Catalytic experiments were performed in Schlenk-type flasks under argon atmosphere unless otherwise noted. Organic solutions were concentrated under reduced pressure using a rotary evaporator. Thin-layer chromatography (TLC) were carried out on 0.25 mm Merck silica gel (60-F254). Flash column chromatography was performed using silica gel Silica 60 M, 0.04-0.063 mm. *N*-Methyl-2-pyrrolidone (NMP) was distilled under reduced pressure and stored under molecular sieves and argon atmosphere. Technical grade petroleum ether (40-60) and ethyl acetate were used for column chromatography. $CDCl_3$ was stored under nitrogen over molecular sieves. NMR spectra were recorded on an AVANCE III 400 spectrometer. $^1H$ NMR spectra were referenced to residual protiated solvent ($\delta$ = 7.26 ppm for $CDCl_3$) and $^{13}C$ chemical shifts are reported relative to deuterated solvents ($\delta$ = 77.0 ppm for $CDCl_3$). The peak patterns are indicated as follows: s, singlet; d, doublet; t, triplet; q, quartet; m, multiplet, and br. for broad. GC-MS analyses were performed with a GCMS-QP2010S (Shimadzu) instrument with a GC-2010 equipped with a 30 m capillary column (Supelco, SLBTM-5ms, fused silica capillary column, 30 m x 0.25 mm x 0.25 mm film thickness), which was used with helium as the vector gas. The following GC conditions were used: initial temperature 80 $^oC$ for 2 minutes, then rate 20 $^oC$/min until 280 $^oC$ and 280 $^oC$ for 28 minutes. HRMS were recorded on a Waters Q-Tof 2 mass spectrometer at the corresponding facilities of the CRMPO, Centre Régional de Mesures Physiques de l'Ouest, Université de Rennes 1.

### 4.2.2 Synthesis and characterization of substrates

**Synthesis and characterization of substrate 1.** Phthalimide (7 mmol, 1.03 g, 1 equiv.), potassium carbonate (14 mmol, 2.59 g, 2 equiv.) and iodomethane (14 mmol, 2 equiv.) were heated at 40 $^{o}$C in *N*,*N*-dimethylformamide (6 mL) for 18 hours. After solvents evaporation under vacuum, water was added to the reaction mixture followed by extraction with DCM. The combined organic phases were dried over $MgSO_4$, filtered, and concentrated in vacuo. The desired phthalimide **1** was purified by silica gel column chromatography with a mixture of petroleum ether and ethyl acetate as eluent in 88% isolated yield. *N*-Methylphthalimide (**1**): $^{1}$H NMR (400 MHz, $CDCl_3$): $\delta$ = 7.78 (dd, *J* = 5.6 Hz, 3.2 Hz, 2H), 7.66 (dd, *J* = 5.6 Hz, 3.2 Hz, 2H), 3.13 (s, 3H) ppm. The spectral data match those previously reported.[20]

**General procedure for the catalysis and characterization of 2-3.** $[RuCl_2(p\text{-cymene})]_2$ (0.004 mmol, 2.5 mg, 0.01 equiv.), base (1.2 mmol, 165.8 mg, 3 equiv.), distilled water (0.6 mmol, 10.8 mg, 10.8 μL, 1.5 equiv.), substrate **1** (0.4 mmol, 1 equiv.) and *N*-methyl-2-pyrrolidone (2.0 mL) were introduced in a flame-dried Schlenk tube under argon atmosphere. The reaction mixture was stirred at 150 $^{o}$C during 6 hours. Then, the reaction mixture was cooled down to room temperature and diluted with water (20 mL). Then, HCl (1 M) was added until pH reached *ca.* 7. The aqueous phase was extracted with ethyl acetate (3 x 20 mL) and the combined organic layer was dried over anhydrous $MgSO_4$, filtered, and concentrated in vacuo. After solvents evaporation, the crude product **2** was obtained. [Note: In order to detect product **3** a small change in the work-up was performed using excess of HCl in order to reach pH *ca.* 1.]

***N*-Methylbenzamide (2).** Isolated by column chromatography ($SiO_2$, petroleum ether/ethyl acetate, 5:1 to 2:1, *v*/*v*) in 93% yield (50.3 mg) as a colourless solid. $^{1}$H NMR (400 MHz, $CDCl_3$) (Figure 4.1): $\delta$ = 7.77-7.74 (m, 2H), 7.49-7.45 (m, 1H), 7.42-7.38 (m, 2H), 6.42 (br. s, 1H), 2.98 (d, *J* = 4.8 Hz, 3H) ppm. $^{13}$C{$^{1}$H} NMR

(100 MHz, $CDCl_3$) (Figure 4.2): $\delta$ = 168.3, 134.5, 131.2, 128.3, 126.8, 26.7 ppm. GC: $t_R$ = 8.7 min; MS (EI): *m/z* = 134 ($M^+$, 48), 105 (100), 77 (91), 51 (34). The spectral data match those previously reported.[21]

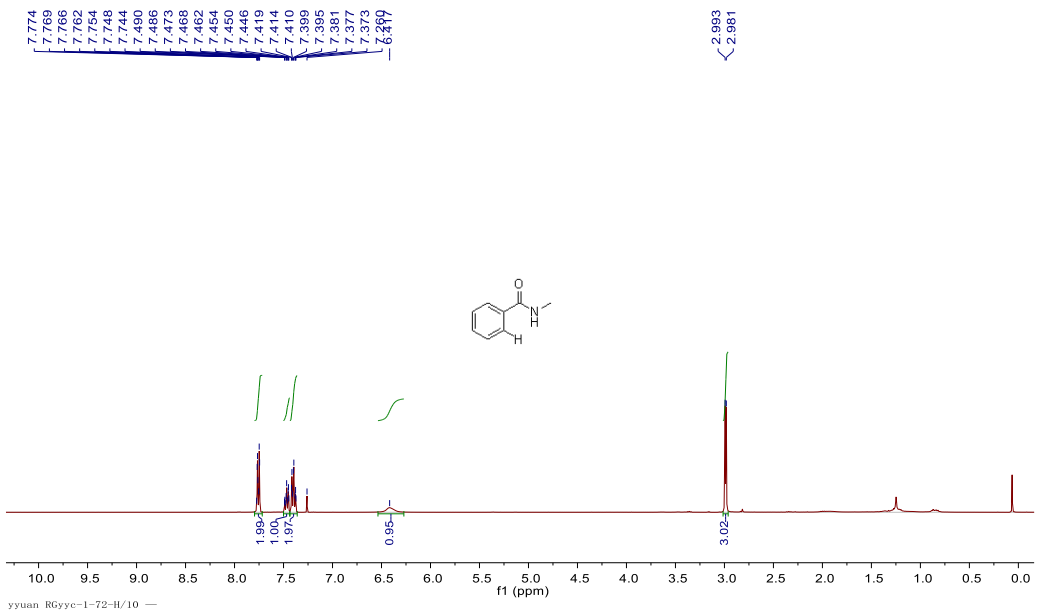


**Figure 4.1.** $^1$H NMR (400 MHz, $CDCl_3$) spectrum of **2**.

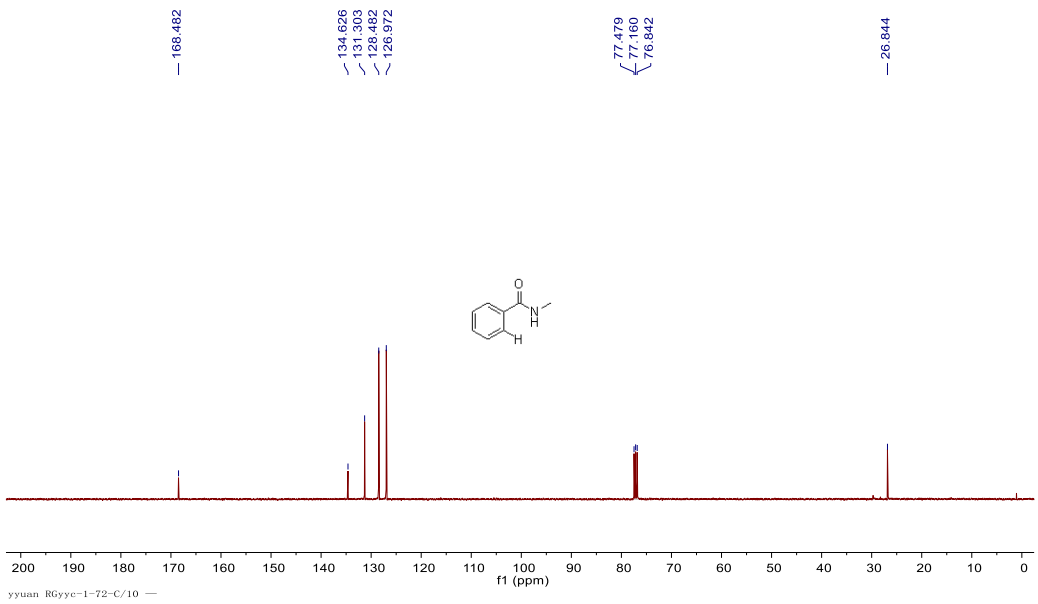


**Figure 4.2.** $^{13}C\{^{1}H\}$ NMR (100 MHz, $CDCl_3$) spectrum of **2**.

**2-(Methylcarbamoyl)benzoic acid (3).** Crude product. $^{1}H$ NMR (400 MHz, $CDCl_3$) (Figure 4.3): $\delta$ = 7.98 (d, $J$ = 7.2 Hz, 1H), 7.48-7.43 (m, 3H), 6.89 (br. s, 1H), 2.94 (d, $J$ = 4.4 Hz, 3H) ppm. $^{13}C\{^{1}H\}$ NMR (100 MHz, $CDCl_3$) (Figure 4.4): $\delta$ = 175.5, 171.4, 136.1, 134.0, 131.9, 125.8, 123.2, 27.1 ppm. HRMS (ESI) calcd. for $[M + Na]^+$ $C_9H_9NO_3Na$ 202.0475, found 202.0476 (1 ppm).

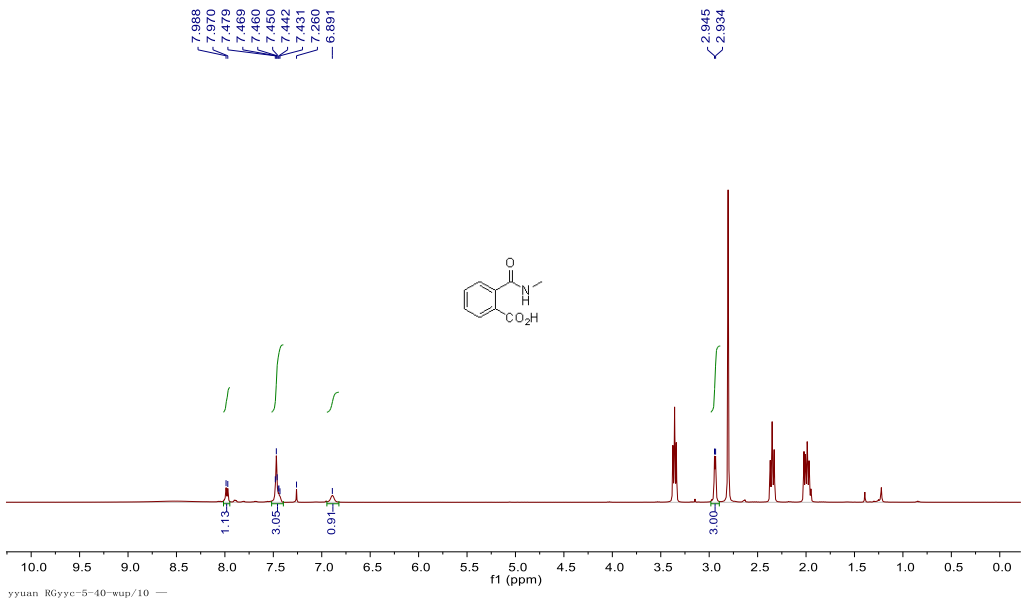


**Figure 4.3** $^{1}H$ NMR (400 MHz, $CDCl_3$) spectrum of **3**.

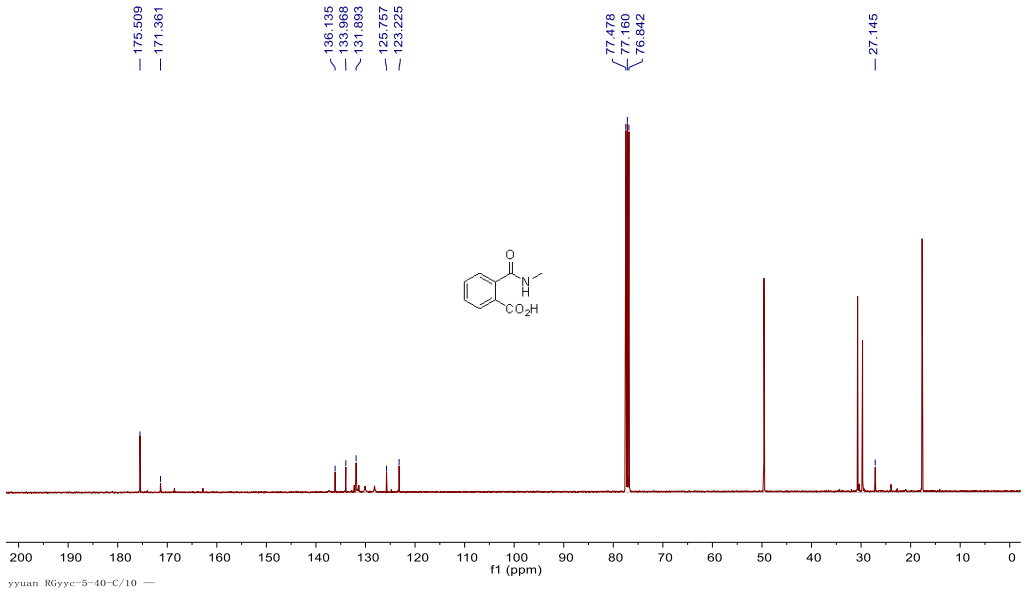


**Figure 4.4** $^{13}C\{^{1}H\}$ NMR (100 MHz, $CDCl_3$) spectrum of **3**.

### 4.2.3 Computational details

All the DFT static calculations were performed with the Gausian09 set of programs,[22] using the BP86 functional of Becke and Perdew,[23-25] together with the Grimme D3 correction term to the electronic energy.[26] The electronic configuration of the molecular systems was described with the double-ζ basis set with polarization of Ahlrichs for main-group atoms (SVP keyword in Gaussian),[27] whereas for ruthenium the small−core quasi−relativistic Stuttgart/Dresden effective core potential, with an associated valence basis set (standard SDD keywords in Gaussian09) were employed.[28-30] The geometry optimizations were performed without symmetry constraints, with analytical frequency calculations for the characterization of the located stationary points. These frequencies were used to calculate unscaled zero-point energies (ZPEs) as well as thermal corrections and entropy effects at 298.15 K. Energies were obtained by single-point calculations on the optimized geometries with the M06 functional[31] and the cc-pVTZ basis set.[32] The reported free energies in this work include energies obtained at the M06/cc-pVTZ~sdd level of theory corrected with zero-point energies, thermal corrections and entropy effects evaluated at 298.15 K, achieved at the BP86-D3/SVP~sdd level plus a solvation contribution evaluated by means of PCM model (n,n-dimethylacetamide).[33]

## 4.3 Results and discussion

### 4.3.1 Catalytic experiments

The optimal reaction conditions previously developed consisted in $[RuCl_2(p\text{-cymene})]_2$ (1 mol%), 1.5 equivalent of water and 3 equivalents of $K_2CO_3$ at 150 $^oC$ during 6 hours.[5] Under these reaction conditions, *N*-methylphthalimide (**1**) fully reacted leading to *N*-methylbenzamide (**2**) in almost quantitative yield (Table 4.1, entry 1). Previous, preliminary mechanistic investigations indicated that $CO_2$ was

formed in the course of the reaction and water served as the source of protons according to GC gas phase analysis and deuteration experiments, respectively.[5] A classical hydrogenation pathway was unlikely as the reaction did not occur in the presence of $H_2$ gas; and a slight excess of $K_2CO_3$ and water was required for the success of the transformation.[5] In addition, radical trapping experiments and mercury tests suggested an homogeneous pathway involving no formation of radicals.[5]

With this background, we performed a number of experiments with different ruthenium complexes as pre-catalysts in view of understanding which ligands lead to catalytically productive ruthenium species. $K_2CO_3$ and KOH bases were evaluated at different temperatures as shown in Table 4.1. The same catalytic outcome was observed with 2 mol% of [Ru(*p*-cymene)($MesCO_2$)$_2$] (Mes = 2-mesityl) as the pre-catalyst (Table 4.1, entry 2),[12] whereas a poor conversion of 30% was observed with 2 mol% of the *para*-cymene-free [Ru($NC^tBu$)$_6$($BF_4$)$_2$] complex and no formation of the expected product **2** (Table 4.1, entry 3).[13] These data strongly suggested that the catalytically active metal complex involved chloride-free, monomeric *para*-cymene-coordinated ruthenium(II) species.

For comparison purposes, we performed a reaction with KOH as the base instead of $K_2CO_3$ as we reasoned that the anion of the base (hydroxyl *versus* carbonate) could influence the catalysis to some extent. At 150 $^oC$ with 1 mol% of [$RuCl_2$(*p*-cymene)]$_2$, full conversion of **1** was observed with the unexpected side-formation of *N*-methylphthalamic acid (**3**) together with the benzamide **2** as the products (Table 4.1, entry 4). Interestingly, **3** became the major product of the reaction when decreasing the temperature to 100 $^oC$ (Table 4.1, entry 5) and at room temperature it was exclusively formed with full conversion of **1** (Table 4.1, entry 6). It is important to note that metal-free, base-mediated five-membered ring-opening of *N*-substituted phthalimides are known to occur only at high temperatures,[14] which further supports that the formation of **3** at room temperature using KOH is indeed catalysed by ruthenium species. In stark contrast, using $K_2CO_3$ as the base at room temperature

led to no conversion of starting material **1** (Table 4.1, entry 7). The starting material was recovered unreacted when the reaction was performed without base regardless of the temperature (Table 4.1, entries 8-9).[5]

**Table 4.1.** Evaluation of ligand, base, and temperature in the ruthenium-catalyzed protodecarbonylation of phthalimide **1**.[a]

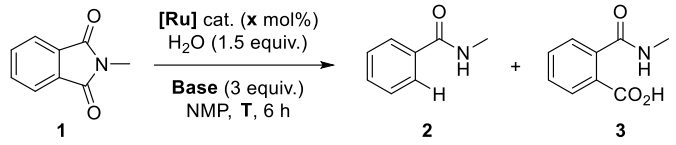


| Entry | [Ru] (x mol%) | Base | T (°C) | **1** : **2** : **3**[b] |
|---|---|---|---|---|
| 1 | $[RuCl_2(p\text{-cymene})]_2$ (1) | $K_2CO_3$ | 150 | 0 : 100 : 0 |
| 2 | $[Ru(p\text{-cymene})(MesCO_2)_2]$ (2) | $K_2CO_3$ | 150 | 0 : 100 : 0 |
| 3 | $[Ru(NC^tBu)_6(BF_4)_2]$ (2) | $K_2CO_3$ | 150 | 70 : 0 : 0[c] |
| 4 | $[RuCl_2(p\text{-cymene})]_2$ (1) | KOH | 150 | 0 : 72 : 28 |
| 5 | $[RuCl_2(p\text{-cymene})]_2$ (1) | KOH | 100 | 0 : 10 : 90 |
| 6 | $[RuCl_2(p\text{-cymene})]_2$ (1) | KOH | 25 | 0 : 0 : 100 |
| 7 | $[RuCl_2(p\text{-cymene})]_2$ (1) | $K_2CO_3$ | 25 | 100 : 0 : 0 |
| 8 | $[RuCl_2(p\text{-cymene})]_2$ (1) | - | 25 | 100 : 0 : 0 |
| 9 | $[RuCl_2(p\text{-cymene})]_2$ (1) | - | 100 | 100 : 0 : 0 |

[a]Reaction conditions: **1** (0.4 mmol), $H_2O$ (0.6 mmol), base (1.2 mmol), NMP (2 mL), Argon. [b]Determined by $^1H$ NMR spectroscopy using 1,3,5-trimethoxybenzene as internal standard and by GC-MS analysis. [c]Unknown by-products are formed.

### 4.3.2 DFT calculations

Taking into account all the previous experimental data and the difficulty to isolate any potential ruthenium intermediates during the catalysis,[8] theoretical calculations at the DFT level were carried out to gain a better understanding of the origin of the

chemoselectivity observed by swapping the base in the ruthenium-catalyzed protodecarbonylation of phthalimides.[15]

First, the catalytic cycle was studied for the case where $K_2CO_3$ as the base is employed, which selectively leads to benzamide **2** at 150 $^oC$ (Figure 4.6A). The initial catalytically active species for the calculations was rationalized to be a cationic 16 electron Ru(II) complex with one $\mu^6$-coordinated *para*-cymene ligand and one $\kappa^2$-coordinated carbonate ligand with a vacant site at ruthenium (**CAT**, Figure 4.6A). Such hypothesis is further supported by the findings from Demerseman and co-workers who reported that [Ru(*p*-cymene)$Cl_2(PR_3)$] (R= Me, Cy, Ph) reacted with $K_2CO_3$ in a polar solvent (i.e. acetone) leading to [Ru(*p*-cymene)($\kappa^2$-$O_2CO$)($PR_3$)] species.[16] In addition, we verified that the reaction of [$RuCl_2$(*p*-cymene)]$_2$ with $K_2CO_3$ releasing KCl and forming [Ru(*p*- cymene)($\kappa^2$-$O_2COK$)]$^+$ (**CAT**) is highly exergonic with $\Delta G$ = -40.1 kcal/mol (Figure 4.5, left).

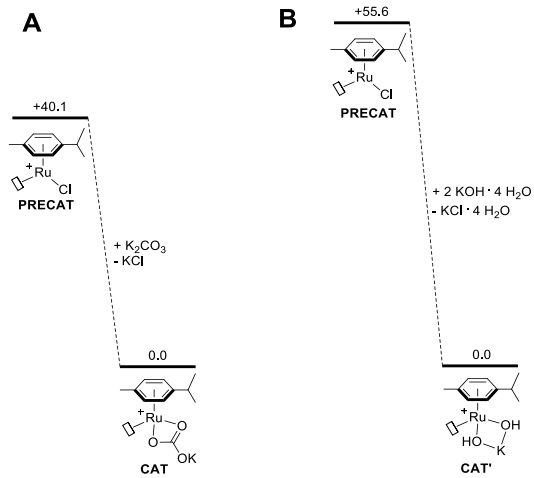


**Figure 4.5** Computed, minimum free energy reaction profile (kcal/mol) for the formation of the catalysts **CAT** (left) and **CAT'** (right).

In the intermediate **INT2**, the hybridization of one carbon atom switches from $sp^2$ in **INT1** to $sp^3$ in **INT2** with a subsequent elongation of the C-N bond by 0.06 Å ($d_{C-N}$ = 1.39 Å in **INT1** *versus* $d_{C-N}$ = 1.45 Å in **INT2**). Next, the simultaneous five-

membered ring-opening of **1** and the decarboxylation from the carbonate fragment occurs *via* **TS2** (Figure 4.6A) giving rise to intermediate **INT3** (Figure 4.6A).

**TS2** appears to be the rate determining step of the catalytic cycle with an energetic cost of 44.0 kcal/mol with respect to **CAT** (Figure 4.6A). The calculated energetic barrier is in full agreement with the experimental reaction temperature of 150 $^{o}$C required for the success of the catalysis. Despite the latter energetically-demanding step *via* **TS2**, the previous intramolecular nucleophilic attack defined by **TS1** is crucial in kinetic terms as well, since the weakening of the C-N bond in **INT2** ($d_{C\text{-}N}$ = 1.45 Å, *vide supra*) makes the former substrate ready for the ring-opening (Figure 4.6A). Indeed, for comparison purposes, we modelled the transition state (TS) of the five-membered ring-opening of **1** without the previous nucleophilic attack. In this case, the substrate **1** coordinates to ruthenium *via* the nitrogen atom and a carbon atom belonging to the carbonyl group (Figure 4.7B) with an energetic barrier that goes up to 75.1 kcal/mol with respect to **CAT** in order to form the intermediate **INT3**. From intermediate **INT3**, a decarboxylation occurs within the substrate *via* **TS3** with an energy barrier of 17.4 kcal/mol with respect to **INT3**, affording the very stable five-membered ruthenacycle **INT4** (Figure 4.6A). The high stability of **INT4** is largely ascribed to the formation of the new Ru-C(aryl) bond. The next concerted **TS4**, with an energy barrier of 25.0 kcal/mol, requires the participation of one molecule of $H_2O$ (Figure 4.6A). More precisely, the Ru-C(aryl) bond is broken *via* a proton-transfer from $H_2O$ to the carbon atom and the hydroxyl group from $H_2O$ migrates to the potassium cation, formally releasing KOH. Thus, a new $K_2CO_3$ molecule enters in the catalytic cycle serving as a ligand to ruthenium leading to intermediate **INT5**, in which the benzamide product is already coordinated to the catalyst.

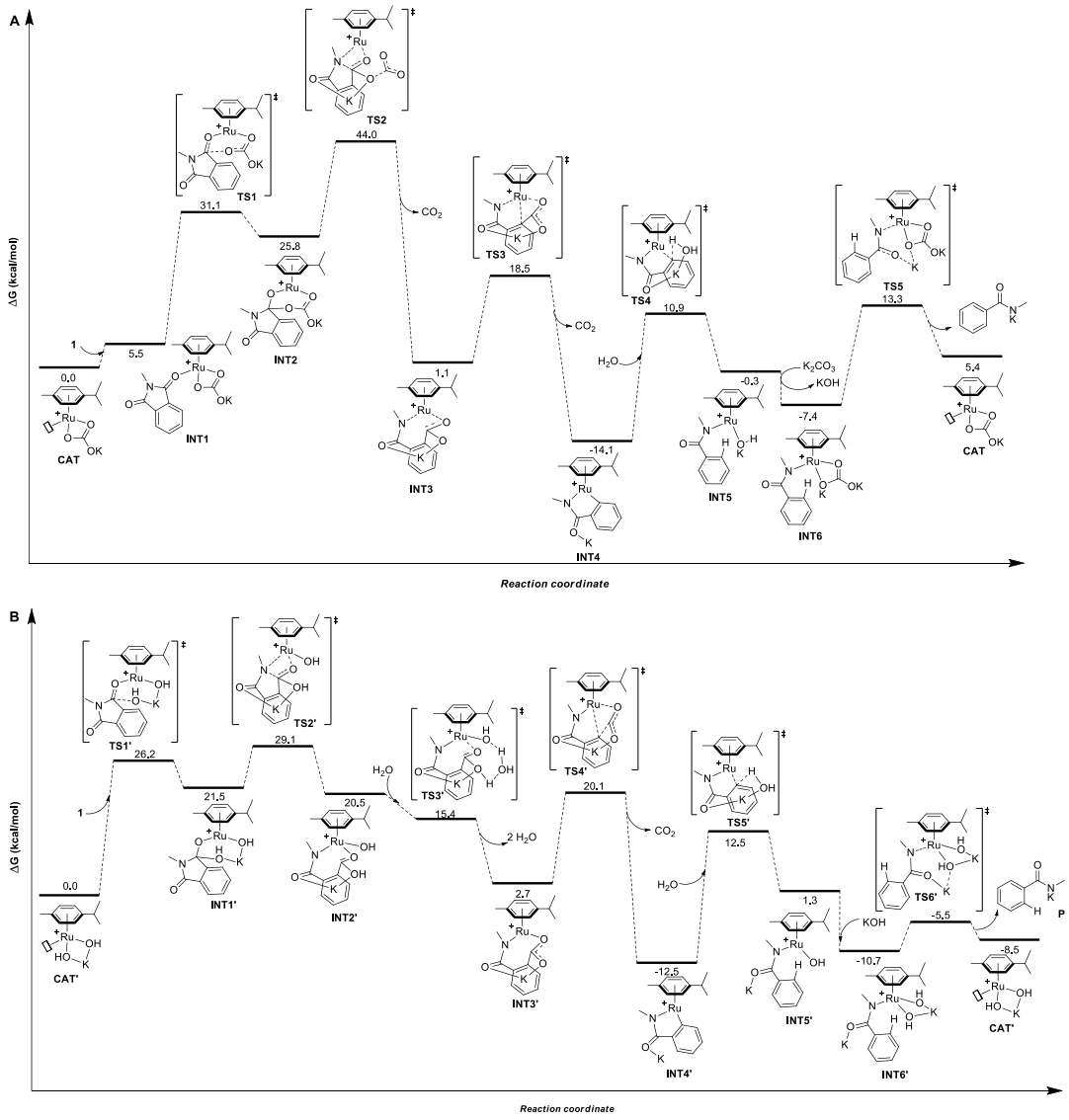


**Figure 4.6**. (**A**) Computed, minimum free energy reaction profile (in kcal/mol) for the ruthenium-catalyzed protodecarbonylation of **1** assisted by $K_2CO_3$, and (**B**) computed, minimum free energy reaction profile (in kcal/mol) for the ruthenium-catalyzed protodecarbonylation of **1** assisted by KOH.

The theoretical evidence of the second additional $K_2CO_3$ molecule is in agreement with the experimental requirements of an excess of base to reach good yields of the benzamide product. The elementary step (**INT4 → INT5**) is well supported by the experimental evidence that 1.5 equivalents of water are enough to the catalysis for completion (Table 4.1). Next step is supported by the excess of $K_2CO_3$, together with the thermodynamic stability of **INT6** (7.1 kcal/mol). Finally, **P** is released *via* **TS5** with an energy barrier of 20.7 kcal/mol, however 27.4 kcal/mol from **INT4** (Figure 4.6A). Experimentally, **2** is obtained from **P** by an acidic work-up.

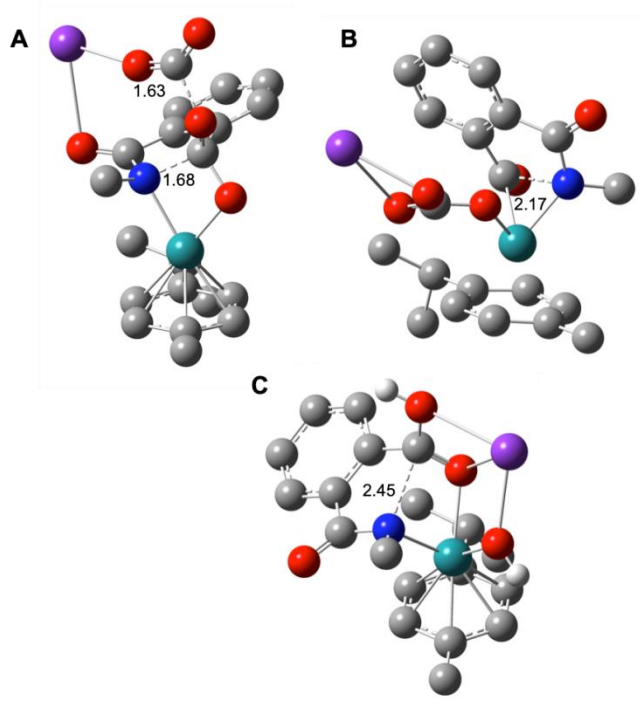


**Figure 4.7.** Computed molecular structures of the five-membered ring opening rate determining step TS2 in the case of $K_2CO_3$ as a base for the assisted mechanism of Figure 4.6, (A); without considering the intramolecular nucleophilic attack from **INT1** to **INT2** (B); In (C) is reported the five-membered ring opening **TS2'** of Figure 4.6B for the KOH assisted mechanism. H atoms omitted for clarity (except the protic ones). Selected distances are displayed in Å. Color code: Ru in green, K in purple, O in red, N in blue and C in gray.

In the case of the product selectivity controlled by KOH, we reasoned that the catalytically active ruthenium species might be the mononuclear $[Ru(OH)_2(p\text{-cymene})K]^+$ complex (**CAT'**, Figure 4.6B) similar to the experimental findings from Stephenson and co-workers.[17] For that, the calculations performed for the reaction of $[RuCl_2(p\text{-cymene})]_2$ with KOH forming **CAT'** and KCl led to a highly favourable exergonic process with $\Delta G$ = -55.6 kcal/mol (Figure 4.5B). In this case, we considered that four water molecules form a hydration cluster with KOH, as it was already noted elsewhere.[18,19]

Differently from the case of $K_2CO_3$, the substrate **1** cannot coordinate to catalyst **CAT'** according to calculations (Figure 4.6B). In fact, a carbonyl group of **1** directly undergoes a nucleophilic attack by an hydroxyl-coordinated to ruthenium *via* **TS1'** with an energy barrier of 26.2 kcal/mol (Figure 4.6B). The resulting intermediate **INT1'** presents a carbon atom that has switched its hybridization from $sp^2$ to $sp^3$ resulting in an elongation of the C-N bond of 0.17 Å (from 1.39 Å in 1 to 1.56 Å in **INT1'**). Importantly, the nucleophilic attack of the KOH base and the subsequent C-N bond elongation in **1** both together promote the five-membered ring-opening of substrate **1**.

The rate determining step for the $OH^-$ assisted mechanism is the five-membered ring-opening of **1** (**TS2'** of Figure 4.6B) analogously to the $KCO_3^-$ assisted mechanism (**TS2** of Figure 4.6A); however, we calculated a lower energy barrier for **TS2'** (29.1 kcal/mol) compared with 44.0 kcal/mol of **TS2**. Such observation is a direct consequence of the longer distance of the C-N bond observed in **INT1'** ($d_{C\text{-}N}$ = 0.17 Å, Figure 4.6B) compared to **INT2** ($d_{C\text{-}N}$ = 0.06 Å, Figure 4.6A). This finding suggests a higher reactivity of the $[Ru(OH)_2(p\text{-cymene})K]^+$ complex (**CAT'**) than the $[Ru(p\text{-cymene})(\kappa^2\text{-}O_2COK)]^+$ complex (**CAT**) even at low temperatures. However, experimentally, **CAT'** does not yield any secondary amide **2** as product, but phthalamic acid derivative **3** at low temperatures (Table 4.1, entry 6). Indeed, the intermediate **INT2'** can be considered as the product **3** coordinated to the $[Ru(OH)(p\text{-cymene})]^+$ complex (Figure 4.6B).

Following an alternative mechanistic pathway (Figure 4.8), the addition of a KOH molecule easily releases product **P'**, the $K^+$ salt of **3** and regeneration of the catalyst *via* the transition state **TS3"** with an overall energetic barrier of 13.0 kcal/mol with respect to **CAT'** (Figure 4.8). On the other hand, the pathway leading to the formation of product **2** (Figure 4.6B) requires the two-fold overcoming of energetic barriers higher than 13.0 kcal/mol, which are (1) the decarboxylation of the substrate *via* **TS4'** with an energetic barrier of 20.1 kcal/mol, (2) the protonation of the ruthenium-coordinated C(aryl) atom by a water molecule *via* **TS5'** with an energetic barrier of 25.0 kcal/mol.

The results of these two competitive paths explains why at low temperature the Ru-catalysed process leads preferentially to product **3**, while by increasing the temperature all the barriers of the catalytic process are overcome, affording a selectivity toward product **2** at 150°C of the 72% (Table 4.1, entry 4).

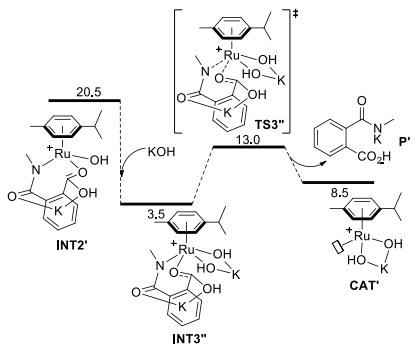


**Figure 4.8.** Computed, minimum free energy reaction profile (in kcal/mol) for the formation of phthalimic acid derivative **P'** from the ruthenium intermediate **INT2'** assisted by KOH.

## 4.4 Conclusions

In summary, by means of experimental and thorough theoretical calculations we have shown that the ruthenium-catalyzed protodecarbonylation of phthalimide derivatives into secondary amides proceeds under a mechanism involving release of two $CO_2$ molecules: one from the substrate and one from the $K_2CO_3$ used as reagent. Interestingly, it was found that the ruthenium center displays an oxidation state +2 through the whole catalytic cycle and the potassium cations are relevant to stabilise all the intermediates *via* weak interactions with the carbonyl groups present either in the substrate and/or the carbonate ligands. The catalysis performed in the presence of KOH as the base at high temperature led to the formation of the secondary amide product, however, at low temperature the formation of a phthalamic acid derivative was exclusively observed indicating a switch in the reaction mechanism that has been rationalized by theoretical calculations as well. Although in both cases (KOH and $K_2CO_3$), the rate determining step is the same, namely the five-membered ring opening of phthalimide, the presence of KOH in the reaction mixture facilitates an unexpected side-reaction towards phthalamic acid, which is not the case for $K_2CO_3$. Consequently, this work shows the non-trivial, multiple roles that the bases can play in reactions catalysed by ruthenium complexes and it provides insights into new mechanistic hypothesis that might be considered in related transition metal-based catalytic reactions.

## References

1. Seddon, E. A.; Seddon, K. R. The Chemistry of Ruthenium, Elsevier Science, **1984**; (b) Murahashi, S.-I. Ruthenium in Organic Synthesis, Wiley-VCH, Weinheim, Germany **2004**; (c) Bruneau, C.; Dixneuf, P. H. Ruthenium in Catalysis, Top. Organomet. Chem., 48, Springer-Verlag, Berlin-Heidelberg, Germany **2014**.

2. Noyori, R.; Hashiguchi, S. Asymmetric Transfer Hydrogenation Catalyzed by Chiral Ruthenium Complexes, *Acc. Chem. Res.* **1997**, *30*, 97-102; (b) Noyori, R.; Okhuma, T. Asymmetric Catalysis by Architectural and Functional Molecular Engineering: Practical Chemo- and Stereoselective Hydrogenation of Ketones. *Angew. Chem. Int. Ed*. **2001**, *40*, 40-73.
3. Trnka, T. M.; Grubbs, R. H. The Development of $L_2X_2Ru$=CHR Olefin Metathesis Catalysts: An Organometallic, Success Story. *Acc. Chem. Res*. **2001**, *34*, 18; (b) Grubbs, R. H. Olefin Metathesis. *Tetrahedron* **2004**, *60*, 7117-7140; (c) Credendino, R.; Poater, A.; Ragone, F.; Cavallo, L. A Computational Perspective of Olefins Metathesis Catalyzed by N-Heterocyclic Carbene Ruthenium (Pre)catalysts. *Catal. Sci. Technol*. **2011**, *1*, 1287-1297; (d) Poater A.; Cavallo, L. A Comprehensive Study of Olefin Metathesis Catalyzed by Ru-Based Catalysts. *Beilstein J. Org. Chem*. **2015**, *11*, 1767-1780.
4. Murai, S.; Kakiuchi, F.; Sekine, S.; Tanaka, Y.; Kamatani, A.; Sonoda, M.; Chatani, N. Efficient Catalytic Addition of Aromatic Carbon-Hydrogen Bonds to Olefins. *Nature* **1993**, *366*, 529-531.
5. Yuan, Y.-C.; Kamaraj, R.; Bruneau, C.; Labasque, T.; Roisnel, T.; Gramage-Doria R. Unmasking Amides: Ruthenium-Catalyzed Protodecarbonylation of N-Substituted Phthalimide Derivative. *Org. Lett.* **2017**, *19*, 6404-6407.
6. Yuan, Y.-C.; Bruneau, C.; Dorcet, V.; Roisnel, T.; Gramage-Doria, R. Ru-Catalyzed Selective C-H Bond Hydroxylation of Cyclic Imides, *J. Org. Chem.* **2019**, *84*, 1898-1907; (b) Poater, A.; Vummaleti, S.V.C. and Cavallo, L. Catalytic Role of Nickel in the Decarbonylative Addition of Phthalimides to Alkynes. *Organometallics* **2013**, *32*, 6330-6336.
7. Inoue, S.; Shiota, H.; Fukumoto, Y.; Chatani, N. Ruthenium-Catalyzed Carbonylation at Ortho C− H Bonds in Aromatic Amides Leading to Phthalimides: C− H Bond Activation Utilizing a Bidentate System. *J. Am. Chem. Soc.* **2009**, *131*, 6898-6899; (b) Hasegawa, N.; Charra, V.; Inoue, S.;

Fukumoto, Y.; Chatani, N. Highly Regioselective Carbonylation of Unactivated C(sp3)–H Bonds by Ruthenium Carbonyl. *J. Am. Chem. Soc*. **2011**, *133*, 8070-8073.

8. Du, Y.; Hyster T. K.; Rovis, T. Rhodium(III)-Catalyzed Oxidative Carbonylation of Benzamides with Carbon Monoxide. *Chem. Commun*. **2011**, *47*, 12074-12076.
9. Huang, L.; Biafora, A.; Zhang, G.; Bragoni V.; Goossen, L. J. Regioselective C-H Hydroarylation of Internal Alkynes with Arenecarboxylates: Carboxylates as Deciduous Directing Groups, *Angew. Chem. Int. Ed*. **2016**, *55*, 6933-6937; (b) Zhang, J.; Shrestha, R.; Hartwig J. F.; Zhao, P. A Decarboxylative Approach for Regioselective Hydroarylation of Alkynes" *Nat. Chem*. **2016**, *8*, 1144-1151; (c) Yu, J.-L.; Zhang, S.-Q.; Hong, X. Mechanisms and Origins of Chemo- and Regioselectivities of Ru(II)-Catalyzed Decarboxylative C-H Alkenylation of Aryl Carboxylic Acids with Alkynes: A Computational Study, *J. Am. Chem. Soc*. **2017**, *139*, 7224-7243; (d) Mandal, A.; Sahoo, H.; Dana S.; Baidya, M. Ruthenium(II)-Catalyzed Hydroarylation of Maleimides Using Carboxylic Acids as a Traceless Directing Group. *Org. Lett*. **2017**, *19*, 4138-4141; (e) Pu, F.; Liu, Z.-W.; Zhang, L.-Y.; Fan, J.; Shi, X.-Y. Switchable C−H Alkylation of Aromatic Acids with Maleimides in Water: Carboxyl as a Diverse Directing Group, *Chem. Cat. Chem*. **2019**, *11*, 4116-4122.
10. Shiba, T.; Kurahashi T.; Matsubara, S. Nickel-Catalyzed Decarbonylative Alkylidenation of Phthalimides with Trimethylsilyl-Substituted Alkynes. *J. Am. Chem. Soc*. **2013**, *135*, 13636-13639.
11. Samanta, P. K.; Biswas, P. Palladium Catalyzed Regioselective Synthesis of Substituted Biaryl Amides through Decarbonylative Arylation of Phthalimides. *J. Org. Chem*. **2019**, *84*, 3968-3976; (b) Zhou, T.-L.; Li, G.-C.; Nolan S. P.; Szostak, M. [Pd(NHC)(acac)Cl]: Well-Defined, Air-Stable, and Readily Available Precatalysts for Suzuki and Buchwald–Hartwig

Cross-coupling (Transamidation) of Amides and Esters by N–C/O–C Activation. *Org. Lett.* **2019**, *21*, 3304-3309. (c) Wang, S.-M.; Zhao, C.; Zhang X.; Qin, H.-L. Clickable Coupling of Carboxylic Acids and Amines at Room Temperature Mediated by $SO_2F_2$: a Significant Breakthrough for the Construction of Amides and Peptide Linkages. *Org. Biomol. Chem*. **2019**, *17*, 4087-4101.

12. Arockiam, P. B.; Bruneau, C.; Dixneuf, P. H. Ruthenium(II)-Catalyzed C–H Bond Activation and Functionalization. *Chem. Rev*. **2012**, *112*, 5879-5883; (b) Ackermann, L. Carboxylate-Assisted Transition-Metal-Catalyzed C−H Bond Functionalizations: Mechanism and Scope, *Chem. Rev*. **2011**, *111*, 1315-1345.
13. Simonetti, M.; Perry, G. J. P.; Cambeiro, X. C.; Julia-Hernandez, F.; Arokianathar J. N.; Larrosa, I. Ru-Catalyzed C–H Arylation of Fluoroarenes with Aryl Halides. *J. Am. Chem. Soc*. **2016**, *138*, 3596-3606.
14. Hasan S. K.; Abbas, S. A Alkaline Hydrolysis Products of N-Substituted Phthalimides. *Can. J. Chem.* **1975**, *53*, 2450-2453; (b) Kumar, P. P.; Devi, B. R.; Dubey P. K.; Mohiuddin, S. M. G. PEG-600 Mediated Simple, Efficient and Eco-Friendly Synthesis of N-substituted Imides and Chemo Selective C=C Reduction. *Green Chem. Lett. Rev*. **2011**, *4*, 341-348.
15. Meng, Y.-Y.; Si, X.-J.; Song, Y.-Y.; Zhou, H.-M.; Xu, F. Palladium-Catalyzed Decarbonylative Annulation of Phthalimides with Arynes: Direct Construction of Phenanthridinone. *Chem. Commun*. **2019**, *55*, 9507-9510.
16. Demerseman, B.; Mbaye, M. D.; Sémeril, D.; Toupet, L.; Bruneau, C.; Dixneuf, P.F. Direct Preparation of [Ru(η2-O2CO)(η6-arene)(L)] Carbonate Complexes (L = Phosphane, Carbene) and Their Use as Precursors of [RuH2(p-cymene)(PCy3)] and [Ru(η6-arene)(L)(MeCN)2][BF4]2: X-ray Crystal Structure Determination of [Ru(η2-O2CO)(p-cymene)(PCy3)]·1/2CH2Cl2 and [Ru(η2-O2CO)(η6-C6Me6)(PMe3)]·H2O. *Eur. J. Inorg. Chem.* **2006**, *6*,1174-1181.

17. Arthur T.; Robertson, D. R.; Tocher D. A.; Stephenson, T. A. Synthesis of Binuclear Hydroxo- and Alkoxo-bridged Arene Complexes of Ruthenium(II) and Osmium(II). *J. Organomet. Chem.* **1981**, *208*, 389-400.
18. Kumar, A.; Park, M.; Huh, J. Y.; Lee, H. M.; Kim, K. S. Hydration Phenomena of Sodium and Potassium Hydroxides by Water Molecules. *J. Phys. Chem. A*, **2006**, *110*, 12484-12493
19. Mahler, J.; Persson, I. A Study of the Hydration of the Alkali Metal Ions in Aqueous Solution. *Inorg. Chem.* **2012**, *51*, 425-438.
20. Takebayashi, S.; John, J. M.; Bergens, S. H. Desymmetrization of meso-Cyclic Imides via Enantioselective Monohydrogenation. *J. Am. Chem. Soc*. **2010**, *132*, 12832-12834.
21. Charette, B.; Grenon, M.; Lemire, A.; Pourashraf, M.; Martel. J. *J. Am. Chem. Soc.* **2001**, *123*, 11829-11830.
22. Gaussian 09, Revision E.01, Frisch, M.J.; Trucks, G.W.; Schlegel, H.B.; Scuseria, G.E.; Robb, M.A.; Cheeseman, J.R.; Montgomery, Jr., J.A.; Vreven, T.; Kudin, K.N.; Burant, J.C.; Millam, J.M.; Iyengar, S.S.; Tomasi, J.; Barone, V.; Mennucci, B.; Cossi, M.; Scalmani, G.; Rega, N.; Petersson, G.A.; Nakatsuji, H.; Hada,M.; Ehara, M.; Toyota, K.; Fukuda, R.; Hasegawa, J.; Ishida, M.; Nakajima, T.; Honda, Y.; Kitao, O.; Nakai, H.; Klene, M.; Li, X.; Knox, J.E.; Hratchian, H.P.; Cross, J. B.; Bakken, V.; Adamo, C.; Jaramillo, J.; Gomperts, R.;Stratmann, R.E.; Yazyev, O.; Austin, A.J.; Cammi, R.; Pomelli, C.; Ochterski, J.W.; Ayala, P.Y.; Morokuma,K.; Voth, G.A.; Salvador, P.; Dannenberg, J.J.; Zakrzewski, V.G.; Dapprich, S.; Daniels, A.D.; Strain, M.C.;Farkas, O.; Malick, D.K.; Rabuck, A.D.; Raghavachari, K.; Foresman, J.B.; Ortiz, J.V.; Cui, Q.; Baboul, A.G.;Clifford, S.; Cioslowski, J.; Stefanov, B.B.; Liu, G.; Liashenko, A.; Piskorz, P.; Komaromi, I.; Martin, R.L.; Fox,D.J.; Keith, T.; Al-Laham, M.A.; Peng, C.Y.; Nanayakkara, A.; Challacombe, M.; Gill, P.M.W.;

Johnson, B.;Chen, W.; Wong, M.W.; Gonzalez, C.; and Pople, J.A.; Gaussian, Inc., Wallingford CT, **2004**.

23. Becke, A.D. Density-Functional Exchange-Energy Approximation with Correct Asymptotic Behaviour. *Phys. Rev. A* **1988**, *38*, 3098-3100.
24. Perdew, J. P. Density-Functional Approximation for the Correlation Energy of the Inhomogeneous Electron Gas, *Phys. Rev. B* **1986**, *33*, 8822-8824.
25. Perdew, J. P. Erratum: Density-functional Approximation for the Correlation Energy of the Inhomogeneous Electron Gas. *Phys. Rev. B* **1986**, *34*, 7406-7406.
26. Grimme, S.; Antony, J.; Ehrlich S.; Krieg, H. A. A Consistent and Accurate Ab-Initio Parametrization of Density Functional Dispersion Correction (DFT-D) for the 94 Elements H-Pu. *J. Chem. Phys.* **2010**, *132*, 154104.
27. Schäfer, S.; Horn, H.; Ahlrichs, R. Fully Optimized Contracted Gaussian Basis Sets for Atoms Li to Kr. *J. Chem. Phys*. **1992**, *97*, 2571-2577.
28. Haeusermann, U.; Dolg, M.; Stoll, H.; Preuss, H.; Schwerdtfeger, P.; Pitzer, R. M. Accuracy of Energy-Adjusted Quasirelativistic Ab-Initio Pseudopotentials. *Mol. Phys*. **1993**, *78*, 1211-1224.
29. Küchle, W.; Dolg, M.; Stoll, H.; Preuss, H. Energy-Adjusted Pseudopotentials for the Actinides. Parameter Sets and Test Calculations for Thorium and Thorium Monoxide. *J. Chem. Phys.* **1994**, *100*, 7535-7542.
30. Leininger, T.; Nicklass, A.; Stoll, H.; Dolg, M.; Schwerdtfeger, P. The Accuracy of the Pseudopotential Approximation. II. A Comparison of Various Core Sizes for Indium Pseudopotentials in Calculations for Spectroscopic Constants of InH, InF, and InCl. *J. Chem. Phys*. **1996**, *105*, 1052-1059.
31. Zhao, Y.; Truhlar, D. G. The M06 Suite of Density Functionals for Main Group Thermochemistry, Thermochemical Kinetics, Noncovalent Interactions, Excited States, and Transition Elements: Two new Functionals

and Systematic Testing of Four M06-class Functionals and 12 other Functionals. *Theor. Chem. Acc.* **2008**, *120*, 215-241.

32. Kendall, R. A.; Dunning Jr. T. H.; Harrison, R. J. Electron Affinities of the First-Row Atoms Revisited. Systematic Basis Sets and Wave Functions. *J. Chem. Phys*. **1992**, *96*, 6796-6806.
33. Barone V.; Cossi, M. Quantum Calculation of Molecular Energies and Energy Gradients in Solution by a Conductor Solvent Model. *J. Phys. Chem. A* **1998**, *102*, 1995-2001.

The work presented in this chapter has been published as: D'Alterio, M. C.; Yuan, Y. C.; Bruneau, C.; Talarico, G.; Gramage-Doria, R.; Poater, A. Base-controlled product switch in the rutheniumcatalyzed protodecarbonylation of phthalimides: a mechanistic study. *Catal. Sci. Technol.* **2020**, *10*, 180 DOI: 10.1039/c9cy02047k

# Appendix

The thesis presented here focused on a well-defined project of ring-opening catalysis applied to the production of materials and products. However, during my Ph.D. I had the opportunity to work on several aspects of computational modeling and material science. For the sake of readability, I did not discuss these topics in detail in the previous chapters, however I reported below the titles and the abstracts of the publications sorted out because I consider these works important for the development of my background both from computational and experimental point of view.

1) D'Alterio, M. C.; De Rosa, C.; Talarico, G. CHAPTER 18 Noncovalent Interactions in Olefin Polymerization Catalysis Promoted by Transition Metals. In *Noncovalent Interactions in Catalysis*, The Royal Society of Chemistry: **2019**; pp 393-414.

Abstract:

We report two case histories where non-covalent interactions play an important role in olefin polymerization catalyzed by transition metals. In the first example, by using DFT calculations, we remark the influence of α-agostic interactions on the stereoselectivity of propene insertion reactions and their contribution to develop new models for the isotactic stereocontrol achieved with non-metallocene catalysts. In the second example we summarize the experimental and theoretical results aiming to explain the role of non-covalent interaction (like F····H or F····M, with M = metal center) in living olefin polymerization promoted by Group 4 non-metallocene systems as well as the chain branching formation of polyethylene obtained by late transition metals.

2) Nagendra, B.; Cozzolino, A.; Daniel, C.; Rizzo, P.; Guerra, G.; Auriemma, F.; De Rosa, C.; D'Alterio, M. C.; Tarallo, O.; Nuzzo, A. Two Nanoporous Crystalline

Forms of Poly(2,6-dimethyl-1,4-phenylene)oxide and Related Co-Crystalline Forms. *Macromolecules* **2019,** *52* (24), 9646-9656.

Abstract:

Extensive characterizations, mainly by wide-angle X-ray diffraction (WAXD) and Fourier transform infrared (FTIR) techniques, are reported for co-crystalline (CC) poly(2,6-dimethyl-1,4-phenylene)oxide (PPO) films with many different low-molecular-mass guest molecules. These characterizations are also reported for the corresponding nanoporous crystalline (NC) phases, as obtained by suitable guest-removal procedures. Two well-separated NC forms, hereafter named α and β, are obtained by guest removal from two well-separated groups of CC forms. α and β NC forms can be easily recognized by reflections in WAXD patterns as well as by suitable FTIR crystalline peaks. Density and degree of crystallinity measurements confirm that both NC phases exhibit a density definitely smaller than for the amorphous phase (ρam = 1.04 g/cm3 > ρβ = 0.95 g/cm3 > ρα = 0.93 g/cm3). Density functional theory calculations combined with geometrical analysis on PPO model systems indicate conformations suitable to fit the observed chain periodicities of the two crystalline forms (c = 5.28 and 5.47 Å, for α and β NC forms, respectively).

3) De Rosa, C.; Malafronte, A.; Auriemma, F.; Scoti, M.; Di Girolamo, R.; D'Alterio, M. C.; Ricci, G.; Zanchin, G.; Leone, G. Synthesis, chain conformation and crystal structure of poly(norbornadiene) having repeating 3,5-enchained nortricyclene units. *Polym. Chem.* **2019,** *10* (33), 4593-4603.

Abstract:

The synthesis of a poly(3,5-tricyclo[2.2.1.$0^{2,6}$]heptylene) [poly(norbornadiene) (PNBD)] mediated by the $TiCl_4/Et_2AlCl$ catalytic system is reported. This polymer is characterized by a rigid nortricyclene repeating structure and unique 3,5-enchainment and is obtained through a transannular cationic polymerization of norbornadiene involving both double bonds. The new PNBD is crystalline with high

glass transition and melting temperatures due to the rigid tricyclic repeating structure. $^{13}$C NMR spectra indicate that the chains of PNBD contain only *exo*/*exo* (**xx**) and *exo*/*endo* (**xn**) nortricyclene repeating monomeric units. Models of the chain conformation and crystal structure of PNBD are also reported. Models of low conformational energy of isotactic and syndiotactic chains of PNBD have been obtained from the regular enchainment of **xx** and **xn** units. The model of the isotactic $(\mathbf{xx})_m$ chain with **s**(2/1) helical symmetry assumes a nearly *trans*-planar conformation, whereas the models of the syndiotactic $(\mathbf{xn–xn})_m$ and $(\mathbf{nx–xn})_m$ chains with **t***c* and **t***i* symmetries assume the conformations $(TG^-G^-TG^+G^+)_n$ and $(G^-TTTG^+T)_n$, respectively. Ideal limit ordered models of the crystal structure have been obtained from the X-ray powder diffraction data and the conformational energy analysis. A good agreement between experimental and calculated powder diffraction profiles has been obtained for a limit ordered model of packing of syndiotactic chains $(\mathbf{nx–xn})_m$ of PNBD with **t***i* symmetry in an orthorhombic unit cell with axes $a$ = 6.6 Å, $b$ = 11.0 Å, and $c$ = 6.84 Å according to the monoclinic space group $P2_1/c$. The real crystal structure of PNBD is disordered because of the possible presence of configurational disorder in the chains due to possible random enchainment of nortricyclene monomeric units in the **xx**, **xn** and **nx** configurations that produces conformational and packing disorder.

4) Auriemma, F.; De Rosa, C.; Scoti, M.; Di Girolamo, R.; Malafronte, A.; D'Alterio, M. C.; Boggioni, L.; Losio, S.; Boccia, A. C.; Tritto, I. Structure and Mechanical Properties of Ethylene/1-Octene Multiblock Copolymers from Chain Shuttling Technology. *Macromolecules* **2019,** *52* (7), 2669-2680.

Abstract:

The mechanical properties and the structural transformations occurring during deformation of some commercial grades of ethylene/1-octene multiblock copolymers (OBCs) obtained from chain shuttling technology are analyzed. The samples are characterized by a statistical multiblock architecture, where soft and

amorphous blocks with high octene concentration (≈18.9 mol %) alternate with hard and crystalline blocks with low octene concentration (≈0.5 mol %). The length of blocks (BL) and the number of blocks/chain (NB) change from chain to chain according to a statistical distribution. The selected samples have molecular mass in the range 85–130 kg/mol, percentage of hard segments in the range 15–27%, and a melting temperature of ≈120 °C. The average molecular masses of the hard blocks $M_H$ and soft blocks $M_S$ are in the ranges 2–3 kg/mol and 6–15 kg/mol, respectively, whereas the number of blocks/chain is in between 2 and 17. Even though the samples are characterized by similar octene concentration, small difference in molecular mass, and fractional content of hard blocks, they show remarkable differences of mechanical properties, depending on the average BL and NB values, encompassing from those of strong elastomers, in the case of samples with low block length and high number of blocks/chain, to those of soft elastomers, in the case of samples with high block length and low number of blocks/chain. The differences in the mechanical properties of OBC samples are amplified by stretching at high temperatures. Not previously stretched films obtained by compression molding show only partial recovery of the initial dimensions in mechanical cycles of stretching and releasing the tension, with values of recovered strain higher than 50% at 25 °C. However, the resultant specimens obtained by release of the tension show good elastomeric properties in a wide deformation range at 25 °C and, in the case of the samples with high strength, also at 60 °C. Fiber diffraction analysis reveals that by stretching at high deformation the orientation of the crystals is accomplished by mechanical melting and formation of an oriented amorphous phase, namely, involving the hard segments extracted from the crystals. Upon releasing the tension recrystallization occurs, and the high degree of orientation achieved by the crystals and amorphous phase is lost.

5) Gimferrer, M.; D'Alterio, M. C.; Talarico, G.; Minami, Y.; Hiyama, T.; Poater, A. Monitorization of the Regioselective Pd-Catalyzed Annulation of Alkylnyl Aryl Ethers leading to 2,3-Bismethylenechromanes. *J. Org. Chem.* **submitted**.

Abstract:

The mechanisms for the synthesis of 2,3-bismethylenechromanes obtained by the reaction between silylethynyloxyarenes with allylic pivalates and catalyzed by palladium catalysts has been investigated by using computational methods rooted into the Density Functional Theory (DFT). The reaction is promoted by a C–H bond activation and consequent bond cleavage of both substrates, followed by a novel annulation. The whole mechanism of this reaction is described together with the drawbacks that potentially could block it. The main role played by the allyl rotation for inducing selectivity reaction together with the lability of the phosphine ligand and base ($Cs_2CO_3$) effects are unraveled. Finally, the nature of the substrates was managed, confirming that *ortho*-allylated silylethynyloxybenzenes lead to the same type of annulated products.

6) Poater, A.; D'Alterio, M. C.; Talarico, G.; Chauvin, R.

A DFT comparison between alkene and arenes as substrates in metathesis reactions by 2$^{nd}$ generation Ru catalysts, **Manuscript in preparation**.

Abstract:

In the current work DFT calculations have been used to compare the ethene and arenes as substrates in the olefin metathesis by Ru(NHC) based catalysts. A large screening of benzene derivatives such as pyran and syran among others was performed in the catalytic pathway with a common 2$^{nd}$ generation Ru(SIMes) based olefin metathesis catalyst. This study aims to explore the possibility to combine metathesis processes with arene substrate and to this aim the concepts of aromaticity and conjugation are taken into consideration, as well as the non-covalent interactions played by π-π interactions between coplanar rings.